Deep-Eddies : Deep Learning for Oceanic Eddy Detection

Evangelos Moschos

To cite this version:

Evangelos Moschos. Deep-Eddies : Deep Learning for Oceanic Eddy Detection. Oceanography. Institut Polytechnique de Paris, 2023. English. NNT : 2023IPPAX005 . tel-04276132

HAL Id: tel-04276132
https://theses.hal.science/tel-04276132

Submitted on 8 Nov 2023

NNT : 2023IPPAX005

Thèse de doctorat

Deep Learning for Oceanic Eddy Detection

Thèse de doctorat de l'Institut Polytechnique de Paris
préparée à École Polytechnique

École doctorale n°626 Dénomination (Sigle)
Spécialité de doctorat : Sciences de l'environnement

Thèse présentée et soutenue à Palaiseau, le 27/01/2023, par

EVANGELOS MOSCHOS

Composition du Jury :

Sylvie Thiria Emeritus Professor, Sorbonne Université (LOCEAN)	Présidente
Ronan Fablet Professor, IMT Atlantique (Lab-STICC)	Rapporteur
Guillaume Roullet Professor, Université de Bretagne Occidentale (LOPS)	Rapporteur
Bruno Buongiorno Nardelli Senior Researcher, National Research Council, Italy (CNR-ISMAR)	Examinateur
Anastase Charantonis Associate Professor, École Nationale Supérieure d'Informatique pour l'Industrie et l'Entreprise (ENSIIE)	Examinateur
Alexandre Stegner Associate Professor, École Polytechnique Senior Rechercher CNRS (LMD/IPSL)	Directeur de thèse
Olivier Schwander Assistant Professor, Sorbonne Université (ISIR)	Co-encadrant
George Galanis Professor, Hellenic Naval Academy	Invité

**ECOLE
DOCTORALE**

Titre : Apprentissage Profond pour la Détection de Tourbillons Océaniques

Mots clés : Tourbillons Océaniques, Télédétection, Vision par Ordinateur, Détection d'objets, Océanographie

Résumé : Les tourbillons océaniques sont des vortex cohérents qui piègent et font circuler dans l'océan des quantités importantes de chaleur, de sel et de nutriments. Plusieurs algorithmes de détection et de suivi des tourbillons sur l'altimétrie satellitaire ont été développés au cours des dernières années, avec de nombreuses applications de monitoring sous-jacentes. Bien que la détection des tourbillons par altimétrie ait permis de nombreuses avancées océanographiques, elle est limitée par la courte fauchée de ces satellites. Ceci conduit à une grande interpolation spatio-temporelle des champs produits et donc à une incertitude dans la détection des tourbillons.

Dans le projet de thèse Deep Eddies, nous exploitons le potentiel émergent de l'apprentissage profond et de la vision par ordinateur appliqués à l'imagerie satellitaire de l'océan, comme les mesures infrarouges de la température de surface de la mer (SST), qui présentent des signatures complexes de tourbillons, par des spirales, des filaments et des gradients. Nous développons des architectures de réseaux de neurones convolutifs, entraînées sur de grands ensembles de données contenant des représentations de tourbillons, pour fournir une nouvelle méthode de détection des tourbillons en temps réel sur des images infrarouges. Notre méthode permet d'améliorer considérablement la précision de la détection des tourbillons par rapport aux méthodes de détection altimétrique standard, tout en étant robuste à la couverture nuageuse des images infrarouges. De plus, nous employons notre réseau de neurones pour détecter les tourbillons sur les images infrarouges, en combinaison avec la détection altimétrique standard, afin de valider les modèles océaniques opérationnels. Grâce à un grand ensemble de données de détection de tourbillons de référence fiables, validées par deux capteurs satellites indépendants, nous employons les contours des tourbillons comme un proxy en temps réel du champ de vitesse. De cette façon, nous pouvons comparer et choisir entre les produits de différents modèles opérationnels dans une certaine région et période. Enfin, nous utilisons les grands ensembles de données collectées pour caractériser la signature SST des tourbillons dans la mer Méditerranée, afin de quantifier l'inversion des anomalies de température de surface des anticyclones et des cyclones. Nous expliquons ce phénomène physique à l'aide d'un simple modèle qui tient compte du mélange vertical. Nos recherches visent à répondre aux besoins des différents acteurs maritimes pour plusieurs applications telles que la surveillance de l'environnement, la pollution plastique, la pêche, la navigation et la défense.

Title : Deep Learning for Oceanic Eddy Detection

Keywords : Ocean Eddies, Remote Sensing, Computer Vision, Object Detection, Oceanography

Abstract : Oceanic eddies are coherent vortices, trapping and transporting in the ocean large amounts of heat, salt, and nutrients. Eddy detection and tracking algorithms on satellite altimetry have been developed during the last years, with numerous monitoring applications. Although altimetric eddy detection has allowed many oceanographic advances, it is limited by the narrow swath of these satellites. This leads to a large spatiotemporal interpolation of the produced fields and therefore uncertainty in eddy detection.

In the Deep Eddies thesis project, we harness the emerging potential of Deep Learning and Computer Vision applied to high-resolution satellite imagery of the ocean, such as infrared measurements of Sea Surface Temperature (SST), which contain complex eddy signatures, through swirls, filaments, and gradients. We develop Convolutional Neural Network architectures, trained on large datasets containing eddy representations, to provide a novel method of real-time eddy detection on infrared images. Our method shows significant improvement in the precision of eddy detection compared to standard altimetric detection methods, while being robust to cloud coverage of infrared images.

Furthermore, we employ our Neural Network detecting eddies on infrared imagery, combined with standard altimetric detection in order to validate operational ocean models. Through a dataset of reliable reference eddy detections, validated by two independent satellite sensors, we use eddy contours as a real-time proxy of the velocity field. This way, we can inter-compare and select from the outputs of different operational models in a certain region and period. Finally, we utilize the large datasets collected to characterize the SST signature of eddies in the Mediterranean Sea, quantifying the inversion of surface temperature anomalies in anticyclones and cyclones. We explain this physical phenomenon through a simple toy model accounting for vertical mixing. Our work seeks to respond to the needs of different maritime stakeholders for several applications such as environmental monitoring, plastic pollution, fishing, shipping, and defense.

Institut Polytechnique de Paris
91120 Palaiseau, France

Chapter 1

List of Papers

Paper I

Evangelos Moschos, Alexandre Barboni, Alexandre Stegner “Why Do Inverse Eddy Surface Temperature Anomalies Emerge? The Case of the Mediterranean Sea”. Published in *Remote Sensing*, August 2022, 14, 3807. DOI: 10.3390/rs14153807.

Paper II

Evangelos Moschos, Olivier Schwander, Alexandre Stegner, Patrick Gallinari “DEEP-SST-EDDIES: A Deep Learning framework to detect oceanic eddies in Sea Surface Temperature Images”. Published in *ICASSP 2020 IEEE International Conference on Acoustics, Speech and Signal Processing*, May 2020, pp. 4307–4311. DOI: 10.1109/ICASSP40776.2020.9053909..

Paper III

Evangelos Moschos, Alexandre Stegner, Olivier Schwander, Patrick Gallinari “Classification of Eddy Sea Surface Temperature Signatures Under Cloud Coverage”. Published in *IEEE Journal of Selected Topics in Applied Earth Observations and Remote Sensing*, June 2020, vol. 13, pp. 3437-3447. DOI: 10.1109/JSTARS.2020.3001830..

Paper IV

Evangelos Moschos, Alisa Kugusheva, Paul Coste, Alexandre Stegner “Computer Vision for Ocean Eddy Detection in Infrared Imagery”. Accepted for publication in *Winter Conference on Applications of Computer Vision 2023*, January 2023

Paper V

Evangelos Moschos, Alexandre Stegner, Briac Le Vu, Olivier Schwander “Real-time Validation of Operational Ocean Models via eddy-detecting deep neural networks”. Published in *International Geoscience and Remote Sensing Symposium (IGARSS 2022)*, July 2022 pp. 8008-8011. DOI: 10.1109/I-GARSS46834.2022.9883253..

Contents

List of Figures

List of Tables

Chapter 2

Introduction

2.1 Remote Sensing of Ocean Eddies

2.1.1 A perpetual ocean

The ocean is in perpetual motion: currents and eddies regulate the dynamic circulation and the exchange of heat, momentum, and mass. Remote sensing has been a key factor in observing and understanding ocean dynamics from large-scale circulation to the fine-scale structures. A multitude of sensors launched on board satellites, provide real-time observations of key oceanic variables such as the ocean surface altimetry, temperature, colour, or roughness.

Eddies, dynamical structures are to the oceans what weather systems are to the atmosphere. By transporting heat, momentum, and mass from their regions of formation to distant areas, they affect the biological productivity (Chelton et al., 2011b), water transport (Zhang et al., 2014), local hydrographic properties (Dong et al., 2014), and the movement of pelagic species (Lobel et al., 1986). Mesoscale eddies, with radii on the order of of tens of kilometers and timescales on the order of months, contribute to an oceanic energy partition on the order of the large ocean circulation (Gill et al., 1974; Zhang et al., 2014). This makes their detection and characterization crucial, both for the study of climate evolution as well as daily operational oceanography.

2.1.2 Surface eddy signature

Eddies that have a signature on the surface of the ocean can be observed with remote sensing, in real-time and in historical analysis, via several instruments on board satellites. Eddies are separated into Anticyclones, which correspond to positive pressure anomalies, and Cyclones, which correspond to negative pressure anomalies. Due to the Coriolis force Anticyclones (Cyclones) will rotate clockwise (counter-clockwise) in the Northern hemisphere and vice versa in the Southern hemisphere.

As a result of the surface pressure anomalies, Anticyclones (Cyclones) will generate a positive (negative) anomaly on the Sea Surface Height (SSH), corresponding to a local ridge (trough). The signature of the eddies on the SSH field is the most commonly studied in operational oceanography, due to advances in satellite altimetry, measuring the height of the sea surface. The anomaly of the eddy on the SSH field is usually referred to as its amplitude. From the pressure anomalies we can derive the geostrophic velocity field u_g due to the balance between the pressure gradient force and the Coriolis effect:

$$f \times \boldsymbol{u}_g + \frac{1}{\rho} \nabla p = 0 \tag{2.1}$$

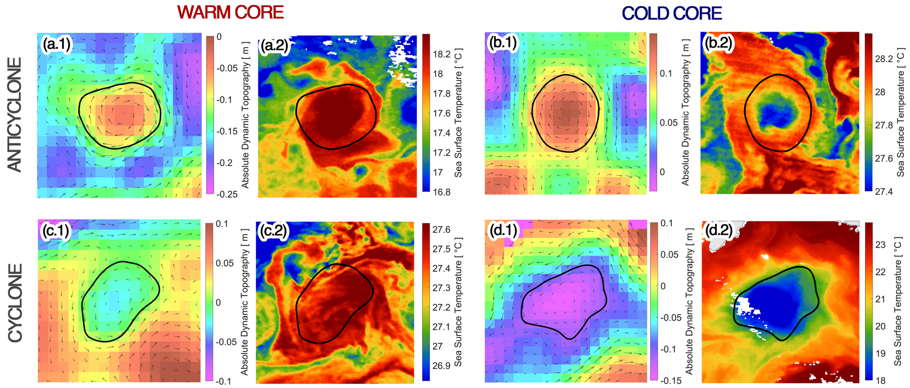

Figure 2.1: **Samples of SST anomalies** for a **(a)** Warm-Core Anticyclone, **(b)** Cold-Core Anticyclone, **(c)** Warm-Core Cyclone, **(d)** Cold-Core Cyclone. On the leftmost panels numbered with **(1)** the velocity vectors and the characteristic contour, computed by the AMEDA algorithm (black line) is superimposed on the Absolute Dynamic Topography. On the rightmost panels numbered with **(2)** the characteristic contour (black line) are superimposed on the patches of Sea Surface Temperature field centered on the detected eddy. Image patches are of side $5R_{max}$, chosen in order to include the temperature of surrounding waters.

where f is the Coriolis parameter, p is the surface pressure field, and ρ the water density.

A second studied signature is that of the temperature anomaly of the eddy with respect to the surrounding water temperature. In most of the literature and several observational studies (Frenger et al., 2013; Gaube et al., 2015) Anticyclonic Eddies are considered to induce a warm-core anomaly and Cyclonic Eddies are considered to induce a cold-core anomaly. Although this regular correlation between the pressure and temperature anomalies holds for the majority of observed eddies, having regular temperature anomaly signatures, a significant amount of inverse anomaly eddy signatures has been noted by studies in several parts of the global ocean. In Figure 2.1 we depict examples of regular and inverse eddy signatures, as seen by an infrared satellite for eddies in the Mediterranean Sea. Our work presented in Paper I further analyzes the distribution of regular and inverse signature in the Mediterranean Sea and explores a mechanism for their emergence.

Finally, eddy signatures can also be found on other types of satellite observations, such as Ocean Colour Reflectance and Synthetic Aperture Radar measurements, described in the following section.

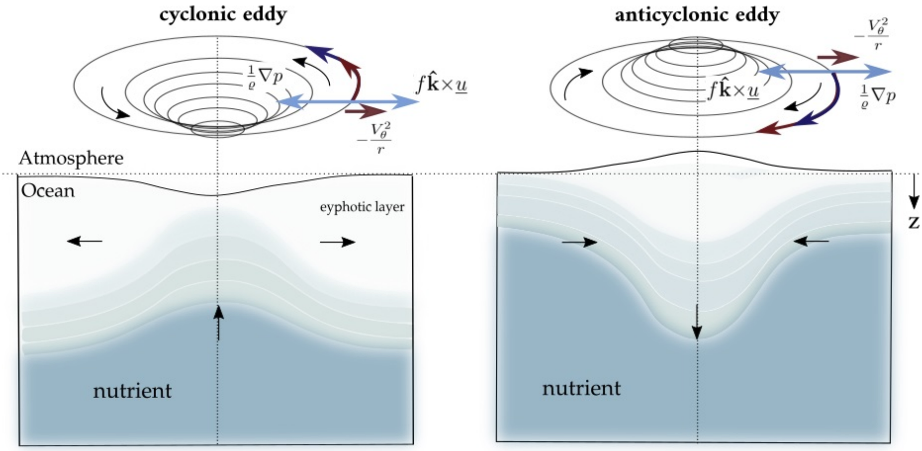

Figure 2.2: **Schematic representation of the 3D structure of Cyclonic and Anticyclonic eddies**. The surface trough and ridge owing to the (cyclo)geostrophic balance are schematically exaggerated. The corresponding shallowing and deepening of the mixed layer as well as the up/downwelling effects transferring nutrients from the deep to the euphotic layers are represented. Figure source: Ioannou, 2019

2.1.3 Subsurface eddy structure

The surface signature of an eddy is only the "tip of the iceberg" of a 3-dimensional structure, extending temperature, salinity, and density anomalies to tens to hundreds of meters of depth. This 3-dimensional structure is responsible for the modulation of the local hydrography (Dong et al., 2014), modulation of the mixed layer (Gaube et al., 2019), trapping of heat and nutrients (Chelton et al., 2011b), the movement of pelagic species (Durán Gómez et al., 2020), and the trapping of microplastics (Brach et al., 2018), among other effects. In Figure 2.2, the effect of the eddy geostrophic balance (equation 2.1) on the sea surface anomaly is schematically exaggerated, while the three-dimensional structure of eddies is also portrayed . For cyclonic (anticyclonic) eddies surface trough (ridge) corresponds to a shallowing (deepening) of the local Mixed Layer as well as a deep upwelling (downwelling) activity, resulting in the vertical transport of nutrients between the euphotic and deep layers of the ocean. The subsurface structure of an eddy is usually defined by an underwater "core", where the maximum density, temperature, or salinity anomaly is found, below the mixed layer (Laxenaire et al., 2019). Eddies can also form a "double core" structure, with two such local maxima found in different depths.

The three-dimensional structure of an eddy is estimated through vertical profiling, most often by in-situ measurements using ARGO floats (Wong et al., 2020). An ARGO instrument is programmed to dive until a certain parking depth and perform measurements of key variables such as temperature, salinity, and pressure (from which density is deduced) or measurements of biological indices. ARGOs have a certain return period usually 7-14 days, over which the float will perform a full cycle from the surface to the parking depth and up again, sending the collected information inland via GPS. Figure 2.3 depicts the typical cycle of an ARGO float. It is noted that ARGOs can be "trapped" into the rotating filaments of an eddy for several days or even months, providing continuous measurements of the evolution of its three-dimensional structure, making the correct initial positioning of the float a crucial task.

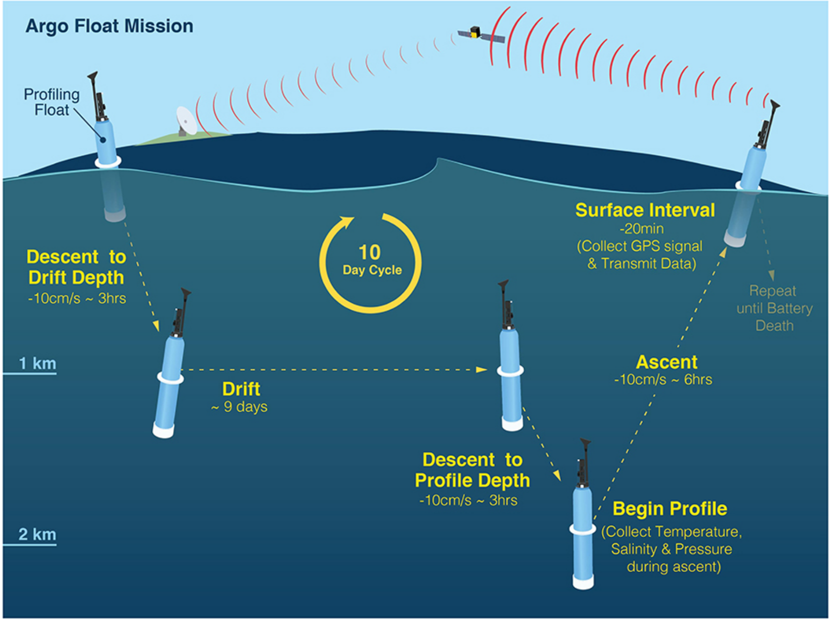

Figure 2.3: **Schematic of the cycle of an ARGO**. During a typical period of 7-14 days, ARGOs will descend to their profile (parking) depth collect temperature, salinity, pressure, and other variables then move again towards the surface to communicate the data inland via GPS. Figure source: Wong et al., 2020

2.2 Satellite Data

2.2.1 Altimetry

Satellite Altimetry operating as early as 1978 with the SeaSat U.S. Satellite, has been key in the observation, understanding, and monitoring pf the ocean dynamics. Essentially, satellite altimetry measures the time for a radar wave emitted from the satellite to reach the sea surface and bounce back to it, and uses it to extract information on the sea surface. In this sense measurements of the Sea Surface Height (SSH) are performed along the tracks of altimetric satellites. With several altimetric satellites currently in operation such as Jason 3, Sentinel 3A,3B and 6MF, HY-2B,C and C, CFOSAT, Saral, and Cryosat, as well as the upcoming wide-band SWOT mission in preparation, along-track measurements of SSH are performed at any given moment in various positions along the globe.

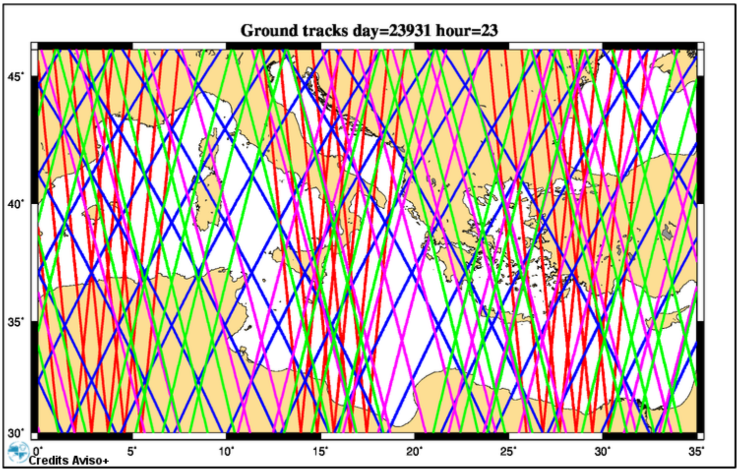

Figure 2.4: **Simulation of satellite altimeter tracks over the Mediterranean Sea**. Accumulated tracks (each colour represents an individual satellite) over a period of 11 days are plotted on the Mediterranean Sea. Gaps denote the regions that are not visited during this period. Figure source: AVISO.

However, as depicted in Figure 2.4 showing the cumulated altimetric tracks over 11 days on the Mediterranean Sea, for a certain time period, satellite tracks will only cover some parts of the sea surface. In order to produce gridded maps of SSH with no missing data, a spatiotemporal interpolation is performed. In this framework, the SSALTO/DUACS multimission altimeter products (Taburet et al., 2019) provide daily gridded SSH maps, distributed by the Copernicus Marine Service (CMEMS).

Through the SSH measurements of satellite altimetry and by resolving the geostrophic balance, the observation of the geostrophic velocity field, an important component of the ocean circulation, has been made possible. In Figure 2.5 we provide an example of SSH observations and derived geostrophic velocity fields in the Eastern Mediterranean Sea, revealing the important presence of eddies (seen as anomalies on the SSH) which modulate the local circulation. The well-developed task of eddy detection using these maps will be analyzed in the following section.

Even though satellite altimetry, has been a primordial factor in revealing the complexity of ocean dynamics, its limitation in real-time ocean monitoring stems

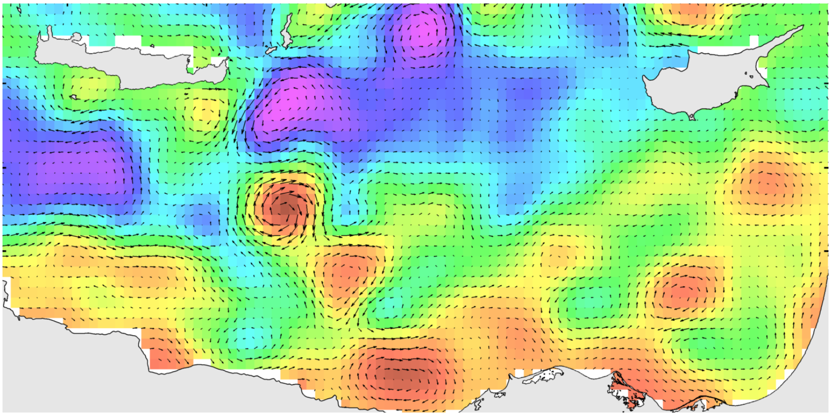

Figure 2.5: **Altimetric Satellite Observations (SSH and Velocities) in the Eastern Mediterrranean Sea**. The measured Sea Surface Height is plotted with colour on the background, while the derived geostrophic velocity vectors are shown with black arrows. A daily snapshot of geostrophic velocity reveals the important presence of eddies.

from the aforementioned spatio-temporal interpolation that is necessary, due to the partial sampling method. While in the sections that follow we further discuss these limitations, we present hereby alternative sources of ocean monitoring, notably via satellite imagery.

2.2.2 Infrared Imagery

Infrared observation of the earth from space has been the first deployed method of remote sensing, stemming back to 1960 with the TIROS-1 U.S. satellite. Infrared satellite imagery measures the temperature of the Earth (land or sea), by detecting heat energy in the infrared spectrum. Infrared satellite imagery has been also specifically developed for the observation of the ocean as it measures the essential variable of the Sea Surface Temperature (SST), important in the monitoring and understanding of the ocean's hydrography and dynamics. In an operational sense, the main advantage of infrared imagery is its independence from visible light in order to operate. The main disadvantage of this type of measurement is that it is obstructed by cloud coverage, not allowing the measurement of the sea temperature at clouded locations.

The high-resolution of the SST observations, compared with satellite altimetry, consists a significant advantage when wanting to observe fine-scale filaments, as well as smaller-scale structure such as sub-mesoscale eddies. Additionally, the wide swath of infrared imagery, produces, in the scale of a day, a coherent image of the globe, and creates therefore no uncertainty as to the measured strctures and dynamics, which is the case in the highly interpolated satellite altimetry.

In Figure 2.6 we provide an example of SST observations in the Eastern

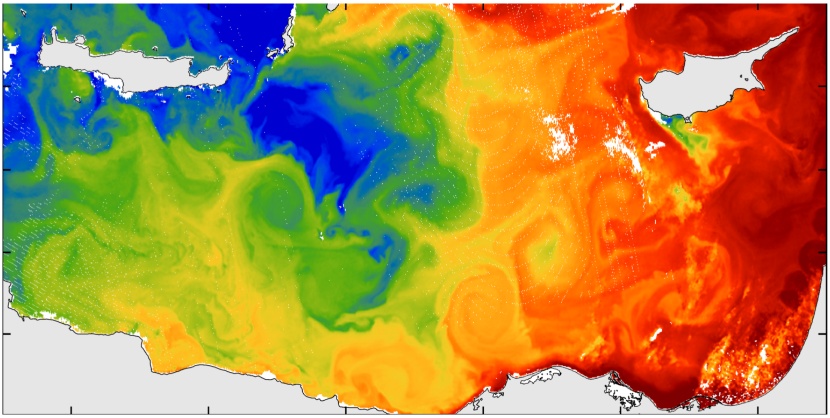

Figure 2.6: **Infrared Satellite Observations (SST) in the Eastern Mediterranean Sea**. The measured Sea Surface Temperature is plotted with colour on the background (blue represents colder waters and red represents warmer waters). On clear day with no clouds, the fine-scale filament and of mesoscale and submesoscale structures of the mediterranean sea become apparent in infrared satellite imagery.

Mediterranean Sea, revealing, on a clear day without cloud coverage, the fine-scale filaments, mesoscale and submesoscale structures of the Mediterranean. These complex patterns and representations of eddies can be harnessed through a Computer Vision based approach, which consists of the main contribution of this thesis and will be furtherly analyzed in the following sections.

2.2.3 Going further: Visible Images and Radar

Visible imagery has also been increasingly developed as a way to provide high-resolution observation of the earth, for terrestrial and oceanic applications. In the oceans, visible light emitted from the satellite is reflected with higher intensity in zones of high biological pigment (nutrient) concentration and absorbed in zones of low biological activity. Ocean Color Reflectance (OCR) is therefore an important proxy for chlorophyll concentration in the ocean. Eddies, which trap and circulate nutrients in their core or via filaments, have a clear signature on visible satellite observations and derived chlorophyll maps. In Figure 2.7 we provide an example of OCR observations in the Eastern Mediterranean Sea, revealing the complex signature of eddies found in this type of imagery.
As with infrared sensors, visible light is obstructed by cloud coverage, while it is only effective during local daytime. However, visible sensors tend to provide highly resolved images at the scale of 300 meters, allowing for the detection of smaller sub-mesoscale structures, and a direct estimation of their biological properties.

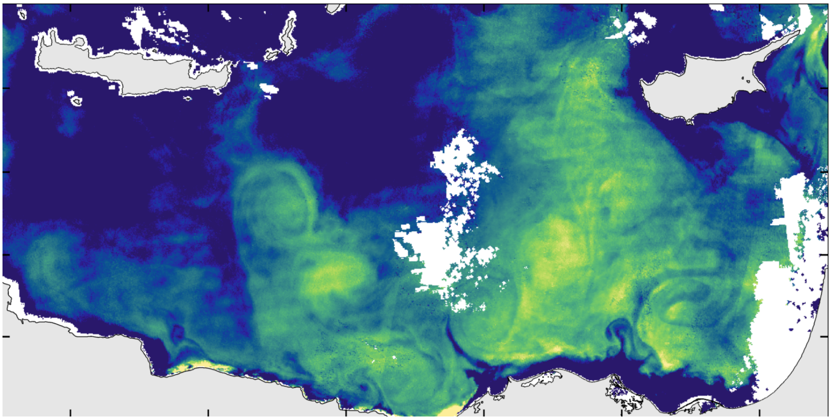

Figure 2.7: **Visible Satellite Observations (OCR) in the Eastern Mediterranean Sea**. The measured Ocean Colour Reflectance is plotted with colour on the background. Visible colour is reflected in regions of high biological pigment concentration. Eddies, which trap and circulate nutrients have a clear signature, when there is no cloud coverage, on this type of imagery.

Additionally, eddies also many times portray a signature on measurements of the rugosity of the sea surface. Synthetic Aperture Radar (SAR) satellites have been developed for several applications, oceanic and terrestrial, with the great advantage that they can bypass clouds and offer images in resolution even higher than those of infrared or visible observations. An example of the SAR observations in the Eastern Mediterranean Sea is provided in Figure 2.8, where a signature of an eddy is apparent on the measured rugosity of the sea surface. As seen in the figure, SAR observations are provided in granules (part of a mid-range swath track) with a longer revisit period than those of infrared and visible sensor satellites. Nevertheless, these granules are measured in ultra-high resolution, revealing the finest scale structures achievable with current remote sensing technology. An important disadvantage of observing eddies via SAR is that their signature can be affected by local wind and wave effects.

Despite their potential, we have not extended this study to visible imagery or SAR observations, although they will be discussed in the perspectives section.

2.3 Eddy Detection

2.3.1 Standard Eddy Detection Algorithms

The advances in Satellite Altimetry have led to 40 years of development of altimetric eddy detection and tracking algorithms operating on the Sea Surface Height or geostrophic velocity fields (Holloway, 1986). In a reference study, Chelton et al., 2011a analyzed sixteen years of SSH satellite data, detecting

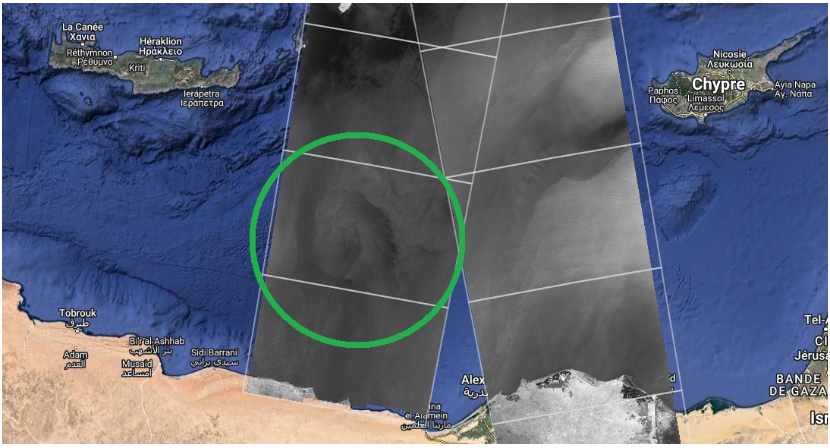

Figure 2.8: **Synthetic Aperture Radar Satellite Observations (SAR) in the Eastern Mediterranean Sea**. With the ability to bypass clouds, SAR measurements offer ultra high-resolution observations, provided in granules. Eddies can sometimes have a signature on the measured rugosity of the sea surface, such as the one seen inside the green circle.

around 1.15 million individual eddy observations and revealing the prevalence of mesoscale structures all over the ocean. We refer to these algorithms as *standard altimetric eddy detection* as they consist, today's oceanographic paradigm, using an objective function on the aforementioned fields. Standard altimetric eddy detection can be broken down into three main groups of algorithms:

- Those that utilize the *geometric* properties of the SSH field, i.e. search for peaks and troughs in it, which represent the pressure anomalies.
- Those that utilize the *dynamical* properties of the geostrophic velocity field derived from altimetry, i.e. the isolines of the flow field.
- Hybrid algorithms that utilize both of the above

Additionally, some of the eddy detection algorithms perform object tracking, by concatenating time series of eddy detections through iterative colocalization or graph methods. Merging and splitting events between two eddies, influenced by the effect of the beta-plane and observable on altimetry, are also recorded by some of the algorithms.
Table 2.1 provides a comparison of some of the main eddy detection and tracking algorithms along with their main properties. We especially mention here the method of the Okubo-Weiss parameter (Okubo, 1970; Weiss, 1991) which quantifies the importance of rotation with respect to the deformation of a Sea Surface Height field and has been in turn used for eddy identification and tracking in various studies. This method has been however sensitive to the

threshold used to identify the vortex boundary and could thus miss weak and intense eddies. Hybrid methods surpass this limitation by using the SSH field to find priors while performing the eddy contour detection on the velocity field. Mkhinini et al., 2014 introduced a dynamic parameter, the *Local Normalized Angular Momentum (LNAM)* which does not depend on the eddy intensity and allows for the identification of closed contours.

Le Vu et al., 2018 introduced a method that not only allows for an optimized combination of the dynamical LNAM parameter and the geometric properties but also accounts for the eddy merging and splitting events, offering the multi-purpose *Angular Momentum Eddy Detection and Tracking Algorithm (AMEDA)*. The AMEDA can be applied on any velocity field, e.g. observed by satellite, numerical model output, or laboratory experimental tank, independent of the grid resolution. By applying the AMEDA on a long record of AVISO velocity field data (2000-2019) a unique dataset containing eddy tracks and detection on the Mediterranean and the Arabian Sea was released as the *DYNED-Atlas*, publically available in https://www1.lmd.polytechnique.fr/dyned/.
For the purposes of this study, the AMEDA algorithm is used when we refer to standard altimetric eddy detection, which will be applied to the corresponding velocity field. The identification of potential eddy centers by AMEDA is performed by computing the LNAM of the velocity field. Only eddy centers with at least one closed contour of the stream function of the velocity field are considered. A radial profile of the velocity for each detected eddy center is calculated by computing the average velocity and radius at each closed streamline around it:

$$\langle V \rangle = \frac{1}{L_p} \oint \vec{V}\, d\vec{l} \tag{2.2}$$

where $\vec{V}$ is the local geostrophic velocity field and L_p is the streamline perimeter. The radius R of the characteristic contour is obtained by considering a circular contour of an equivalent area A:

$$\langle R \rangle = \sqrt{\frac{A}{\pi}} \tag{2.3}$$

Characteristic quantities are calculated for every eddy detection:

- The characteristic eddy contour, corresponding to the closest isoline of the eddy (equation 2.2) where the velocity is maximum.
- The radius R_{max} of the characteristic contour via equation 2.3.
- The velocity V_{max} of the characteristic contour.
- The barycenter x_{bar}, y_{bar} of the characteristic contour.

Various objective algorithms have also been developed for eddy contour identification on infrared observations of SST. Fernandes, 2008 has developed an ellipse fitting algorithm on identified eddy locations, while D'Alimonte, 2009 has inspected iso-SST patterns to identify eddy locations using fronts and gradients and extract morphological parameters (location, scale, symmetry, rotation). Dong et al., 2011 use a different methodology, that derives the velocity field from the SST field via the thermal wind equation, detecting eddy locations on the velocity product. In the same framework, Isern-Fontanet et al., 2014 showed that the SST field can be used as a proxy of the stream function in various areas of the Mediterranean region, provided that the Mixed Layer Depth is adequately large. The objective eddy detection algorithms on infrared observations are listed in Table 2.1. All of the above algorithms try to process the complex patterns found in high-resolution infrared imagery, through physics-informed methods. In the subsection that follows we argue that machine learning-based methods are much more powerful in extracting the complex features and patterns found in infrared imagery and can be used to build a new state-of-the-art in eddy detection.

	Criteria			
Study	Observed Variable	Type	Tracking	Merging Splitting
(Isern-Fontanet et al., 2003)	SSH	Geometric	NO	NO
(Chelton et al., 2007)	SSH	Geometric	YES	NO
(Nencioli et al., 2010)	SSH	Geometric	YES	NO
(Chelton et al., 2011a)	SSH	Geometric	YES	NO
(Mason et al., 2014)	SSH	Geometric	YES	NO
(Mkhinini et al., 2014)	VEL	Dynamical	YES	NO
(Matsuoka et al., 2016)	SSH	Geometric	YES	YES
(Le Vu et al., 2018)	SSH, VEL	Hybrid	YES	YES
(Pegliasco et al., 2022)	SSH	Geometric	YES	NO
(Fernandes, 2008)	SST	Ellipse	NO	NO
(D'Alimonte, 2009)	SST	Gradient	NO	NO
(Dong et al., 2011)	SST	Gradient	NO	NO
(Isern-Fontanet et al., 2014)	SST	Gradient	NO	NO

Table 2.1: Comparison of Studies using Objective Methods for Eddy Detection

2.3.2 Machine Learning for Eddy Detection

Owing to the important advances in the field of computer vision, Machine Learning has been leveraged for the detection of eddies, from the early period of shallow neural networks to the present day of Deep Learning. Studies have been conducted on most of the available remote sensing observations (SSH, SST, and SAR) where eddy surface signatures can be found. Convolutional Neural Networks (LeCun et al., 1995) are mainly employed, with several variations of architecture, to perform an object detection task either with the form of whole-image classification, object localization or pixel-wise segmentation. We provide in Table 2.2 a comprehensive comparison of several published works on eddy detection using Machine Learning methods. We compare these works based on the following criteria:

- The measured variable used for training and applying the Neural Network.
- The source of the data used to train i.e. Satellite Observations or Synthetic (Model) Data. For satellite data observation we precise if data has been labeled by experts (EL).
- The way the task is defined (i.e. Classification/Localisation or Segmentation).
- The overall category of the architecture employed.
- The abillity to perform a forecast of the future eddy position.

	Criteria				
Study	Measured Variable	Data Source	ML Task	Architecture	Forecast
(Lguensat et al., 2018)	SSH	Satellite	Segmentation	UNET	NO
(Franz et al., 2018)	SSH	Satellite	Segmentation	LSTM+CNN	NO
(Duo et al., 2019)	SSH	Satellite	Localisation	FPS+ResNet	NO
(Wang et al., 2021)	SSH	Satellite	Localisation	GRU-based	YES
(Liu et al., 2021)	SSH, SST	Satellite	Segmentation	CNN-based	NO
(Lambhate et al., 2021)	SSH, SST	Satellite-EL	Segmentation	UNET-like	NO
(Du et al., 2019)	SAR	Satellite	Classification	CNN+SPP	NO
(Castellani, 2006)	SST	Satellite	Classification	MLP	NO
(Moschos et al., 2020)	SST	Satellite-EL	Classification	ResNet	NO
(Moschos et al., 2023)	SST	Numerical Model	Segmentation	UNET-like	NO

Table 2.2: Comparison of Studies using Machine Learning Methods for Eddy Detection

Studies such as those of Du et al., 2019; Franz et al., 2018; Lguensat et al., 2018; Wang et al., 2020 used CNN-based architectures in order to detect eddies

in SSH data either as a task of Localisation or Pixel-Wise Segmentation. Other studies employing CNNs (Lambhate et al., 2021; Liu et al., 2021) additionally incorporated corresponding SST data, with the latter utilizing a small expert-labeled data set for training and testing.
Despite their variety in input variables, feature engineering, and employed neural network architectures, all of the listed studies are training neural networks using ground truth of eddies detected on satellite observations via objective algorithms. As we will showcase in the following sections of the introduction, these ground truths contain a large amount of noisy labeling due to the inherent uncertainty of the altimetric data on which the objective eddy detection algorithms operate. Therefore, the best performing Machine Learning-based methods will only perform as well as the best of the Objective Eddy Detection algorithms. In order to outperform standard eddy detection, we focus in this study on training with accurate ground truths for learning representations, via numerical model synthetic data. Furthermore, we use infrared images of SST as the operational application data which allow to surpass the limitations of standard altimetric eddy detection.

2.3.3 Limitations of Altimetry and Perspectives

Despite the importance of standard altimetric eddy detection, it is inherently limited by the uncertainty and low resolution of the input altimetric maps. Recent studies have quantified the limits of eddy detections on standard altimetry maps. By simulating satellite altimetry products, Amores et al., 2018 showed that altimetric detection only captures 6 to 16 % of eddies in the North Atlantic Ocean and the Mediterranean Sea respectively. In addition, the authors have calculated a constant bias of artificially larger detected eddies, compared to their real size. In the same framework, in a study of the Mediterranean Sea, Stegner et al., 2021 showed that altimetric detection has a Ghost (False Positive) rate for Anticyclones (Cyclones) of 35% (45%) for radii between 15 and 25km, dropping to 10% (30%) for radii between 25 km and 35km. Additionally, by employing a collocalization schema, Stegner et al., 2021 showed that much of what is seen as large cyclones in altimetric maps is actually an average composed of smaller cyclones, unseen due to the spatial resolution of the altimetry. Regarding the average error of the position of eddies, the authors show that this does not exceed the grid size of altimetry maps (i.e. 1/8 °), while the average error on eddy position does not exceed 25%. However, the authors do report a systematic underestimation of the intensity of the eddies i.e. of the maximum azimuthal geostrophic velocity V_{max}. This underestimation can be as high as 100% (60%) for anticyclones with radii of 25km, dropping to 50% (30%) for anticyclones (cyclones) with radii of 35km.
Machine Learning approaches to eddy detection that employ altimetric observation as input are also bound by the same limitations due to the input data uncertainty. Thus, as developed previously, the best of the Machine Learning algorithms will only be as good as the best of the standard eddy detection algorithms, the outputs of which are used as a training ground truth. It is for

this reason that the potential of Machine Learning for eddy detection is harnessed by its application on Satellite Imagery on the infrared or visible spectrum.

2.4 Learning Eddy Representations

2.4.1 Retaining Ground Truth from Satellite Data

Supervised learning links the representations of input data ($x \in X$) to a prematched ground truth ($y \in Y$). Thus, for the infrared eddy detection task, we learn the link between the eddy signature on the SST data with a linked dynamic eddy contour, corresponding to the streamline of maximum velocity. A match between an infrared image patch x and a dynamical contour y needs to be performed to retain the supervised learning dataset. This problem is specific in that a prior of the location of an eddy is needed to extract x and y. As we have no information on x (SST) we consider y to be on the location of an eddy detection on the Velocity Field. Thus, when using satellite data, an inaccurate eddy prior and thus inaccurate ground truth $\tilde{y}$ could lead to a noisy SST patch $\tilde{x}$ with no eddy signature. This can be due to several reasons:

- The altimetric eddy detection used to retain the eddy prior, is erroneous, due to the uncertainty of the altimetric observation maps.
- Cloud Coverage of the SST observation corrupting the eddy signature.
- Atmosphere-Ocean interaction and submesoscale phenomena might create noise on the SST image on different wavelengths than the studied dynamics.

Through a visual inspection of 400 SST patches for each eddy type (Anticycles, Cyclones) retained through an altimetric prior, we have retained that only 40% of Anticyclonic and 30% of Cyclonic SST signatures x and corresponding ground truths y are accurate. Learning representations with such an significant amount of noisy labels can be a tedious process and imply extensive manual labeling. We seek therefore alternative sources of eddy representations with accurate underlying dynamic ground truths.

2.4.2 Numerical Models of the Ocean

Numerical Models of the Ocean resolve the ocean dynamics in high resolution while also simulating fields like the SST through advection schemas. We can therefore use such simulations of the oceanic basin to retain accurate pairs of eddy SST signatures (patches) and dynamical contours as the output SST field always corresponds to the simulated velocity field. To this end, data assimilation, performed in operational models is not necessary, as we only require a free realistic simulation of the dynamics of the studied domain.

The CROCO Numerical Model of the Ocean is a realistic numerical simulation of the ocean circulation, covering here the domain of the Mediterranean Sea. CROCO is able to resolve very fine scales of ocean dynamics and their interactions

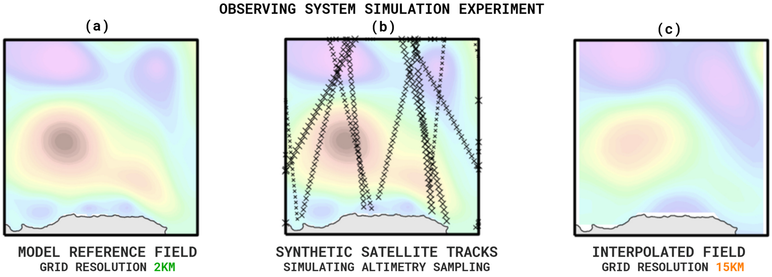

Figure 2.9: An OSSE consists of (a) Retaining a high-resolution numerical model field of SSH (b) Sampling the field via synthetic satellite tracks which simulate observation by altimeters (c) Inhomogenous spatio-temporal interpolation between the sampled points to receive the OSSE field. In our experiment grid resolution is degraded from 2km to 15km.

with larger scales. The model solves the primitive equations on a grid with a horizontal resolution of 2km in both longitudinal and latitudinal directions. The model performs a three-dimensional simulation of the ocean dynamics using forty unevenly distributed vertical layers to discretize the water column. These vertical layers are closer to each other near the surface and their distance becomes larger towards the bottom of the ocean, where the vertical gradients of hydrological parameters (temperature or salinity) are weak. For more details on the numerical characteristics of the CROCO model, we refer to Shchepetkin et al., 2005, Debreu et al., 2012, and Auclair et al., 2018. The simulation used in this study, CROCO-MED60v40-15-16, was forced at the ocean surface with ARPEGE HR analyzed meteorological fields (winds, pressure, air temperature, relative humidity). The initial and the boundary conditions were built from the CMEMS global system analysis optimally interpolated on the computational grid.

In the following sections, we use both the dynamical outputs (SSH, Velocities) as well the SST output of the CROCO numerical model as reference model data in order to train neural networks on accurate ground truths (see section 2.5.4). These numerical model data constitutes also as a *reference* on which we can simulate the altimetric observation, as explained in the following subsection, and thus quantify the performance of standard eddy detection methods and compare them with those developed in this work.

2.4.3 Observing System Simulation Experiment

In order to reproduce the altimetric satellite observation, while also having an accurate reference ground truth, we simulate synthetic data through an Observing System Simulation Experiment (OSSE) based on the numerical model output. The OSSE reproduces the same observation errors and statistical properties found in the satellite observation [1] and is always linked to a corresponding reference of the numerical model. In Figure IV.2 (a) presents an example of numerical model output. To downsample the field in an inhomogeneous manner, we simulate tracks using a four-satellite configuration, comprising the reference mission Jason-3 and three other missions: Sentinel3-A, Sentinel3-B, and Cryosat-2. The synthetic satellite tracks are reproduced through the SWOT simulator software (Gaultier et al., 2016), providing realistic measurement errors and noise. The simulation of the satellite tracks on the model reference field is depicted in Figure IV.2 (b). The resulting synthetic along-track field is then processed to compute gridded fields with the same interpolation schema that is utilized for the production of gridded SSH satellite data (Taburet et al., 2019). It consists of an inhomogeneous spatiotemporal interpolation between the sampled points by the synthetic tracks. An example of an interpolated OSSE field is shown in Figure IV.2 (c). Preprocessing is also carried out on the numerical model simulation data to filter large-scale, high-frequency signals derived from atmospheric forcing fields (Carrère et al., 2003)

2.5 Computer Vision Principles

The advances of *Computer Vision* performed through *Convolutional Neural Networks (CNNs)* (LeCun et al., 1989) have been particularly successful in practical applications which consist of processing complex imagery, such as satellite observations of the ocean. In this section we outline the main elements of the structure and the training procedure of a Neural Network, describe more specifically the functioning and architecture of CNNs and give a brief summary of the transfer learning methodology used in this study. As the oceanography-oriented readers of this manuscript might not be familiar with the Machine Learning terminology we have chosen to introduce key terms using *italics* in this section.

2.5.1 Artificial Neural Networks: Structure, Training, Parameters

Artificial Neural Networks (ANNs), are computing systems, consisting of sets of interconnected nodes, owing their naming to inspiration from the functioning of a bilogical counterpart (Bishop, 2006; Goodfellow et al., 2016). These systems learn to perform tasks through inspecting examples, and without needing to be implicitly programmed with task-specific rules.

The keystone of ANNs is their *artificial neurons*, a set of computationally simple nodes that are combined together. Neurons are structured in layers, which are separated in *input*, *hidden* and *output* ones. An input layer consists of the properly transformed examples needed to train the model, while the output layer will provide the *score* on the performed task. These two layers are separated by a number of hidden layers, in which the training of the model is elaborated.

---

[1] The OSSE can also be described as the numerical model field as if it was observed by altimetry satellites

As their name implies, the interpretability of the (often non-linear) calculation process in hidden layers is much more difficult than in other algorithmic tasks, a fact that is an inherent condition in Deep Learning. Typically neurons are interconnected with eachother: each neuron in hidden and output layers will connect and draw information from all neurons of previous layers. Other types of interconnections exist in more complex architecture. In Figure, 2.10 showing a simple ANN with one hidden layer, these connections are visualized.

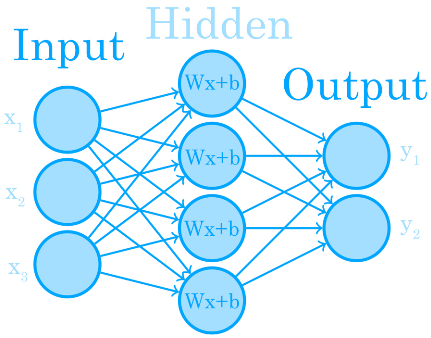

Figure 2.10: Diagram of a simple ANN with one hidden layer. The input layer has three nodes (neurons), the hidden layer has four nodes and the output layer has two.

A linear hidden layer can be mathematically described as a function that applies a linear transformation on a vectorial input of dimension I and outputs a vector of dimension O. The layer will usually contain trainable weights belonging to a matrix **W** and a bias parameter b:

$$y = W \bullet x + b \tag{2.4}$$

$$y_i = \sum_{j=1}^{I} (W_{i,j} x_j) + b_i \tag{2.5}$$

ANNs have the theoretical capacity to approximate any function and especially non-convex ones. This ability stems from the use of a non-linear function called the *activation function* which is applied on the output of layers in order to introduce non-linearity on top of the linear transformations seen in equation 2.4. Commonly used activation function include the *Sigmoid, Softmax, tanh, ReLU*. Here we discuss the ReLU and the softmax function, which are employed in the architectures of this study.

The *Rectified Linear Unit (ReLU)* function used commonly to activate hidden layers of deep networks has the following form:

$$y = max(0, x) \tag{2.6}$$

The ReLU function will thus map all negative values to zero, which allows for a sparse activation of only a part of the hidden layers. It has been found to improve gradient propagation (Glorot et al., 2011) by evading vanishing gradient effects (small values of partial derivatives in equation 2.9 thus no update in weight values).

The Softmax function, used notably to activate the output layer in classification tasks has the following expression:

$$S(y_i) = \frac{e^{y_i}}{\sum_j e^{y_j}} \tag{2.7}$$

The Softmax function takes a real value and maps it between 0 and 1, which corresponds to a probability-like number, proportional to the exponential of the input number. Furthermore, as the softmax function is normalized through the denominator of Equation 2.7, the sum of all softmax outputs of j possible classes for a certain linear output y_i is equal to 1. This is particularly useful in classification tasks, image-wise or pixel-wise, with a predefined number of classes, as is the case of the eddy detection task that we treat.

Training an ANN in a supervised learning approach requires an amount of input labeled examples, called the *Training Dataset*. At the beginning of the training phase, weights are initialized as Gaussian random variables with mean 0, while standard deviation and biases are initialized to zero values. The evaluation of the ability of the model to approximate the ground truth input labels is done through the *Loss Function*, which has as inputs the weights, biases, and samples of the training set. The most common way used to iteratively update the values of weights and biases by reducing the values of the cost function is the method of *Gradient Descent*. In such methods, a non-smooth type of cost function needs to be chosen. One such commonly used loss function is the Cross-Entropy Loss:

$$L(x, y) = -\sum_i y_i * log(\frac{\exp x_i}{(\sum_j \exp x_j)}) \tag{2.8}$$

where L is the loss function, x is a vector of n predictions, and y is a binary vector consisting of zeros and a value of one in the corresponding class dimension.

The prediction and the associated value of the loss function (i.e. distance from ground truth) will be thus computed. The sum of the losses for all examples consists of the total loss. Subsequently, the *Backpropagation Algorithm* will be used in order to propagate this loss and compute the partial derivatives of the cost function $\frac{\partial L}{\partial w}$ and $\frac{\partial L}{\partial b}$ for all the weights and biases. Through an optimization technique, the weights and biases of all the layers of the neural network are then finally updated. A common optimization technique is that of the *Stochastic Gradient Descent* in which:

$$\theta_{t+1} = \theta_t - \lambda * \nabla_{\theta_t} L(f_{\theta_t}(x_i), y_i) \tag{2.9}$$

where θ is the parameter to be approximated that minimizes the cost function $L(f_{\theta_t}(x_i), y_i)$ and is the step or the *learning rate* at which the iterations of step t are performed.

This process of forward-backward pass and optimization is then repeated numerous times, with each repetition consisting of an *epoch*. The goal is to find and converge to a local minimum of the loss function, a goal that SGD usually succeeds to perform by minimizing the loss function even for non-convex cases, as is the case of images studied here.

2.5.2 Spatial Convolution and Pooling

Common ANNs constructed by linear and non-linear (activation) hidden layers require a huge number of parameters to process images. The function of spatial convolution is employed as it can reduce the number of parameters significantly. The use of sliding convolutional filters allows us to explore the spatial relationship in the image. A set of N_k filters $F = f_1, f_2, ..., f_N$ are convoluted spatially with the input image x, to produce a set of N_k 2D feature maps z:

$$z_k = f_k * x \tag{2.10}$$

where $*$ is the convolution operation.

Each filter f_n is slid along the image x producing a corresponding feature map by performing the convolution operation at each area of the image (Figure 2.11) The response in an area will be high if the filter correlates well with it. This way, only the weights of each filter need to be trained, which are shared between the image, reducing largely the amount of trainable parameters as well as allowing equivariance (i.e. if x is shifted, the response of the convolution operation is also shifted). The definition of the size of spatial convolution is given by the size, number, and additional properties of the convolution kernels and not by the size of the images or of the feature maps.

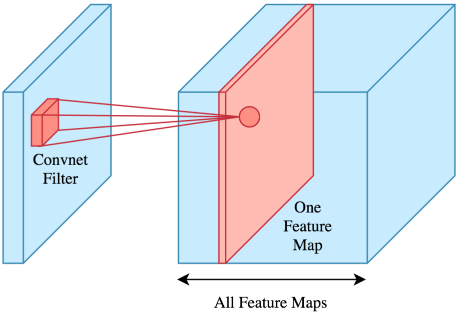

Figure 2.11: The result of the operation between a sliding convolutional filter and an image is extracted in a future map

In order to introduce invariance, as well as reduce the size of the feature maps when moving deeper in the CNN, the process of *Spatial Pooling* is introduced. In pooling layers a function P will be applied over the region of pixels R:

$$p_R = P_{i \in R}(z_i) \tag{2.11}$$

The function of max pooling is commonly selected, which only selects and retains the pixel with the highest value inside a sliding pooling window of a defined size. An example of spatial pooling is given in Figure 2.12 .

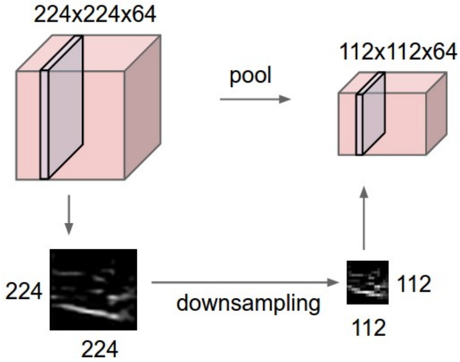

Figure 2.12: An example of spatial pooling operation with a 2×2 filter size and a stride of 2.

2.5.3 Deep Learning and CNN Architectures

The operations of spatial convolution and pooling described before, as well as the common linear layer transformations described at the beginning of the section, will create an ensemble of layers that process the original input image, called the *architecture* of the CNN. An example of a typical CNN architecture is illustrated in Figure 2.13.

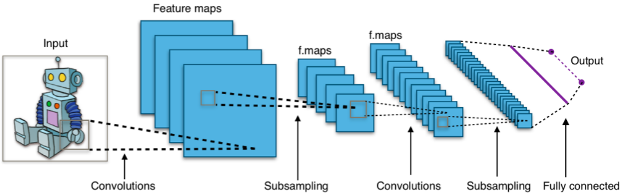

Figure 2.13: An example of a CNN architecture consisting of convolution, pooling, and fully connected linear layers.

The advances in Machine Learning, fueled by modern computational abilities (processing data with GPUs and other methods), have allowed the design and implementation of "deep" architectures, that is neural networks with a large number of hidden layers, giving birth to the term of *Deep Learning*. This has provided an especially outstanding performance in the case of CNNs where the input examples are images with very high dimensionality. Novel deep CNN architectures provide multi-layer setups, which mobilize different methods of architecture engineering for adequate processing of information.

A notable example of a deep CNN architecture are *Residual Networks (ResNets)* He et al., 2016 which use skip connections between layers in order to build deeper architectures. Whereas a large number of hidden layers would originally lead to the problem of saturation of performance, that is a decrease

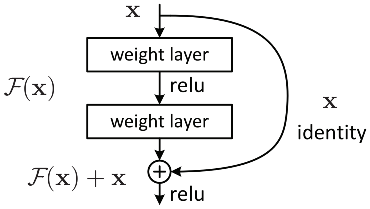

Figure 2.14: Skip Connections between two layers of a Residual Network. Source: He et al., 2016

of accuracy with an increase in the number of hidden layers, after a certain point, ResNet architectures have managed to solve this by requiring a set number of layers called residual blocks approximate not only the desired underlying mapping ($\mathcal{H}(x)$) but the residual mapping ($\mathcal{F}(x)$) which is defined as:

$$\mathcal{F}(x) = H(x) - x \tag{2.12}$$

where x is the input of the residual block. Skip connections are usually inserted in two or three-layer blocks, with the same application for convolutional layers. An example of a skip connection is given in Figure 2.14. In this study a Residual Network with a total of 18 layers is used (from here on *ResNet18*).

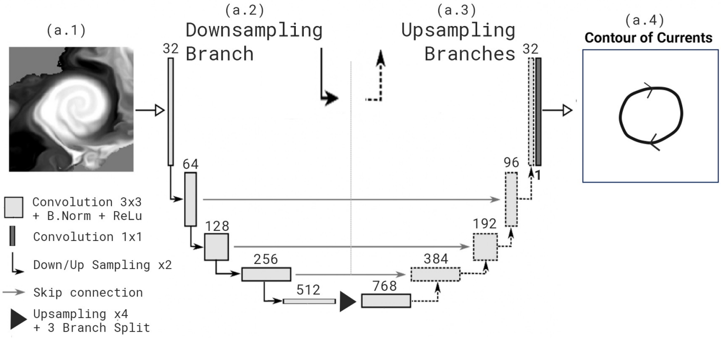

Figure 2.15: Schematic of an encoder-decoder architecture employed for the purposes of this study. As an input, an SST image with an eddy signature is provided, learning its link with an output dynamical contour, representative of the eddy velocity.

Another CNN architecture often employed is encoder-decoders, one of the most popular being the UNET (Ronneberger et al., 2015), owing its name to its U-shaped architecture, which consists of a two-branch, encoder-decoder neural network, proving very efficient for the semantic segmentation of medical imagery. An initial downsampling branch is followed by an upsampling branch, allowing for features of different scales in the input image to be captured. Convolutional, as well as pooling operations are performed from one layer to another. These

operators take the form of a transposed convolution and an upsample pooling in the decoder branch. A final convolutional layer turns the feature maps into the output.
Skip connections are employed between the corresponding layers of the encoder and decoder branches, allowing concatenation of the learned feature maps and passing them as spatial information to the decoder, in order to recover fine-scale details in the output mask. A schematic is provided in Figure 2.15 showcasing the UNET-like architecture that is employed when treating semantic segmentation tasks in this work. As an input, an SST image with an eddy signature is provided, learning its link with an output dynamical contour, representative of the eddy velocity.

2.5.4 Transfer Learning

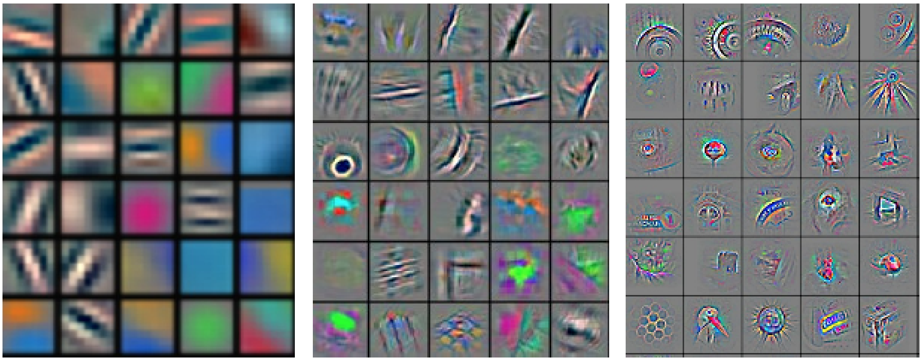

Figure 2.16: Example of learned convolutional kernels, from shallowest layers (left) to deeper (right). The network learns to detect different levels of abstraction the deeper it goes.

When the size of the dataset of the case study is too low for enough features to be extracted the methodology of *Transfer Learning* is employed. It consists of using a CNN which is *pretrained* in a large dataset, having already extracted numerous features which can be generalized to process datasets different from the one used to pre-train the model (An example of learned features from a CNN can be seen in Figure 2.16). Two transfer learning strategies can be employed: *Feature extraction* or *Finetuning*. In the first one, the pre-trained CNN is used to extract features from the dataset of the case study, by constraining all the weights of the hidden layers to their pre-trained value and re-training only the final output layer. In the second one the CNN is finetuned, that is the pre-trained network values are used to initialize the training process (instead of a random initialization described before), and all hidden layers are "unfrozen" to be re-trained.
In this work, we employ transfer learning as a way to surpass the underlying ground truth problem of satellite data, as described in Section 2.4.1. To this

end, we use numerical models of the ocean, described in Section 2.4.2, to extract representations on temperature data with an accurate underlying ground truth, i.e. dynamical eddy contour. We thus dispose of a set of high-resolution data with eddy representations accurate ground truths to perform an initial training. The numerical model data needs to be calibrated accordingly, especially in terms of resolution, to match that of the target satellite data. The CNN trained on numerical model data can then be directly applied on satellite data fields, or further finetuned with a selection of expert-labeled satellite data, to increase performance.

2.5.5 Multi-Task Learning

Multi-task learning consists of combining several tasks to be learned, by means of an addition of loss functions, in order to improve generalization. In a multi-task learning set-up the learning from each task can help improve the performance on the other tasks. We can define a multi-task learning loss as:

$$\mathrm{L}_{total} = \sum_{i=1}^{n} \alpha \mathrm{L}_i \tag{2.13}$$

where L_i are the loss terms corresponding to each task i and α the corresponding weight factors.

For our study of contour detection and based on studies conducted on medical imaging (Murugesan et al., 2019), we explore the use of additional learning factors in order to boost the eddy map segmentation task which is the primary learning task.

2.6 Summary of Papers

We present an article-based manuscript, which combines 5 publications in scientific journals and conference proceedings, conducted during the course of the thesis:

Paper I This journal manuscript explores the signatures and anomalies of mesoscale eddies on Sea Surface Temperature images in the Mediterranean Sea. We observe the seasonal emergence of eddy SST anomalies of Cold-Core Anticyclones and Warm-Core Cyclones, which we refer to as inverse anomalies, as well as the correlation between the seasonality of eddy anomalies and the cycle of the Mixed Layer Depth variation. Furthermore, we use in-situ data to link the surface anomaly with the subsurface eddy structure. Finally, we propose a mechanism of vertical mixing explaining the emergence of these inverse eddy anomalies through a simple 1D toy model. For this work, we have utilized a dataset of SST eddy signatures, retreived initially for the purposes of Machine Learning. It sets the stage for this thesis manuscript by providing a physical understanding of the signatures later used for training Machine Learning eddy detection tools.

Paper II This conference proceeding, published at the very beginning of the thesis, is an initial exploration of the possibility to classify eddy signatures (Anticyclone, Cyclone, No Eddy) on Sea Surface Temperature images, using a simple Convolutional Neural Network. The encouraging results reported provided the initial motivation to further pursue the subject.

Paper III This journal manuscript, expands the previous work, exploring the cloud coverage and noisy labeling problems when learning eddy representations on satellite data, in particular SST. Following the task of classification of eddy signatures, we propose a simple method to learn representations with missing data due to clouds, achieving a classification accuracy of 90% for up to 50% cloud coverage in a local SST patch.

Paper IV This manuscript presents our state-of-the-art on eddy dynamical contour detection on SST images, EddyScan-SST. By using an encoder-decoder architecture, a semantic segmentation task is performed through a multi-task learning schema. We also employ a transfer learning schema using numerical model data to learn accurately eddy representations. Through simulated synthetic altimetry data via an OSSE, we show that EddyScan-SST outperforms standard eddy detection methods, both on miss and ghost eddy rates but also on the detected eddy position and size. Finally, we test EddyScan-SST on expert-labeled satellite SST observations.

Paper V This conference proceeding presents a methodology to inter-compare the dynamical outputs of different operational numerical models, by using reliable reference eddy detections. To build a set of reference reliable eddies, we combine eddy detection on altimetry and SST, retaining as the most reliable the eddy detections performed by both independent sensors. We then use these reference detections as proxies of the velocity field, in order to inter-compare the operational outputs of two assimilated models, MERCATOR and MFS, in a case study in the Mediterranean Sea. Our method can be expanded to any region of the globe and offers valuable reference objects for operational model validation, which complement the sparsely available in-situ measurements.

References

Amores, A. et al. (2018). “Up to what extent can we characterize ocean eddies using present-day gridded altimetric products?” In: *Journal of Geophysical Research: Oceans* vol. 123, no. 10, pp. 7220–7236.

Auclair, F. et al. (2018). “Some recent developments around the CROCO initiative for complex regional to coastal modeling”. In: *COMOD 2018-Workshop on Coastal Ocean Modelling*, pp. 1–47.

Bishop, C. M. (2006). *Pattern recognition and machine learning.* springer.

Brach, L. et al. (2018). “Anticyclonic eddies increase accumulation of microplastic in the North Atlantic subtropical gyre”. In: *Marine pollution bulletin* vol. 126, pp. 191–196.

Carrère, L. and Lyard, F. (2003). “Modeling the barotropic response of the global ocean to atmospheric wind and pressure forcing-comparisons with observations (DOI 10.1029/2002GL016473)”. In: *Geophysical Research Letters* vol. 30, no. 6, pp. 8–8.

Castellani, M. (2006). “Identification of eddies from sea surface temperature maps with neural networks”. In: *International journal of remote sensing* vol. 27, no. 8, pp. 1601–1618.

Chelton, D. B., Schlax, M. G., and Samelson, R. M. (2011a). “Global observations of nonlinear mesoscale eddies”. In: *Progress in oceanography* vol. 91, no. 2, pp. 167–216.

Chelton, D. B. et al. (2007). “Global observations of large oceanic eddies”. In: *Geophysical Research Letters* vol. 34, no. 15.

Chelton, D. B. et al. (2011b). “The influence of nonlinear mesoscale eddies on near-surface oceanic chlorophyll”. In: *Science* vol. 334, no. 6054, pp. 328–332.

D’Alimonte, D. (2009). “Detection of mesoscale eddy-related structures through iso-SST patterns”. In: *IEEE Geoscience and Remote Sensing Letters* vol. 6, no. 2, pp. 189–193.

Debreu, L. et al. (2012). “Two-way nesting in split-explicit ocean models: Algorithms, implementation and validation”. In: *Ocean Modelling* vol. 49, pp. 1–21.

Dong, C. et al. (2011). “An automated approach to detect oceanic eddies from satellite remotely sensed sea surface temperature data”. In: *IEEE Geoscience and Remote Sensing Letters* vol. 8, no. 6, pp. 1055–1059.

Dong, C. et al. (2014). “Global heat and salt transports by eddy movement”. In: *Nature communications* vol. 5, no. 1, pp. 1–6.

Du, Y. et al. (2019). “Deep learning with multi-scale feature fusion in remote sensing for automatic oceanic eddy detection”. In: *Information Fusion* vol. 49, pp. 89–99.

Duo, Z., Wang, W., and Wang, H. (2019). “Oceanic mesoscale eddy detection method based on deep learning”. In: *Remote Sensing* vol. 11, no. 16, p. 1921.

Durán Gómez, G. S., Nagai, T., and Yokawa, K. (2020). “Mesoscale warm-core eddies drive interannual modulations of swordfish catch in the Kuroshio Extension System”. In: *Frontiers in Marine Science* vol. 7, p. 680.

Fernandes, A. M. (2008). “Identification of oceanic eddies in satellite images”. In: *International Symposium on Visual Computing*. Springer, pp. 65–74.

Franz, K. et al. (2018). “Ocean eddy identification and tracking using neural networks”. In: *IGARSS 2018-2018 IEEE International Geoscience and Remote Sensing Symposium*. IEEE, pp. 6887–6890.

Frenger, I. et al. (2013). “Imprint of Southern Ocean eddies on winds, clouds and rainfall”. In: *Nature geoscience* vol. 6, no. 8, pp. 608–612.

Gaube, P., J. McGillicuddy Jr, D., and Moulin, A. J. (2019). “Mesoscale eddies modulate mixed layer depth globally”. In: *Geophysical Research Letters* vol. 46, no. 3, pp. 1505–1512.

Gaube, P. et al. (2015). “Satellite observations of mesoscale eddy-induced Ekman pumping”. In: *Journal of Physical Oceanography* vol. 45, no. 1, pp. 104–132.

Gaultier, L., Ubelmann, C., and Fu, L.-L. (2016). “The challenge of using future SWOT data for oceanic field reconstruction”. In: *Journal of Atmospheric and Oceanic Technology* vol. 33, no. 1, pp. 119–126.

Gill, A., Green, J., and Simmons, A. (1974). “Energy partition in the large-scale ocean circulation and the production of mid-ocean eddies”. In: *Deep sea research and oceanographic abstracts*. Vol. 21. 7. Elsevier, pp. 499–528.

Glorot, X., Bordes, A., and Bengio, Y. (2011). “Deep sparse rectifier neural networks”. In: *Proceedings of the fourteenth international conference on artificial intelligence and statistics*, pp. 315–323.

Goodfellow, I., Bengio, Y., and Courville, A. (2016). *Deep Learning*. http://www.deeplearningbook.org. MIT Press.

He, K. et al. (2016). “Deep residual learning for image recognition”. In: *Proceedings of the IEEE conference on computer vision and pattern recognition*, pp. 770–778.

Holloway, G. (1986). “Estimation of oceanic eddy transports from satellite altimetry”. In: *Nature* vol. 323, no. 6085, pp. 243–244.

Ioannou, A. (2019). “Dynamical evolution of intense mesoscale Ierapetra eddies in connection with orographic wind forcing”. PhD thesis. Sorbonne université.

Isern-Fontanet, J., Garcıa-Ladona, E., and Font, J. (2003). “Identification of marine eddies from altimetric maps”. In: *Journal of Atmospheric and Oceanic Technology* vol. 20, no. 5, pp. 772–778.

Isern-Fontanet, J., Shinde, M., and González-Haro, C. (2014). “On the transfer function between surface fields and the geostrophic stream function in the Mediterranean Sea”. In: *Journal of Physical Oceanography* vol. 44, no. 5, pp. 1406–1423.

Lambhate, D. et al. (2021). “W-Net: A Deep Network for Simultaneous Identification of Gulf Stream and Rings From Concurrent Satellite Images of Sea Surface Temperature and Height”. In: *IEEE Transactions on Geoscience and Remote Sensing* vol. 60, pp. 1–13.

Laxenaire, R., Speich, S., and Stegner, A. (2019). “Evolution of the thermohaline structure of one Agulhas ring reconstructed from satellite altimetry and Argo floats”. In: *Journal of Geophysical Research: Oceans* vol. 124, no. 12, pp. 8969–9003.

Le Vu, B., Stegner, A., and Arsouze, T. (2018). “Angular Momentum Eddy Detection and tracking Algorithm (AMEDA) and its application to coastal eddy formation”. In: *Journal of Atmospheric and Oceanic Technology* vol. 35, no. 4, pp. 739–762.

LeCun, Y. et al. (1989). “Generalization and network design strategies”. In: *Connectionism in perspective*. Vol. 19. Citeseer.

LeCun, Y., Bengio, Y., et al. (1995). “Convolutional networks for images, speech, and time series”. In: *The handbook of brain theory and neural networks* vol. 3361, no. 10, p. 1995.

Lguensat, R. et al. (2018). “EddyNet: A deep neural network for pixel-wise classification of oceanic eddies”. In: *IGARSS 2018-2018 IEEE International Geoscience and Remote Sensing Symposium*. IEEE, pp. 1764–1767.

Liu, Y., Zheng, Q., and Li, X. (2021). “Characteristics of Global Ocean Abnormal Mesoscale Eddies Derived From the Fusion of Sea Surface Height and Temperature Data by Deep Learning”. In: *Geophysical Research Letters* vol. 48, no. 17, e2021GL094772.

Lobel, P. and Robinson, A. (1986). “Transport and entrapment of fish larvae by ocean mesoscale eddies and currents in Hawaiian waters”. In: *Deep Sea Research Part A. Oceanographic Research Papers* vol. 33, no. 4, pp. 483–500.

Mason, E., Pascual, A., and McWilliams, J. C. (2014). “A new sea surface height–based code for oceanic mesoscale eddy tracking”. In: *Journal of Atmospheric and Oceanic Technology* vol. 31, no. 5, pp. 1181–1188.

Matsuoka, D. et al. (2016). “A new approach to ocean eddy detection, tracking, and event visualization–application to the northwest pacific ocean”. In: *Procedia Computer Science* vol. 80, pp. 1601–1611.

Mkhinini, N. et al. (2014). “Long-lived mesoscale eddies in the eastern Mediterranean Sea: Analysis of 20 years of AVISO geostrophic velocities”. In: *Journal of Geophysical Research: Oceans* vol. 119, no. 12, pp. 8603–8626.

Moschos, E. et al. (2020). “Classification of eddy sea surface temperature signatures under cloud coverage”. In: *IEEE Journal of Selected Topics in Applied Earth Observations and Remote Sensing* vol. 13, pp. 3437–3447.

Moschos, E. et al. (2023). “Computer Vision for Ocean Eddy Detection in Infrared Imagery”. In: *Submitted to WACV 2023 (Under Review)*.

Murugesan, B. et al. (2019). “Psi-Net: Shape and boundary aware joint multi-task deep network for medical image segmentation”. In: *2019 41st Annual International Conference of the IEEE Engineering in Medicine and Biology Society (EMBC)*. IEEE, pp. 7223–7226.

Nencioli, F. et al. (2010). “A vector geometry–based eddy detection algorithm and its application to a high-resolution numerical model product and high-frequency radar surface velocities in the Southern California Bight”. In: *Journal of atmospheric and oceanic technology* vol. 27, no. 3, pp. 564–579.

Okubo, A. (1970). “Horizontal dispersion of floatable particles in the vicinity of velocity singularities such as convergences”. In: *Deep sea research and oceanographic abstracts*. Vol. 17. 3. Elsevier, pp. 445–454.

Pegliasco, C. et al. (2022). “META3. 1exp: a new global mesoscale eddy trajectory atlas derived from altimetry”. In: *Earth System Science Data* vol. 14, no. 3, pp. 1087–1107.

Ronneberger, O., Fischer, P., and Brox, T. (2015). “U-net: Convolutional networks for biomedical image segmentation”. In: *International Conference on Medical image computing and computer-assisted intervention.* Springer, pp. 234–241.

Shchepetkin, A. F. and McWilliams, J. C. (2005). “The regional oceanic modeling system (ROMS): a split-explicit, free-surface, topography-following-coordinate oceanic model”. In: *Ocean modelling* vol. 9, no. 4, pp. 347–404.

Stegner, A. et al. (2021). “Cyclone-Anticyclone Asymmetry of Eddy Detection on Gridded Altimetry Product in the Mediterranean Sea”. In: *Journal of Geophysical Research: Oceans* vol. 126, no. 9, e2021JC017475.

Taburet, G. et al. (2019). “DUACS DT2018: 25 years of reprocessed sea level altimetry products”. In: *Ocean Science* vol. 15, no. 5, pp. 1207–1224.

Wang, X. et al. (2020). “The prediction of oceanic mesoscale eddy properties and propagation trajectories based on machine learning”. In: *Water* vol. 12, no. 9, p. 2521.

Wang, X. et al. (2021). “MesoGRU: Deep learning framework for mesoscale eddy trajectory prediction”. In: *IEEE Geoscience and Remote Sensing Letters* vol. 19, pp. 1–5.

Weiss, J. (1991). “The dynamics of enstrophy transfer in two-dimensional hydrodynamics”. In: *Physica D: Nonlinear Phenomena* vol. 48, no. 2-3, pp. 273–294.

Wong, A. P. et al. (2020). “Argo data 1999–2019: two million temperature-salinity profiles and subsurface velocity observations from a global array of profiling floats”. In: *Frontiers in Marine Science* vol. 7, p. 700.

Zhang, Z., Wang, W., and Qiu, B. (2014). “Oceanic mass transport by mesoscale eddies”. In: *Science* vol. 345, no. 6194, pp. 322–324.

Papers

Paper I

Why Do Inverse Eddy Surface Temperature Anomalies Emerge? The Case of the Mediterranean Sea

Evangelos Moschos, Alexandre Barboni, Alexandre Stegner

Published in *Remote Sensing*, August 2022, 14, 3807. DOI: 10.3390/rs14153807.

Abstract

It is widely accepted that the signature of anticyclonic (cyclonic) eddies on the sea surface temperature corresponds to a warm (cold) core anomaly. Nevertheless, this statement has been put to question by recent regional studies showing the existence of inverse eddy SST anomalies: cold-core anticyclones and respectively warm-core cyclones. This study shows that the emergence of these inverse anomalies is a seasonal phenomenon that affects the life cycle of mesoscale eddies in the Mediterranean Sea. We use remote-sensing observations and in-situ data to analyse the eddy-induced SST anomaly over a 3 years period (2016-2018). We build an eddy core surface temperature index to quantify the amount of Cold Core Anticyclones and Warm Core Cyclones all over the year and especially during the spring re-stratification period. We find that 70% eddy anomalies are inverse in May and June, both for cyclones and anticyclones. Regular temperature anomalies could reach $1.5°C$ while inverse ones are only present in the first $50m$ of the oceanic layer and hardly exceed $1°C$. In order to understand the underlying dynamical processes, we construct a simple vertical column model to study the impact of the seasonal air-sea fluxes on the surface stratification inside and outside eddies. It is only by taking into account a differential diapycnal eddy mixing - increased in anticyclones and reduced in cyclones - that we reproduce correctly, in agreement with the observations, the surface temperature inversion in the eddy core. This simplified model, suggests that vertical mixing modulation by mesoscale eddies might be the key mechanism that leads to the eddy-SSTA seasonal inversion in the ocean.

I.1 Introduction

Mesoscale eddies are coherent structures with typical radii of the order of 20-80 kilometres. These eddies can be sometimes long-lived, surviving several months or even years. Significant advances in the resolution of both satellite altimetry measurements (Chelton et al., 2011) and high resolution oceanic numerical models (Su et al., 2018) have revealed the predominance of these mesoscale eddies in the global oceanic circulation. They are able to trap and transport heat, salt, pollutants and various biogeochemical components from their regions of formation to remote areas (Laxenaire et al., 2018; Zhang et al., 2014). Their dynamics can impact significantly the biological productivity at the ocean surface (Gaube et al., 2013; Lévy et al., 2018; McGillicuddy Jr, 2016), modify the depth of the mixed layer (Gaube et al., 2019), influence clouds and rainfall within their vicinity (Frenger et al., 2013), amplify locally the vertical motions (Klein et al., 2009), attract pelagic species (Abrahms et al., 2018; Baudena et al., 2021; Gómez et al., 2020) or concentrate and transport micro-plastics (Brach et al., 2018). Thus, long-lived mesoscale eddies are ubiquitous in the global ocean and play a major role in its circulation differentiating from mean patterns. In the Mediterranean Sea, domain of this study, mesoscale eddies have been identified, tracked and analysed, both on their surface and subsurface structure in many studies (Amitai et al., 2010; Barboni et al., 2021; Escudier et al., 2016; Hamad et al., 2006; Ioannou et al., 2017; Menna et al., 2012; Mkhinini et al., 2014; Pessini et al., 2018).

The use of infrared images, which measure the Sea Surface Temperature (SST) has allowed the detection of many oceanic eddies and a better understanding of regional circulations (Auer, 1987; Hamad et al., 2006; Millot, 1985). These detections were performed visually by expert oceanographers. However, due to the scarcity of in-situ observations, it was not until the intensive development of satellite altimetry and the development of automatic vortex detection algorithms on Sea Surface Height (SSH) (Chelton et al., 2011) that a statistical link between Eddy-induced Sea Surface Temperature Anomalies (eddy-SSTA) and SSH anomalies was established.

Several studies working on SST composites of eddies detected on the SSH associate warm eddy-SSTA with anticyclones and cold eddy-SSTA with cyclones (Frenger et al., 2013; Gaube et al., 2015; Hausmann et al., 2012). However through individual analysis of eddies various regional studies have shown the existence of inverse temperature anamolies i.e. anticyclones (respectively cyclones) with cold (warm) core anomaly. Hamad et al., 2006 performed observations of some cold core anticyclones on the summer period in the Eastern Mediterranean sea. Everett et al., 2012 observed the existence of an important fraction (70%) of inverse anomalies in the Tasman Sea eddy avenue. Assassi et al., 2016 built an index based on the SST anomaly of an eddy to distinguish between surface and subsurface structure. Leyba et al., 2017 found cyclones with a warm eddy-SSTA in the southwestern Atlantic ocean, which are explained through their (warm) region of formation. Trott et al., 2019 showed the existence of inverse anomalies in the Arabian Sea, while searching for a link between the

SST and MLD anomaly. Sun et al., 2019 performed similar observations in the North Pacific Ocean, and also showed a seasonal variability in the regional eddy temperature anomaly distribution, noting that these inverse anomalies appear for shorter times than the regular ones. In the same fashion, Liu et al., 2020 analysed the inverse eddy-SSTA in the South China Sea and noted a slight dependence on both seasonal effects and eddy amplitude. The last two studies, both link inverse anomalies with the summer re-stratification at the ocean surface.
The presence of cold-core anticyclonic and warm-core cyclonic eddies on a global scale has also been documented by two recent studies. Through a Deep Learning eddy identification method based on semantic segmentation, Liu et al., 2020 detected and classified eddies and their surface temperature anomaly. An important fraction of inverse anomalies is revealed around the globe, reaching up to 40%. The authors also showcase the seasonal variation of this fraction as well as an interannual trend of diminishing inverse anomalies. In the same manner Ni et al., 2021, showcases that inverse anomaly eddies have lower absolute eddy-SSTA values than their regular counterparts. Exhibiting strong seasonal variation, inverse anomalies cover according to this paper 15% of anticyclones (10% cyclones) on summer period. Finally the authors show correlation of this seasonal variation of eddy SST anomalies with the mixed layer modulation, along with the inversement of wind-stress and heat-flux patterns over these eddies. It should be noted that the percentages of inverse anomalies differs significantly between the aforementioned studies (regional and global) based on the method used to quantify them.
However, correlation does not imply causation, and even if some of the aforementioned articles create a strong observational link, regionally or globally, between the mixed layer modulation and the inversion of eddy-SSTA, none of them demonstrates an underlying mechanism for this phenomenon.

The goal of this work is to perform a comprehensive study on the formation of inverse sea surface temperature anomaly of mesoscale eddies, and propose an underlying physical mechanism. As a case study, observations in the Mediterranean Sea are examined, although our results can be expanded to other regions of the globe. Here, we attempt to answer four questions:

- *How does the eddy-SSTA distribution vary seasonally? :* We first define an eddy core surface temperature anomaly index to quantify the intensity of the eddy-SSTA for a large number of cyclonic and anticyclonic eddies in the Med Sea. This index allows us to perform a statistical analysis of the seasonal variations of the temperature anomaly inside coherent eddies and study its correlation with the evolution of the mixed layer depth.

- *How does the SST signature and anomaly of an individual mesoscale structure evolve? :* We investigate a few long-lived eddies to follow the temporal evolution of their SST anomaly with respect to their dynamical parameters and the seasonal stratification of the ocean surface.

- *Is the surface temperature anomaly linked with the subsurface structure? :* We quantify more precisely the evolution of the surface stratification inside and outside these selected eddies using ARGO profiles to estimate the eddy vertical temperature structure and compare it with the surface temperature anomaly.

- ***Why do inverse SST anomalies emerge? :*** We propose a mechanism based on differential vertical mixing between the eddy core and its periphery under atmospheric fluxes, illustrated with idealized single-column numerical simulations. The relevance of this physical model to explain the inverse emergence of inverse eddy-SSTA and its agreement with the remote-sensing and in-situ observations are discussed in the conclusion.

I.2 Satellite and in-situ data

This study focus on the mesoscale oceanic eddies of the Mediterranean Sea, during the three-year period 2016-2018. To perform our analysis, we combine satellite and in-situ data to characterize both the ocean surface and the subsurface stratification. The infrared satellite imagery provides the Sea Surface Temperature (SST) maps which are the core data of this study. We use the DYNED-Atlas database to obtain the dynamical parameters and the contours of mesoscale eddies detected on standard satellite altimetry products. The three dimensional structures of the studied eddies, as well as the surface stratification and the mixed layer depth (MLD) were derived from the in-situ Argo floats measurements.

I.2.1 Satellite Data

Daily, high-resolution (1/120°) super-collated SST maps of the Mediterranean Sea are received from the Copernicus - Marine Environment Monitoring Service (CMEMS), Ultra High Resolution L3S SST Dataset, produced by the CNR - Italy and distributed by CMEMS. The process of supercollation uses SST measurements derived from multiple sensors, representative of nighttime SST values (Nardelli et al., 2013).

Sea Surface Height (SSH) and geostrophic velocity fields, used in Figures of this study, are L4 altimetric products at 1/8°resolution retrieved from the CMEMS L4 Sea Level dataset.

I.2.2 Eddy contours, centers and tracks

The dynamical evolution of eddies and their individual tracks are retrieved from the DYNED-Atlas database for the three year period 2016-2018. The DYNED-Atlas project containing eddy tracks and their physical properties is publicly accessible . The tracking of these eddies is performed by the AMEDA eddy detection algorithm (Le Vu et al., 2018) applied on daily surface velocity fields, derived from the aforementioned SSH maps. A cyclostrophic correction is applied on these geostrophic velocities to accurately quantify eddy dynamical properties (Ioannou et al., 2019). Unlike standard eddy detection and tracking algorithms, the main advantage of the AMEDA algorithm is that it detects the merging and the splitting events and allows thus for a dynamical tracking of eddies (Le Vu et al., 2018).

The identification of potential eddy centers by AMEDA is performed by computing the Local Normalized Angular Momentum (LNAM) (Mkhinini et al., 2014) of the geostrophic velocity field. Only eddy centers with at least one closed contour of the stream function of the velocity field are retained. A radial profile of the velocity for each detected eddy center is calculated by computing the average velocity and radius at each closed streamline around it:

$$\langle V \rangle = \frac{1}{L_p} \oint \vec{V}\, d\vec{l} \tag{I.1}$$

$$\langle R \rangle = \sqrt{\frac{A}{\pi}} \tag{I.2}$$

The maximum velocity, obtained through equation IV.1, will be hereby noted as V_{max} and the radius corresponding to this characteristic contour, obtained through equation IV.2, will be noted as R_{max}. The eddy centers and their characteristic radius R_{max} are important parameters used to retrieve SST patches for each eddy detection.

I.2.3 Argo Floats

Hydrographic profiles of Argo floats are received through the CORIOLIS program database. Potential temperature and salinity profiles are received from Argo floats, through which the potential density profiles are derived. A co-localization is performed between the position of Argo floats and the detected eddies of the DYNED-Atlas database. Argo profiles are marked as inside an eddy if their distance r from any eddy center is $r < R_{max}$ and outside an eddy if the above condition is false for every eddy detection of the same day.

To calculate the Mixed Layer Depth (MLD) of each Argo observation, we use its potential density profile and search for the maximum depth at which a threshold of $\delta\rho = 0.03 kg/m^3$ is reached (Boyer Montégut et al., 2004).

I.3 Quantifying eddy-induced SST anomalies

Mesoscale eddies often have a visible signature on SST images, with a temperature difference between the waters in the eddy core and the waters in its periphery. This difference is hereby referred to as the eddy-induced surface temperature anomaly (eddy-SSTA) of an eddy, and can be quantified through our proposed methods.

A procedure to retrieve a large dataset of SST image patches containing eddy signatures is proposed, following (Moschos et al., 2020a,b). The Eddy-Core Surface Temperature Anomaly Index (δT), a simple and heuristic method for quantifying the eddy-induced temperature anomaly represented in each image,

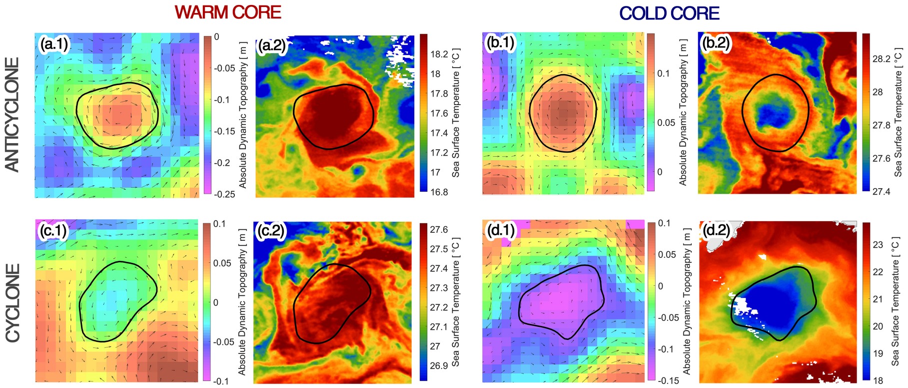

Figure I.1: **Samples of eddy induced SST anomalies** for a **(a)** Warm-Core Anticyclone, **(b)** Cold-Core Anticyclone, **(c)** Warm-Core Cyclone, **(d)** Cold-Core Cyclone. On the leftmost panels numbered with **(1)** the velocity vectors and the characteristic contour, computed by the AMEDA algorithm (black line) are superimposed on the Absolute Dynamic Topography. On the rightmost panels numbered with **(2)** the characteristic contour (black line) are superimposed on the patches of Sea Surface Temperature field centered on the detected eddy. Image patches are of side $5R_{max}$, chosen in order to include the temperature of waters

is then defined. The proposed methodology, applied here to observations in the Mediterranean Sea, is generic enough to provide results in every oceanic domain.

I.3.1 Eddy SST patches dataset

A thorough statistical analysis of eddy-induced SST anomalies requires a large data set of SST image patches in the Mediterranean Sea. The characteristic contours (highest mean velocity) of the mesoscale eddies contained in the DYNED-Atlas are used to crop patches from SST maps, centered on the detected eddies. These contours can either represent Anticyclonic Eddies (AE) or Cyclonic Eddies (CE) rotating clockwise and anti-clockwise respectively in the northern hemisphere. For each eddy, a square patch of size ($5R_{max} \times 5R_{max}$) is cropped, centered on the contour barycenter. Cloud coverage creates missing values on satellite SST images, and can corrupt the signature of the cropped image patches. Thus, only patches with less than 50% of cloudy pixels are retained.

As shown in the previous studies, the SST eddy signatures can be distinguished either as Warm-Core (WC) or Cold-Core (CC) anomalies. Four such cases are depicted in Figure I.1 that both positive and negative SSH anomalies can correspond to a Warm or a Cold SST anomaly. The characteristic contour of each eddy (in black) are superimposed on the Absolute Dynamic Topography (ADT), derived from the SSH, and the corresponding SST patch.

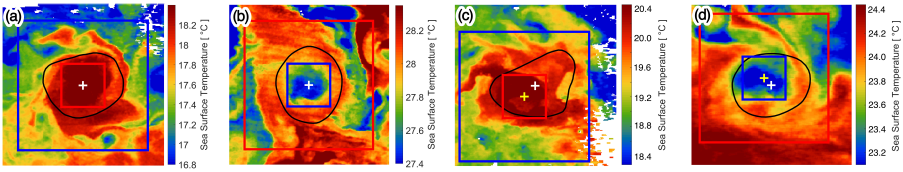

Figure I.2: **Examples of the Eddy-Core Surface Temperature Anomaly computation and offset method.**. Snapshots represent Sea Surface Temperature in degrees. Black lines are superimposed altimetric detection contours. Small squares represent the core-mean and large ones the periphery-mean frames. Core-periphery are coloured red-blue or blue-red based on the sign of δT. Examples (a)-(d) illustrate the correction by offset: A white cross marks the center of the image. A yellow cross marks the center of the core-mean and periphery-mean frames, if it differs from the center of the image. Examples (a) and (b) are centered while (c) and (d) are offseted.

I.3.2 The Eddy-Core Surface Temperature Anomaly Index [δT]

The Eddy-Core Surface Temperature Anomaly Index (hereby δT) is a simple and heuristic metric of the temperature difference between the core (center) of the eddy and its periphery. We define the core of the eddy as the region enclosed by the maximum velocity contour (Le Vu et al., 2018). The value of δT is calculated as the difference between the mean of the temperature values inside a *core-mean frame* and a *periphery-mean frame* in a given patch, with units in $°C$. These two square frames, which share a common center, have sides of R_{max} and $5R_{max}$, respectively, chosen in order to For the calculation of the mean value in the periphery-mean frame, the values contained in the core-mean frame are ignored. A positive δT value denotes a larger core-mean temperature than its periphery-mean temperature and thus a Warm Core Eddy, while a negative δT denotes respectively a Cold Core Eddy. The calculation of the δT variable by use of the core-mean and periphery-mean frames is shown in Figure I.2. Examples (a) and (b) show the two centered anomalies, shown also in Figure I.1 (a.2) and (b.2). The δT values are $0.75°C$ for the WC example (a) and $-0.27°C$ for the CC example (b).

However, the barycenter of the velocity contour can differ from the center of the eddy SST anomaly core, due to bias or errors of altimetric maps (Amores et al., 2018; Stegner et al., 2021). Therefore, an offset of both frames is considered, in order to locate the exact position of the maximum eddy-SSTA and correct the index value.

This correction is computed as follows: First, the value of δT is calculated through squares centered on the image, as described above. The sign of the eddy-induced SST anomaly is thus defined. Then, if δT is positive (negative) the warmest (coldest) core-mean value is searched for, by offsetting the core-mean frame in all directions with a stride of $\frac{1}{9}R$ and a maximum offset of $\frac{2}{3}R$. Finally, the periphery-mean frame is centered along the shifted core-mean frame and the

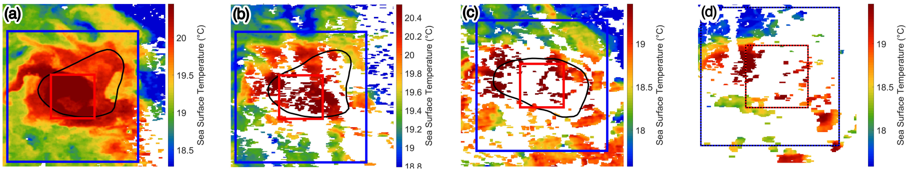

Figure I.3: **Examples with different Cloud Coverage**. Snapshots represent Sea Surface Temperature in degrees. Contours and squares are the same as Figure I.2. Snapshots of the same eddy (Ierapetra) on different days of December 2016 (a) 19/12 (b) 20/12 (c) 29/12 and (d) 30/12. Cloud coverage percentage is increasingly high. Examples (a) and (b) are retained while (c) and (d) are filtered

corrected δT value is computed. In the rest of this manuscript δT represents the final values calculated by applying the offset correction.

Examples of off-centered eddy detections are shown in Figure I.2 (c) and (d). The core and periphery have been shifted in order to maximize the eddy-core surface temperature anomaly index. The geometric center of the image is shown with a white cross, while the shifted center of the core-mean frame is shown with a yellow cross. The δT values are $0.68°C$ corrected to $0.86°C$ by offseting, for the WC example (c) and $-0.46°C$ corrected to $-0.55°C$ by offseting for the CC example (d).

Nevertheless, even with this correction a significant amount of noisy and/or corrupted SST signatures remain. This could be due to the combination of erroneous eddy detections on gridded AVISO/CMEMS altimetry products, large scale air-sea interactions that mask mesoscale eddy signature or the presence of clouds (Moschos et al., 2020a).

In order to exclude these images with unclear SST signatures, two thresholds are considered. The Cloud Coverage threshold, described above is used to retain only images that contain less than 50% of cloudy pixels. This criterion is applied twice: on the whole image patch (CCP_{patch}), as well as the core-mean frame (CCP_{frame}). The threshold is chosen so that the eddy SST signature is not corrupted creating error in the retained δT value (Moschos et al., 2020a).

An illustration of the application of the Cloud Coverage threshold is provided in Figure I.3 (e)-(h), where snapshots of the SST signature of the same eddy (Ierapetra) are provided at different days of December 2016, along with core-mean and periphery-mean frames. Example (a) on 19/12 shows a patch with an overly clear eddy signature ($CCP_{patch} = 8\%$,$CCP_{frame} = 0\%$), retained in the dataset. Example (b) on 20/12 shows a patch with an eddy signature covered by clouds ($CCP_{patch} = 40\%$,$CCP_{frame} = 48\%$), which however do not surpass the 50% threshold and is retained in the dataset. Examples (c) on 29/12 ($CCP_{patch} = 48\%$,$CCP_{frame} = 90\%$) and (d) on 30/12 ($CCP_{patch} = 72\%$,$CCP_{frame} = 76\%$) show patches exceeding the Cloud Coverage threshold and therefore filtered from the dataset.

Finally a filter on weak δT values is also applied. We have noticed by visual inspection that unclear SST signatures often induce a week value of the δT. Hence, to filter out these noisy images we retain only SST patches if $|\delta T| > 0.1$ (see next section and Figure I.5 for the filtering threshold choice).

I.4 Seasonal variations of the eddy-induced temperature anomaly

I.4.1 Statistical analysis

Composite averages are often employed in the bibliography to represent the SST anomaly of mesoscale eddies (Frenger et al., 2013; Gaube et al., 2015; Hausmann et al., 2012). This averaging leads frequently to the association of a warm-core anomaly to anticyclonic eddies and a cold-core anomaly to cyclonic eddies.

To examine these average temperature anomalies we calculate here the composites of all eddy SST patches retained, after first performing a normalization per patch. To receive the Normalized SST Anomaly, we subtract from each pixel the mean value of all the SST values of the patch and divide the result by the standard deviation of all the SST values of the patch. In Figure I.4 composites of Anticyclonic and Cyclonic Normalized SST Anomaly are plotted for all eddies and those observed on the Winter (December-January-February) and Summer (May-June-July) period. These two oceanic seasons are chosen on the three months period when the mean value of the mixed layer depth (MLD), computed outside the detected eddies, reaches its largest or smallest value (see Figure I.6).

From the composites of Figure I.4 it can be seen that the average SST anomaly of all anticyclonic (cyclonic) observations indeed corresponds to a warm-core (cold-core) structure, or else the regular eddy anomaly. Nevertheless, a strong seasonal variation of this average anomaly is revealed by plotting the winter and summer composites. On winter, the regular anomaly is even more pronounced with double to triple normalized anomaly values. On summer, the average anomaly is inversed with a weaker however normalized anomaly values.

While composites suffice to portray the seasonal inversion of eddy temperature anomalies, averaging out patch values does not retain the variance in eddy anomalies on the SST. To quantify thus the latter we perform a statistical analysis of the δT index values computed for all the patches retained.

The histograms of the δT index are shown in Figure I.5, separately for anticyclonic and cyclonic eddies, at winter (DJF) and summer (MJJ). On the histograms, red bins represent warm-core observations, while blue bins represent cold-core observations. Grey bins represent observations where $|\delta T| < 0.1$. These bins correspond to outlier values, linked with the noise on the SST data as well as errors on the sensors observation and our method. A threshold of $|\delta T| > 0.1$ is fixed to filter out these observations in the analysis/figures that follow.

If we consider a year-long statistical distribution, AE are predominantly Warm Core and CE are predominantly Cold Core, in other words AE and CE, exhibit on average a *regular* anomaly on the SST. However, the distribution of δT values in the histograms of Figure I.5 suggest that the eddy-core temperature

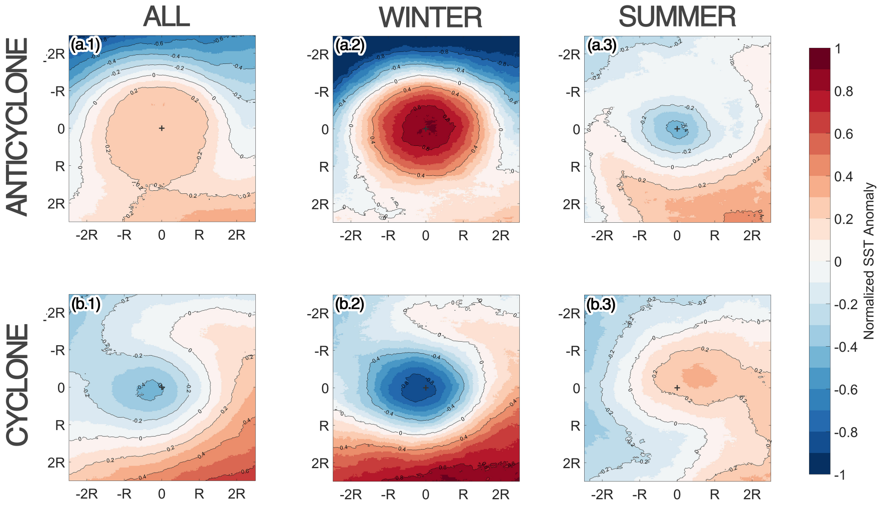

Figure I.4: **Composite averages of Normalized SST Anomaly** for (a) Anticyclonic and (b) Cyclonic eddies, for (1) all (2) winter (DJF) and (3) summer (MJJ) observations. Each value in an eddy SST patch is normalized by subtracting the mean value and dividing by the standard deviation of all values. Composites are retained by averaging between patches.

anomaly exhibits strong seasonal variation, altering between Warm Core and Cold Core anomaly regimes. Specifically, during winter the regular anomalies are preponderant: 93% of AE observations correspond to Warm Core eddy and while 92% of CE observations being Cold Core. However, during summer, Cold Core AE and Warm Core CE observations become dominant with respectively 69% and 66% of the observations. It is due to this seasonal inversion of the regular anomaly, that we name the Cold Core AE and Warm Core CE as *inverse* SST anomaly.

The seasonal cycle of the eddy-SSTA of both AE and CE, in the Mediterranean Sea, coincides with the seasonal variation of the Mixed Layer Depth (MLD). This is portrayed in Figure I.6, were the monthly variation of the percentage of inverse eddy core anomalies is plotted along with the monthly variation of the MLD. The later is calculated as the mean of all Argo profiles that are located outside eddies. The winter mixing period (DJF) when the mean MLD is at its largest extent, coincides with the period when inverse anomalies appear with the lowest percentage between $5-15\%$ for both AE and CE. Conversely, the end of the spring re-stratification period (MJJ) when the mean MLD is at its shallowest, coincides with the period when inverse anomalies appear at their highest percentage, reaching a peak of 70% of cold-core AE and warm-core CE observations for the months of May and June.

The seasonal variation of the core anomalies and their summer inversion, seen on Figures I.4, I.5 and I.6 is also analysed spatially. In Figure I.7 we plot the δT

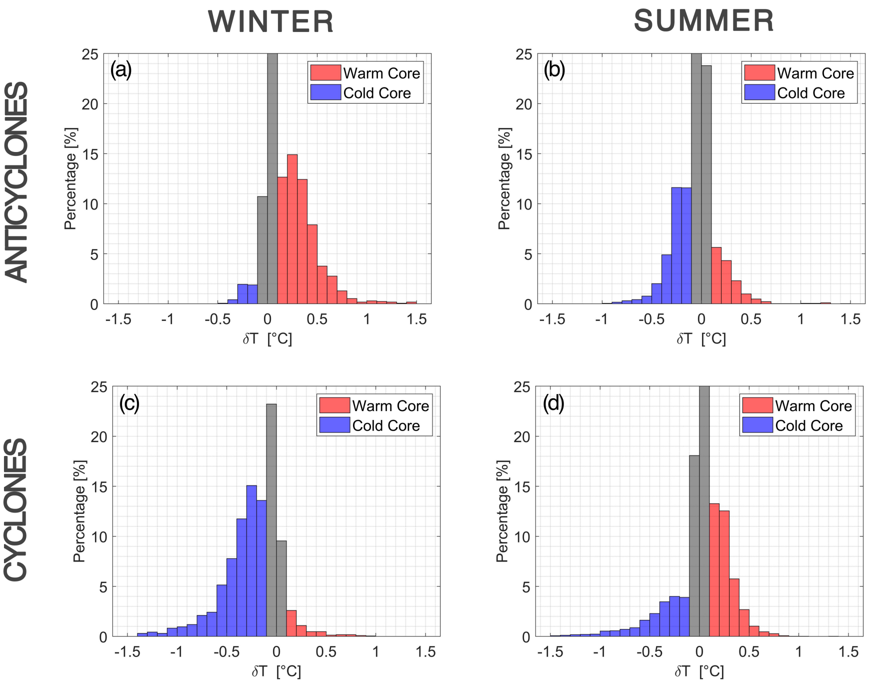

Figure I.5: **Seasonal histograms of δT values**. **(a)** AE in the winter mixing period (DJF), **(b)** AE in the summer restratification period (MJJ), **(c)** CE in the winter mixing period (DJF) and **(d)** CE in the summer restratification period (MJJ). Red bins represent positive δT warm-core observations while blue bins negative δT cold-core observations. Grey bins represent observations where $|\delta T| < 0.1$.

values of all anticyclonic/cyclonic eddy detections in the Mediterranean Sea for one winter (DJF) and one summer (MJJ) season. The predominance of regular anomalies (WC AE, CC CE) on winter (panels a and c) and inverse anomalies (CC AE, WC CE) on summer (panels b and d) is spatially homogeneous over the Mediterranean Sea. Regular temperature anomalies, reach higher absolute values as can be seen by the intense red dots (i.e. warm-core anticyclones on panels a and b) and blue dots (cold-core cyclones on panels c and d). The inverse anomalies have lower absolute values, as portrayed in the histograms of Figure I.5.

I.4.2 Individual eddy analysis

To better investigate how the seasonal evolution of the surface stratification inside mesoscale eddies impacts their surface temperature signature, we track four long-lived eddies and followed the temporal evolution of their dynamical

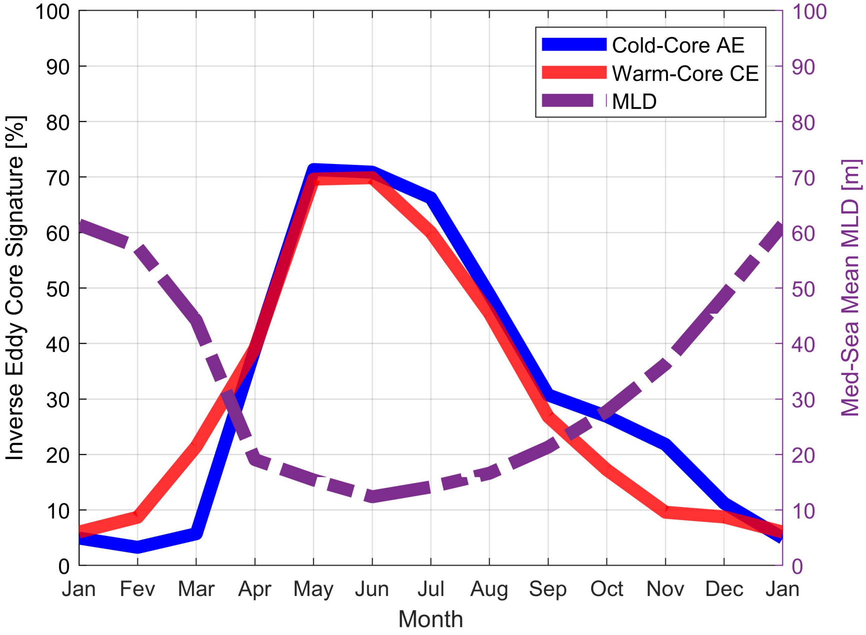

Figure I.6: **Seasonal variation of the Mean MLD with inverse eddy anomaly percentage.** For each month the mean percentage of Cold-Core AE observations is plotted with a blue line, the mean percentage of Warm-Core CE observations with a red line and the mean MLD of all Argo profiles located outside eddies with a dashed purple line.

parameters, the surrounding MLD and their surface SST anomaly. One of them, an Ierapetra Anticyclone, formed south of the island of Crete, was sampled for over a year by a few Argo floats trapped inside its core. Three more eddies are considered: a Cyprus anticyclone located among and around the Eratosthenes seamount, an Algeria Anticyclone drifting along the Algerian coast and an elongated cyclone located in the Ligurian sea. The timeline of the Ierapetra eddy is shown in Figure I.8, while those of the Algeria, Cyprus and Liguria eddies are shown respectively in Figures I.12, I.13, I.14 of the Appendix.
For each of these four eddies we create an *Eddy Timeline*, that contains the δT index, the evolution of the mixed layer depth (MLD) in the eddy area, the eddy intensity and a few characteristic snapshots of the eddy SST signature. Moreover, to highlight the seasonal variations a monthly mean average (MMA) is calculated for each parameter. The daily value of the Core Temperature Anomaly Index (δT), are plotted when the cloud coverage is not too high and the temperature anomaly not too small (i.e. $|\delta T| > 0.1$). The calculated (δT) (dots) as well as the corresponding MMA (line) are coloured in red (blue), when their value is positive (negative), denoting a warm (cold) core regime.

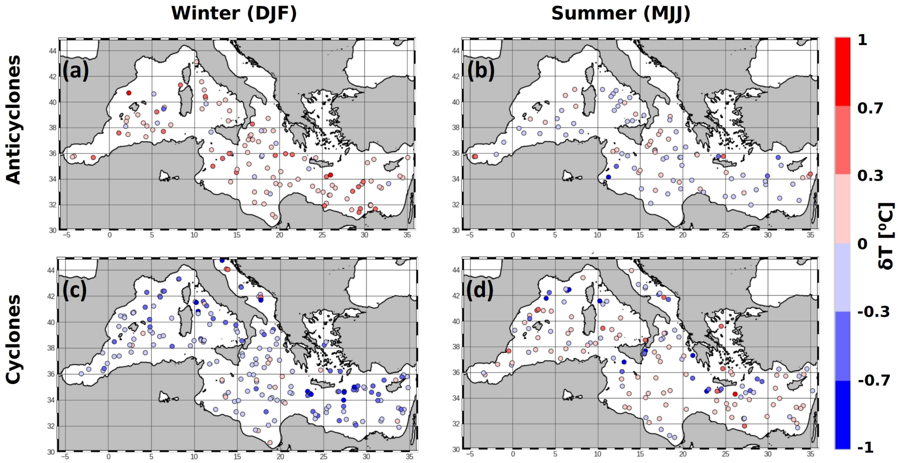

Figure I.7: **Spatial variation of δT values in the Med Sea** for **(a)** Anticyclones in Winter **(b)** Anticyclones in Summer **(c)** Cyclones in Winter and **(d)** Cyclones in Summer. Red (Blue) dots correspond to warm (cold) anomalies. The colour intensity shows the absolute value of the anomaly.

To construct the MLD time series (pink dots), we use all the Argo profiles that were measured outside the eddy contour in a surrounding area, defined as a rectangular box of one degree of latitude and longitude, centered on the eddy. More than one MLD observation might exist for a certain day, causing a spread of values especially for the winter mixing period. When in-situ measurements are available inside the eddy contour, the MLD is plotted with black dots. The variations of the eddy intensity, quantified here by V_{max}, is plotted during the same period. In order to highlight the seasonal variations, we use distinct colors for the velocity above (magenta) and below (cyan) the mean velocity value averaged over the whole period.

Our analysis is focused on the evolution of an Ierapetra Anticyclone from September 2016 to September 2018. According to the figure I.8, this anticyclone changes regime twice from a regular to an inverse anomaly. The inverse sea surface temperature anomaly begins in spring, when the re-stratification sets in, and continues until fall.

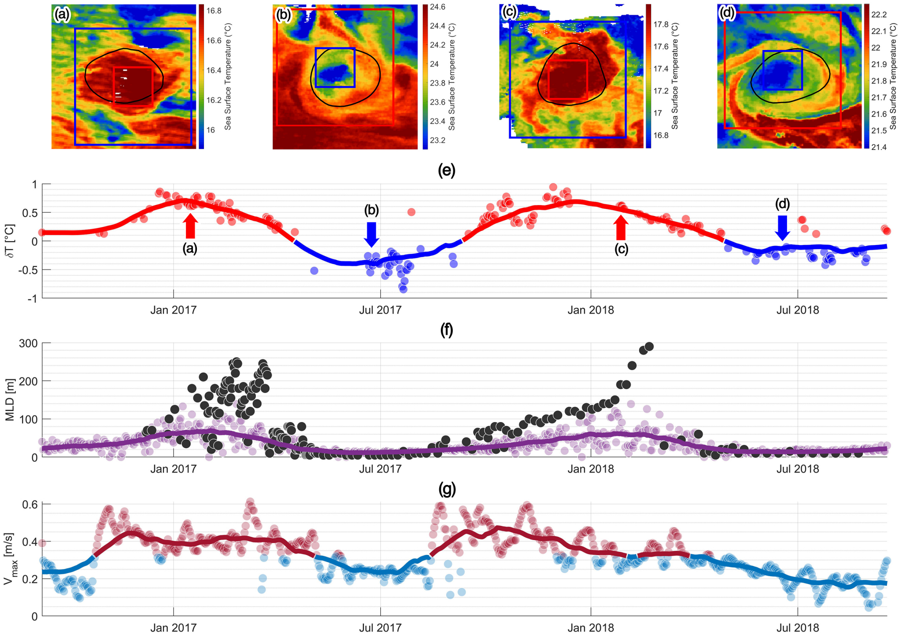

Figure I.8: **Timeline of the Ierapetra Anticyclone** with DYNED ID #11099. Four characteristic SST patches are shown in panels (a)-(d) which corresponds to different regimes of the evolution of the eddy SST anomaly, shown in panel (e): the δT index values are plotted for every retained observation with red (blue) dots for positive (negative) values. The MMA of these values is plotted with a red (blue) line showing the regime change between a warm-core (cold-core) eddy. On panel (f) the depth of the mixed layer (MLD) is plotted with pink dots for values outside the eddy and black dots inside the ierapetra eddy. A MMA of the MLD evolution outside the eddy is plotted with a pink line. On panel (g) the surface maximal velocities (V_{max}) for each timestep in the DYNED-Atlas eddy track are plotted with dots and their MMA with a line. Velocities are plotted with magenta (cyan) when they are higher (lower) than the mean velocity in the eddy lifetime.

As can be seen in panel (f) of Figure I.8, on winter months, while the eddy is a warm-core regime in panel (e), the MLD is two or three times deeper inside the ierapetra anticyclone than in its surroundings, reaching 300 meters of depth while being shallower than 120 meters in its surroundings. The warm-core surface anomaly of the eddy (panels (a) and (c)) can be linked therefore with its subsurface heat content. On the other hand, during the spring re-stratification period and a cold-core regime, the MLD is rather shallow, not exceeding a few tens of meters both inside and outside the anticyclone. The cold-core surface anomaly (panels (b) and (d)) is disconnected from the warm subsurface heat content. It should also be noted, that it is during the winter months, when the

MLD is deeper in the eddy core, that the anticyclone passes an intensification phase shown in the evolution of the surface velocity V_{max}.
Similar regime transitions from a regular to an inverse sea surface temperature anomaly are visualized in the supplementary material of this article for a cyclonic eddy in Figure S1 as well as for two other anticyclones in Figures S2 and S3. For all these eddies the inverse sea surface temperature anomaly, is directly correlated to a small MLD in the eddy surrounding. This indicates a strong surface stratification on the same period and thus a disconnection of the inverse surface anomaly with the subsurface heat content.

To investigate if the change in the surface core temperature anomaly is linked with the subsurface anomaly of the Ierapetra anticyclone two profiles from an ARGO float released inside the core of the eddy are examined. From a series of observations, the profiles are chosen on two dates where the SST signature of the eddy is not corrupted by clouds and the in-situ profile samples well the eddy core. On winter a regular warm-core observation, on the 26 February 2017 can be seen in panel (a.2) of Figure I.9, corresponding to panel (a) of Figure I.8. On summer a regular warm-core observation, on the 26 of June 2017 can be seen in panel (b.2) of Figure I.9, corresponding to panel (b) of Figure I.8. On these panels a white star corresponds to the location of the eddy-sampling ARGO float. On panels (a.1) and (b.1) of Figure I.8 the location of the eddy-sampling floats are shown with a star in a wider map, where we also plot the region (dashed rectangle) where we search for background-sampling ARGO floats. We consider a ± 1 week period from the observation date and search for ARGO profiles in that region that fall outside of eddies. The temperature measurement of these background outside-eddy profiles is plotted with dashed gray lines on panels (c) and (d) of Figure I.8 while their mean is plotted with a thick black line. The eddy-sampling profile is plotted on panels (c) and (d) of Figure I.8 corresponding to the winter and summer periods respectively. When eddy-sampling profile is warmer (cooler) than the mean outside-eddy profile it is plotted with a thick red (blue) line.
Due to the deep winter mixed layer, the warm core SSTA extends down to 250m (Fig.I.9 (c)). On this winter profile, the core of the anticyclone is always warmer that its surrounding down to 1000m. An inversion of the eddy-SSTA is visible on the summer profile (Fig.I.9 (d)). However this cold core temperature anomaly does not extend below a few tens of meters (Fig I.9 (e)). Below the strong summer stratification, at -100m for instance, the core temperature of the anticyclone is warmer than its surrounding waters whose temperature is portrayed by the mean outside-eddy profile (black line in Figure I.9 (d)). The subsurface temperature anomaly reaches a positive value of $+1°C$ at 500m, which is coherent with other observations of long-lived anticyclonic eddies in the region (Barboni et al., 2021; Moutin et al., 2012). Hence, these unique in-situ measurements indicate that the inverse eddy-SSTA remains confined to a few dozen meters below the ocean surface and does not correspond to the deep subsurface heat content of the anticyclone.

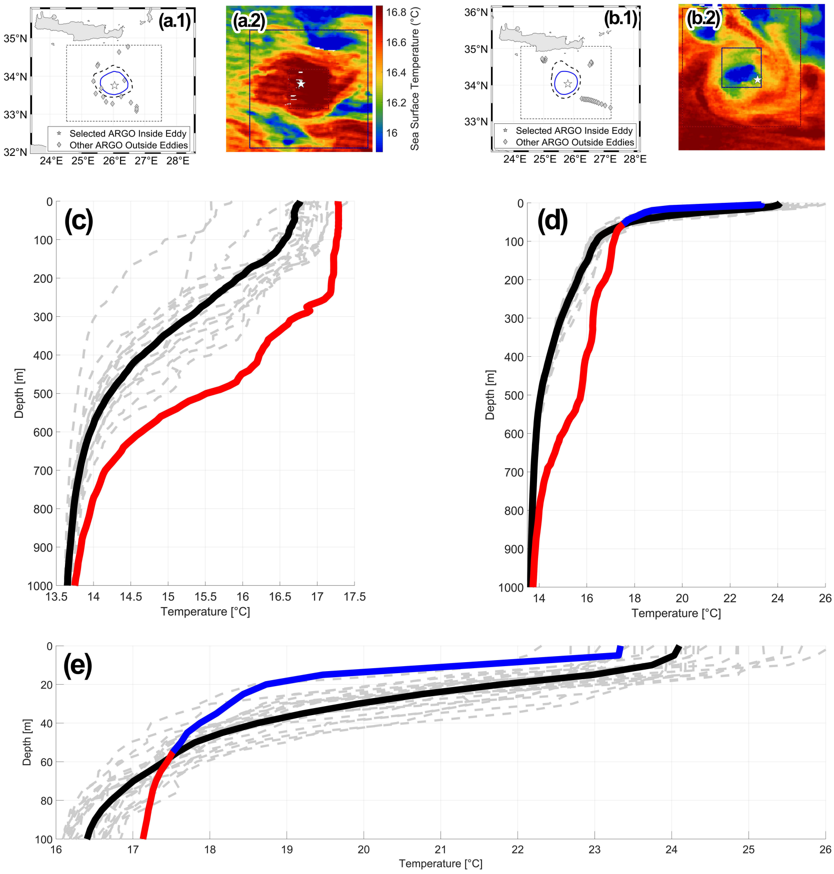

Figure I.9: **Seasonal evolution of the vertical structure of the Ierapetra eddy**. Panels (a) and (c) correspond to a warm-core SST observation of the eddy, on 26/07/2017. Panels (b), (d) and (e) correspond to a cold-core SST observation on 26/07/2017. Maps (a.1) and (a.2) show the maximum velocity contour and outermost contour of the eddy, the eddy-sampling ARGO profile with a star and the outside-eddy profiles with diamonds, retained in a region outlined by the dashed rectangle in a period of ± 2 weeks from the eddy observation. Patches (b.1) and (b.2) show the SST anomaly of the eddy, along with the location of the eddy-sampling profile, plotted with a star. Vertical plots (c), (d) and (e) show the outside-eddy profiles plotted with dashed gray lines and their mean outside-eddy profile with a thick black line. The eddy-sampling profile is plotted with a thick red (blue) line when it is warmer (colder) than the mean outside-eddy profile. Profile (c) shows the winter regular surface anomaly, with a warm structure, profile (d) the summer inverse surface anomaly with a cold surface and a warm subsurface structure, while panel (e) zooms into the 100 first meters of (d) to portray the SST inversion.

I.5 A mechanism of SST anomaly inversion: Single column simulations

The above individual-eddy viewpoint analysis portrays that the winter mixed layer varies significantly inside long-lived mesoscale eddies, particularly in the core of anticyclones. But is this MLD difference between the core of the eddy and its vicinity sufficient enough to explain the inverse eddy-SSTA that occurs during the spring re-stratification ?

To answer this question, and investigate other hypotheses, we use a simplified 1D model of the vertical advection-diffusion of heat in a stratified water column inside and outside mesoscale eddies. The seasonal forcing of the atmosphere is simulated with a sinusoidal surface temperature flux as $Q = Q_0 sin(2\pi t/365.25)$ ($Q_0 > 0$, positive for ocean heat gain), so that the simulation starts with a temperature flux increasing from zero (corresponding to spring). A value of $Q_0 = 150\, W/m^2$ is chosen as an accurate Mediterranean average of total surface heat flux seasonal cycle, following Pettenuzzo et al., 2010, with a negative (positive) maximum heat flux approximately in December (July). As salinity effects are neglected, the temperature flux is equivalent to the buoyancy flux.

An equal surface heat flux is applied for different temperature profiles corresponding to water columns inside a cyclone, anticyclone and a profile outside an eddy respectively. The simulation starts on the end of the winter period, when the MLD is at its deepest. The initial profiles are described analytically in equation I.3, whose parameters are chosen so that the simulated profiles represent average temperature profiles in the Mediterranean sea. These stand for a homogeneous MLD of $Z_{MLD} = 50\, m$ at $T_0 = 16°C$ for a cyclone core, $200\, m$ at $18°C$ for an anticyclone core and $100\, m$ at $17°C$ for the outside-eddy profile. Below the mixed layer, we introduce an exponential decrease (typical thickness $Z_T = 150m$) to a deep ocean value of $T_b = 13.5°C$. The $T(z)$ profiles are plotted on panels (b) and (d) of Figure I.10, with a blue, red and black line for the anticyclone, cyclone and outside-eddy profiles respectively.

$$\begin{aligned} T(z) &= T_0 && ;\ \text{if} z > Z_{MLD} \\ T(z) &= T_b + (T_0 - T_b) exp\left(\frac{z - Z_{MLD}}{Z_T}\right) && ;\ \text{if}\, z < Z_{MLD} \end{aligned} \tag{I.3}$$

Vertical profiles are forced by the surface heat flux, and in a one-dimensional space the temperature temporal evolution follows a simple diffusion equation I.4. We additionally assume a steady turbulent mixing coefficient $A(z)$ which depends only on depth. This vertical mixing profile is set by the equation I.5, starting from a surface value A_0 down to a deep ocean value A_{back} with a Gaussian vertical shape, with $Z_T = 150\, m$. Static instability (i.e. $\partial_z T < 0$) are inhibited by simply boosting the mixing coefficient $A(z)$ to $1 m^2/s$.

$$\frac{\partial T}{\partial t} = \frac{\partial}{\partial z}\left(A(z)\frac{\partial T}{\partial z}\right) \tag{I.4}$$

$$A(z) = A_{back} + A_0 e^{-(z/Z_T)^2} \tag{I.5}$$

We first assume that the vertical mixing profile remains the same in the cyclone, the anticyclone and outside-eddy. The surface value A_0 of $10^{-4} m^2.s^{-1}$ is chosen as a typical value for turbulent mixing in the upper ocean while in the deep ocean the mixing is reduced by two orders of magnitude down to $A_{back} = 1.0 \times 10^{-6} m^2.s^{-1}$, the water kinematic viscosity.
The uniform vertical mixing profile, common for both three water columns, is plotted in panel (a) of Figure I.10, while the response of the three water columns (anticyclone, cyclone, outside-eddy) is plotted in panel (b). The simulation starts from a deep-MLD profile at the end of the winter mixing period (dashed line). During spring re-stratification, positive surface is transferred downwards at the same rate for all water columns. As a consequence, the surface temperature difference between the three winter profiles is also maintained in summer (continuous line). This effect is also observed in panel (b) of Figure I.11 where the seasonal evolution of the SST of the three water columns, is plotted on a 18-month period. The anticyclonic (cyclonic) profile is constantly warmer (colder) than the outside-eddy profile. A two month lag between the surface flux of Figure I.11 panel (a) and the SST of panel (b) is explained through the delay needed for the water column to integrate the radiative forcing.

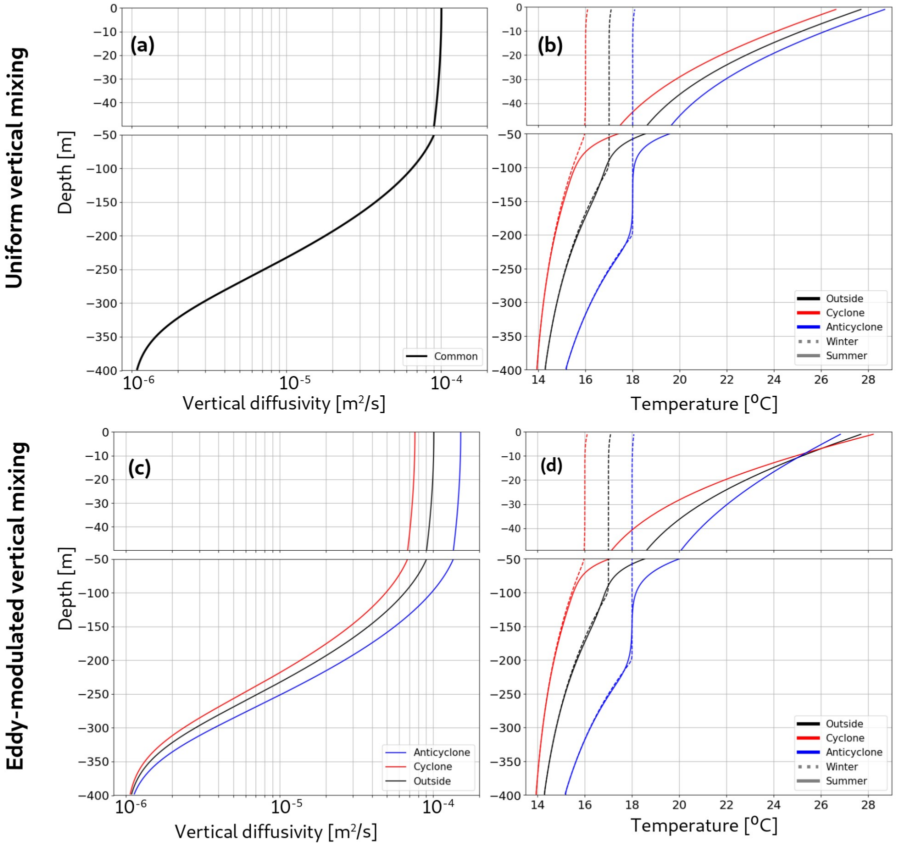

Figure I.10: **1D single column experiments : vertical structure**. With a uniform vertical mixing : (a) vertical diffusivity $A(z)$ from equation I.5, and (b) temperature profiles in winter (dashed line) and summer (continuous line), corresponding time of the year being reported on Fig.I.11b . Initial winter profiles are set in equation I.3. With eddy-modulated vertical mixing : (c) vertical diffusivity and (d) temperature profiles.

The initial differences of temperature profiles and winter MLD are not sufficient to reproduce observed eddy-SSTA inversion, suggesting that an additional physical process is missing. To explore such a mechanism, we assume that the vertical mixing coefficient is, on the one hand, enhanced in the core of anticyclonic eddies and, on the other hand, reduced in the core of cyclonic eddies. To test this hypothesis, we perform another set of heat vertical diffusion experiment, with the same vertical profiles (equation I.3) and diffusion process (equations I.4 and I.5), but with a varying surface vertical diffusivity value. A_0 stays outside-eddy at $1.0 \times 10^{-4}\, m^2.s^{-1}$ but is divided by a factor 2 to $5.0 \times 10^{-5}\, m^2.s^{-1}$ in the cyclone profile, and multiplied by 2 to

$2.0 \times 10^{-4}\, m^2.s^{-1}$ in the anticyclone one. These eddy-modulated vertical mixing profiles are plotted in panel (c) of Figure I.10 with a blue/red/black colour representing the anticyclone/cyclone/outside-eddy profile.

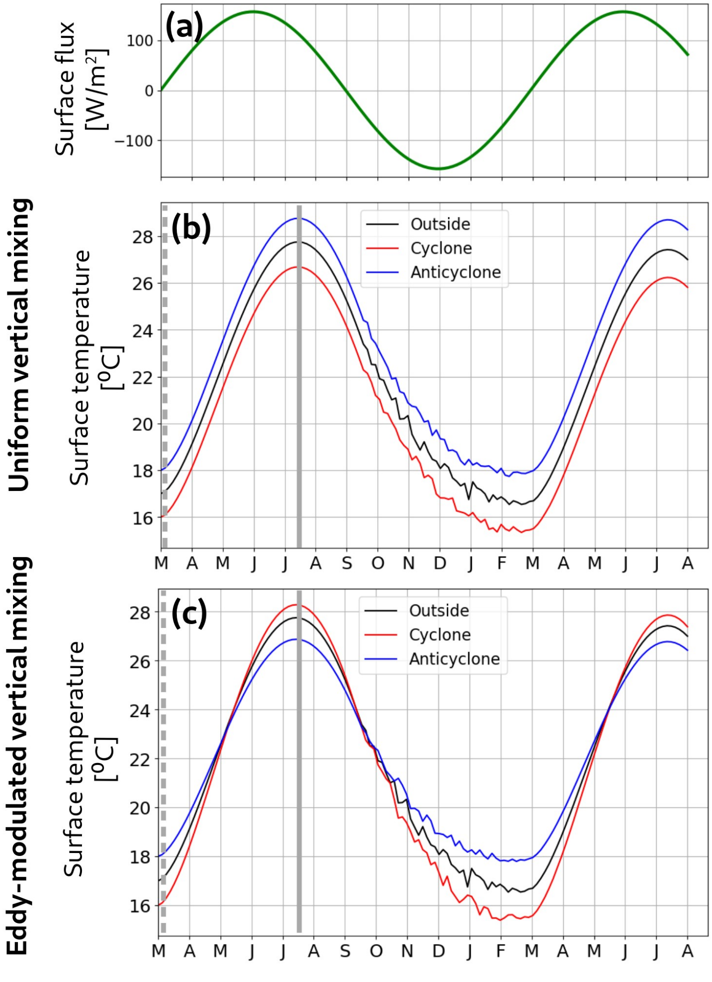

Figure I.11: **1D single column experiments : surface temperature**. (a) Surface heat flux forcing the simulation (b) Surface temperature evolution for anticyclone, cyclone and outside-eddy profiles with a uniform vertical mixing and (c) same as (b) but with an eddy-modulated vertical mixing, shown in Fig.I.10 (c).

Through the season evolution results of the eddy-modulated vertical mixing model, shown in panel (d) of Figure I.10, it is observed that heat penetrates deeper in the vertical structure of the anticyclone, resulting in a less stratified profile in summer (blue continuous line). Vice-versa, heat reaches a shallower depth of the cyclone, resulting in a more stratified summer profile (red continuous line). The vertical diffusivity difference is strong enough so that the anticyclone (respectively cyclone) profile gets cooler (warmer) than the outside-eddy profile, resulting in an isotherm crossing similar to what was observed in the Ierapetra anticyclone, seen at panel (e) of Figure I.9.

The evolution of surface temperature given by the eddy modulated vertical mixing model, shown in panel (c) of Figure I.11 for more than a year and a half, reproduces the same SST anomaly summer inversion in cyclones and anticyclones. The column representative of an AE (CE) core is indeed warmer (colder) in winter at the surface than a column representative of an outside-eddy profile stratification, while turning colder (warmer) in summer, implying that an inverse SST anomaly has emerged.

These simplified 1D model simulations show that, despite initial differences in vertical stratification or MLD, a differential mixing coefficient, between the core and the periphery of oceanic eddies, is needed to explain the inverse sea surface temperature anomalies which emerge during the spring re-stratification period.

I.6 Discussion

The emergence of inverse eddy SST anomalies during the summer season, in the global ocean as well as in regional seas, has been well-documented by recent studies (Leyba et al., 2017; Liu et al., 2020; Ni et al., 2021; Sun et al., 2019; Trott et al., 2019). Some of them also link this inversion of eddy surface anomaly with the spring re-stratification of the ocean surface. This study confirms that such seasonal correlation is also valid for the Mediterranean Sea (Figure I.6). Nevertheless, we showcase here that the difference in the MLD alone is a necessary but not sufficient condition for the emergence of an inverse eddy SST anomaly. We consider thus the hypothesis that eddies modulate the diapycnal mixing in their interior creating a vertical spacing (tightening) of isopycnals in anticyclones (cyclones). Our 1D single column modelling experiment (Figures I.10 and I.11) shows that a modulation of vertical mixing $A(z)$ inside eddies is needed to reproduce the inversion of the eddy-induced SST anomalies during summer. The origin of this vertical mixing modulation might stem from 3D dynamical processes that cannot be reproduced explicitly in the 1D vertical model.

Some hypotheses exist in the bibliography, and several papers studied the trapping of Near-Inertial Oscillations (NIO) in anticyclones either through a theoretical formulation (Kunze, 1985; Young et al., 1997), or through modelling experiments (Danioux et al., 2015; Klein et al., 2001; Lelong et al., 2020) and observations (Elipot et al., 2010). Enhanced turbulent mixing at depth was also reported when NIO were trapped inside anticyclones (Martinez-Marrero et al., 2019; Whalen et al., 2018). Nevertheless, we are not aware of a theoretical study that provides a direct link between the trapping of NIO and enhanced vertical mixing in the thermocline layer. The opposite trend for cyclones is still under discussion. However, due to the effective Coriolis parameter $f_{eff} = f + \zeta$, which is higher for positive vorticity area ($\zeta > 0$), the spectrum of NIO is expected to be reduced in the core of cyclonic eddies (Kunze, 1985; Young et al., 1997). This impact of NIO within the eddies is a very plausible explanation of the differential vertical mixing and the observed eddy-SSTA asymmetry between cyclone and anticyclones. Nevertheless, other mechanisms could also be responsible of inverse eddy SST anomalies such as nonlinear wind-induced Ekman pumping.

Motivated by the impact of eddies on biological productivity, several studies investigate the self-induced Ekman pumping in the core of mesoscale cyclones and anticyclones. Local currents induced by coherent eddies generate a curl to the surface stress from the relative motion between surface air and water, even if the wind stress is uniform. Hence, an uniform wind applied to an anticyclonic eddy can lead to a divergence and upwelling in its core (Gaube et al., 2015; Ledwell et al., 2008; McGillicuddy Jr, 2016)). A local upwelling could therefore induce a cold core anomaly for anticyclones. However, such a mechanism depends directly on the eddy intensity and we didn't find on the data of this study, any correlation between the amplitude of the temperature anomaly in the core of the eddy and its intensity. Nevertheless, to investigate in more details the impacts of the wind-induced Ekman pumping on the emergence of inverse eddy SST anomalies a full 3D numerical simulation will be performed in a future work.

I.7 Summary and Conclusions

The emergence of inverse eddy SST anomalies, in the Mediterranean Sea, is a global seasonal phenomenon that affects all mesoscale eddies. Remote-sensing and in-situ observations were used to detect and quantify the eddy induced SST anomaly over a 2 years period (2016-2018). We build an eddy core surface temperature index to quantify the amount of Cold Core Anticyclones and Warm Core Cyclones all over the year and especially during the spring re-stratification period. We find that these inverse eddy anomalies could reach a peak of 70% in May and June. This seasonal cycle coincides with the seasonal variation of the MLD, both through a statistical analysis, on a basin scale, and through an individual analysis for long-lived eddies. By tracking these eddies we find that some of them alternate several times, from one season to another, between a warm-core and a cold-core SST anomaly. However, the inverse eddy anomalies are constrained to the upper layer of the ocean. For instance, co-localizing ARGO profiles in cold-core anticyclonic eddies reveals that their cold temperature anomaly inversion is limited to the first 50 meters of the ocean, while a warm subsurface anomaly persists deeper.

We propose a simple dynamical mechanism, based on a differential mixing between the eddy core and its surroundings, that leads to reproducing cold-core (warm-core) anticyclones (cyclones) during the spring re-stratification period. To do so, we construct a simple vertical column model to compute the impact of the seasonal air-sea flux on the vertical stratification inside and outside eddies. We start off by a winter stratification setup with a deep mixed layer, and investigate how the spring re-stratification of the ocean surface differs between the eddy core and its surrounding. By considering only the MLD difference, we were not able to reproduce the inverse eddy-SSTA that are observed during the spring re-stratification period in satellite data. It is only by taking into account a differential diapycnal eddy mixing - increased in anticyclones and diminished in cyclones - that we reproduce correctly the surface temperature inversion in the eddy core, with respect to an outside-eddy profile. This simplified model, suggests that vertical mixing modulation by mesoscale eddies might be the key mechanism that leads to the eddy-SSTA seasonal inversion in the ocean. Besides, even if our study focuses on the Mediterranean Sea, the mechanism proposed here is, a priori, independent of the oceanic region.

Several theoretical studies on near inertial oscillations and corresponding in-situ observations could explain the modulation of the vertical mixing induced by oceanic eddies and the cyclone/anticyclone asymmetry. However, full 3-dimensional modelling is necessary to further investigate these dynamical modes in combination with the wind-induced Ekman pumping inside the eddy core. Such high-resolution simulations are beyond the scope of this study and consist the perspectives of a future work.

Lastly, this study showcases that a detailed analysis of remote sensing observations of the complex eddy signature at the ocean surface could reveal its subsurface structure in the first tens of meters. This would provide valuable information on the vertical extension of the mixing layer or the bio-geochemical activity in the euphotic layer.

I.8 Supplmetary: Eddy Timelines

We provide three additional eddy timeline of long-lived eddies: an Algeria Anticyclone (Figure I.12), a Cyprus (Eratosthenes) Anticyclone (Figure I.13) and a Liguria Cyclone (Figure I.14). The figure is refered to Figure I.8 (timeline of the Ierapetra long-lived eddy) in the main corpus of the text for detail description of this timeline as an individual eddy analysis of the sea surface temperature anomaly evolution.

We note several differences compared with the Ierapetra anticyclone: The Algeria anticyclone in the western Mediterranean shows the same swift between cold-core anomaly (summer) to warm-core anomaly (winter), while having a smaller local MLD than the Ierapetra eddy. The Cyprus Anticyclone in the eastern Mediterranean shows a persistent inverse cold-core anomaly ranging from May to December, while the regular warm-core anomaly appears only for few winter months. Finally the Liguria cyclone shows that the shift between regular and inverse anomalies can also emerge for long-lived cyclone, corresponding also with the MLD seasonal cycle.

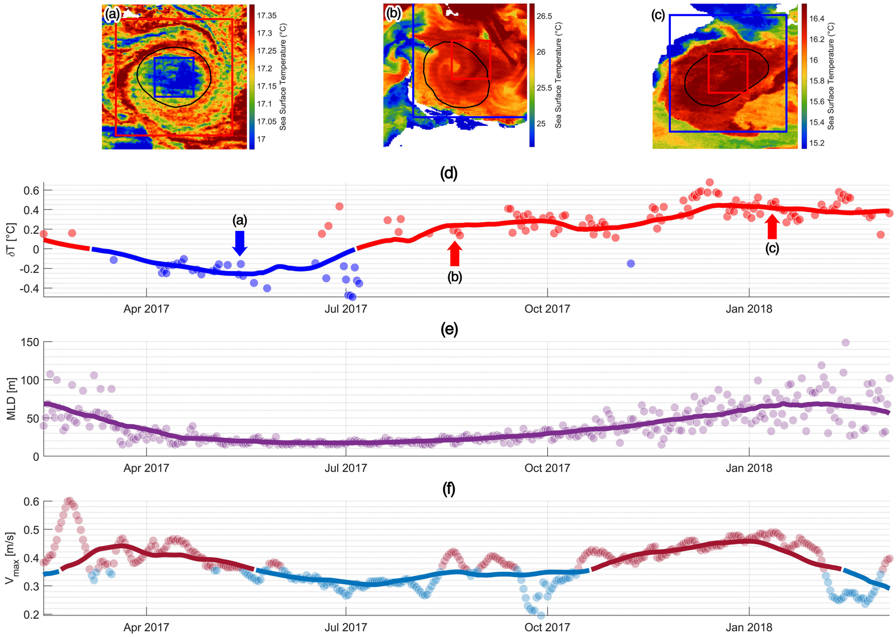

Figure I.12: **Timeline of the Algeria Anticyclone** with DYNED ID #11411. Panels (a)-(c) show four characteristic SST patches corresponding with the δT evolution in panel (d). Panel (e) shows the evolution of the MLD outside the eddy. Panel (f) shows the evolution of the maximal velocity. Lines represent the MMA of each variable. For more information the reader is refered to Figure I.8.

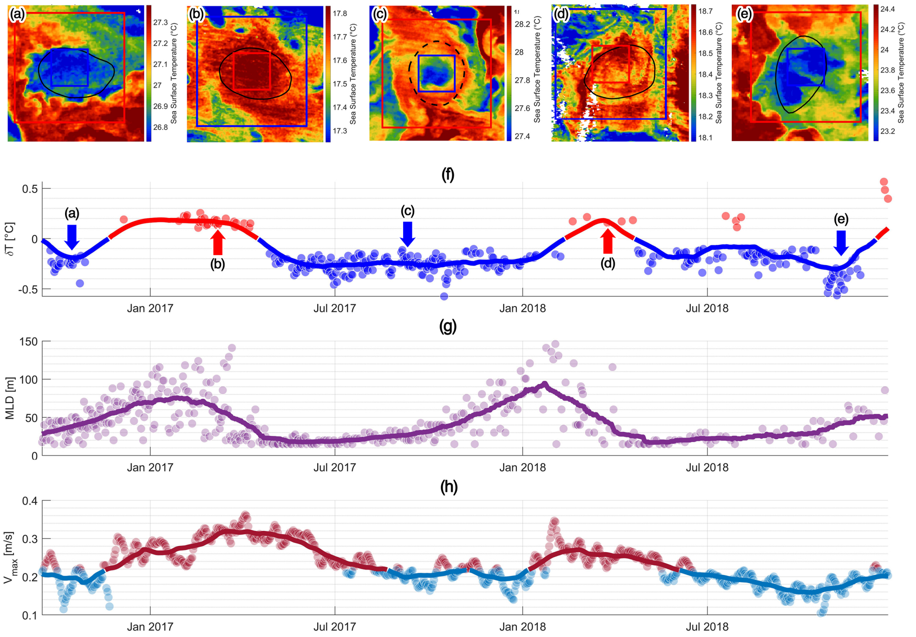

Figure I.13: **Timeline of the Cyprus (Eratosthenes) Anticyclone** with DYNED ID #10754. Panels (a)-(e) show four characteristic SST patches corresponding with the δT evolution in panel (f). Panel (g) shows the evolution of the MLD outside the eddy. Panel (h) shows the evolution of the maximal velocity. Lines represent the MMA of each variable. For more information the reader is refered to Figure I.8.

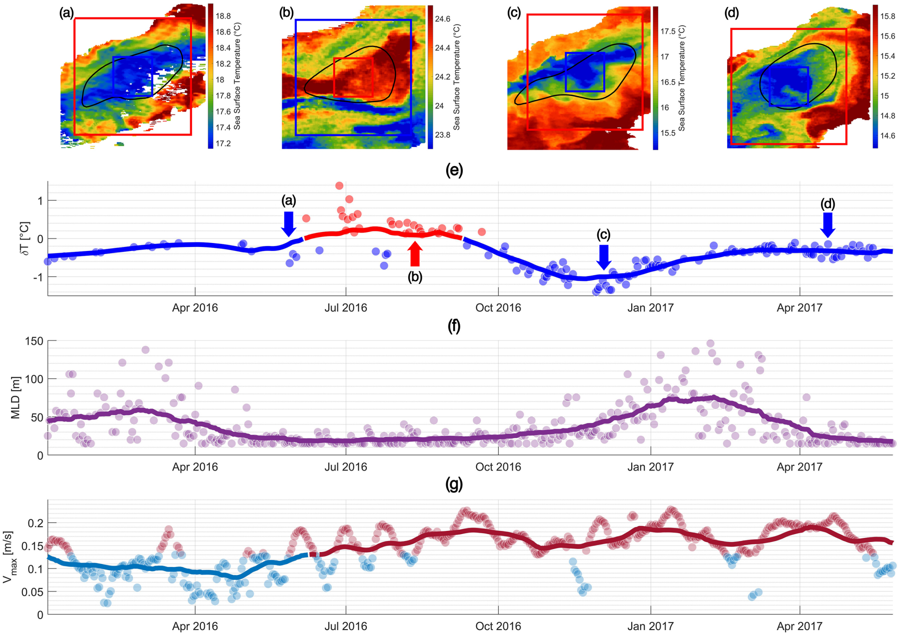

Figure I.14: **Timeline of the Liguria Cyclone** with DYNED ID #9784. Panels (a)-(d) show four characteristic SST patches corresponding with the δT evolution in panel (e). Panel (f) shows the evolution of the MLD outside the eddy. Panel (g) shows the evolution of the maximal velocity. Lines represent the MMA of each variable. For more information the reader is refered to Figure I.8.

References

Abrahms, B. et al. (2018). “Mesoscale activity facilitates energy gain in a top predator”. In: *Proceedings of the Royal Society B* vol. 285, no. 1885, p. 20181101.

Amitai, Y. et al. (2010). “Surface circulation of the eastern Mediterranean Levantine basin: Insights from analyzing 14 years of satellite altimetry data”. In: *Journal of Geophysical Research: Oceans* vol. 115, no. C10.

Amores, A. et al. (2018). “Up to what extent can we characterize ocean eddies using present-day gridded altimetric products?” In: *Journal of Geophysical Research: Oceans* vol. 123, no. 10, pp. 7220–7236.

Assassi, C. et al. (2016). “An index to distinguish surface-and subsurface-intensified vortices from surface observations”. In: *Journal of Physical Oceanography* vol. 46, no. 8, pp. 2529–2552.

Auer, S. J. (1987). “Five-year climatological survey of the Gulf Stream system and its associated rings”. In: *Journal of Geophysical Research: Oceans* vol. 92, no. C11, pp. 11709–11726.

Barboni, A. et al. (2021). “Lagrangian eddy tracking reveals the Eratosthenes anticyclonic attractor in the eastern Levantine basin”. In: *Ocean Science Discussions*, pp. 1–35.

Baudena, A. et al. (2021). “Fine-scale structures as spots of increased fish concentration in the open ocean”. In: *Scientific Reports* vol. 11, no. 1, pp. 1–13.

Boyer Montégut, C. de et al. (2004). “Mixed layer depth over the global ocean: An examination of profile data and a profile-based climatology”. In: *Journal of Geophysical Research: Oceans* vol. 109, no. C12.

Brach, L. et al. (2018). “Anticyclonic eddies increase accumulation of microplastic in the North Atlantic subtropical gyre”. In: *Marine pollution bulletin* vol. 126, pp. 191–196.

Chelton, D. B., Schlax, M. G., and Samelson, R. M. (2011). “Global observations of nonlinear mesoscale eddies”. In: *Progress in oceanography* vol. 91, no. 2, pp. 167–216.

Danioux, E., Vanneste, J., and Bühler, O. (2015). “On the concentration of near-inertial waves in anticyclones”. In: *Journal of Fluid Mechanics* vol. 773.

Elipot, S., Lumpkin, R., and Prieto, G. (2010). “Modification of inertial oscillations by the mesoscale eddy field”. In: *Journal of Geophysical Research: Oceans* vol. 115, no. C9.

Escudier, R. et al. (2016). “Eddy properties in the Western Mediterranean Sea from satellite altimetry and a numerical simulation”. In: *Journal of Geophysical Research: Oceans* vol. 121, no. 6, pp. 3990–4006.

Everett, J. et al. (2012). “An avenue of eddies: Quantifying the biophysical properties of mesoscale eddies in the Tasman Sea”. In: *Geophysical Research Letters* vol. 39, no. 16.

Frenger, I. et al. (2013). “Imprint of Southern Ocean eddies on winds, clouds and rainfall”. In: *Nature geoscience* vol. 6, no. 8, pp. 608–612.

Gaube, P., J. McGillicuddy Jr, D., and Moulin, A. J. (2019). “Mesoscale eddies modulate mixed layer depth globally”. In: *Geophysical Research Letters* vol. 46, no. 3, pp. 1505–1512.

Gaube, P. et al. (2013). “Satellite observations of chlorophyll, phytoplankton biomass, and Ekman pumping in nonlinear mesoscale eddies”. In: *Journal of Geophysical Research: Oceans* vol. 118, no. 12, pp. 6349–6370.

Gaube, P. et al. (2015). “Satellite observations of mesoscale eddy-induced Ekman pumping”. In: *Journal of Physical Oceanography* vol. 45, no. 1, pp. 104–132.

Gómez, G. S. D., Nagai, T., and Yokawa, K. (2020). “Mesoscale warm-core eddies drive interannual modulations of swordfish catch in the Kuroshio Extension System”. In: *Frontiers in Marine Science.*

Hamad, N., Millot, C., and Taupier-Letage, I. (2006). “The surface circulation in the eastern basin of the Mediterranean Sea”. In: *Scientia Marina* vol. 70, no. 3, pp. 457–503.

Hausmann, U. and Czaja, A. (2012). “The observed signature of mesoscale eddies in sea surface temperature and the associated heat transport”. In: *Deep Sea Research Part I: Oceanographic Research Papers* vol. 70, pp. 60–72.

Ioannou, A. et al. (2017). “Dynamical evolution of intense Ierapetra eddies on a 22 year long period”. In: *Journal of Geophysical Research: Oceans* vol. 122, no. 11, pp. 9276–9298.

Ioannou, A. et al. (2019). “Cyclostrophic corrections of AVISO/DUACS surface velocities and its application to mesoscale eddies in the Mediterranean Sea”. In: *Journal of Geophysical Research: Oceans* vol. 124, no. 12, pp. 8913–8932.

Klein, P. and Lapeyre, G. (2009). “The oceanic vertical pump induced by mesoscale and submesoscale turbulence”. In: *Annual review of marine science* vol. 1, pp. 351–375.

Klein, P. and Smith, S. L. (2001). “Horizontal dispersion of near-inertial oscillations in a turbulent mesoscale eddy field”. In: *Journal of marine research* vol. 59, no. 5, pp. 697–723.

Kunze, E. (1985). “Near-inertial wave propagation in geostrophic shear”. In: *Journal of Physical Oceanography* vol. 15, no. 5, pp. 544–565.

Laxenaire, R. et al. (2018). “Anticyclonic eddies connecting the western boundaries of Indian and Atlantic Oceans”. In: *Journal of Geophysical Research: Oceans* vol. 123, no. 11, pp. 7651–7677.

Le Vu, B., Stegner, A., and Arsouze, T. (2018). “Angular Momentum Eddy Detection and tracking Algorithm (AMEDA) and its application to coastal eddy formation”. In: *Journal of Atmospheric and Oceanic Technology* vol. 35, no. 4, pp. 739–762.

Ledwell, J. R., McGillicuddy Jr, D. J., and Anderson, L. A. (2008). “Nutrient flux into an intense deep chlorophyll layer in a mode-water eddy”. In: *Deep Sea Research Part II: Topical Studies in Oceanography* vol. 55, no. 10-13, pp. 1139–1160.

Lelong, M.-P., Cuypers, Y., and Bouruet-Aubertot, P. (2020). “Near-inertial energy propagation inside a Mediterranean anticyclonic eddy”. In: *Journal of Physical Oceanography* vol. 50, no. 8, pp. 2271–2288.

Lévy, M., Franks, P. J., and Smith, K. S. (2018). “The role of submesoscale currents in structuring marine ecosystems”. In: *Nature communications* vol. 9, no. 1, pp. 1–16.

Leyba, I. M., Saraceno, M., and Solman, S. A. (2017). “Air-sea heat fluxes associated to mesoscale eddies in the Southwestern Atlantic Ocean and their dependence on different regional conditions”. In: *Climate Dynamics* vol. 49, no. 7-8, pp. 2491–2501.

Liu, Y., Yu, L., and Chen, G. (2020). “Characterization of Sea Surface Temperature and Air-Sea Heat Flux Anomalies Associated With Mesoscale Eddies in the South China Sea”. In: *Journal of Geophysical Research: Oceans* vol. 125, no. 4, e2019JC015470.

Martinez-Marrero, A. et al. (2019). “Near-inertial wave trapping near the base of an anticyclonic mesoscale eddy under normal atmospheric conditions”. In: *Journal of Geophysical Research: Oceans* vol. 124, no. 11, pp. 8455–8467.

McGillicuddy Jr, D. J. (2016). “Mechanisms of physical-biological-biogeochemical interaction at the oceanic mesoscale”. In: *Annual Review of Marine Science* vol. 8, pp. 125–159.

Menna, M. et al. (2012). “On the surface circulation of the Levantine sub-basin derived from Lagrangian drifters and satellite altimetry data”. In: *Deep Sea Research Part I: Oceanographic Research Papers* vol. 65, pp. 46–58.

Millot, C. (1985). “Some features of the Algerian Current”. In: *Journal of Geophysical Research: Oceans* vol. 90, no. C4, pp. 7169–7176.

Mkhinini, N. et al. (2014). “Long-lived mesoscale eddies in the eastern Mediterranean Sea: Analysis of 20 years of AVISO geostrophic velocities”. In: *Journal of Geophysical Research: Oceans* vol. 119, no. 12, pp. 8603–8626.

Moschos, E. et al. (2020a). “Classification of eddy sea surface temperature signatures under cloud coverage”. In: *IEEE Journal of Selected Topics in Applied Earth Observations and Remote Sensing* vol. 13, pp. 3437–3447.

Moschos, E. et al. (2020b). “DEEP-SST-EDDIES: A Deep Learning framework to detect oceanic eddies in Sea Surface Temperature images”. In: *ICASSP 2020-2020 IEEE International Conference on Acoustics, Speech and Signal Processing (ICASSP)*. IEEE, pp. 4307–4311.

Moutin, T. and Prieur, L. (2012). “Influence of anticyclonic eddies on the Biogeochemistry from the Oligotrophic to the Ultraoligotrophic Mediterranean (BOUM cruise)”. In: *Biogeosciences* vol. 9, no. 10, pp. 3827–3855.

Nardelli, B. B. et al. (2013). “High and Ultra-High resolution processing of satellite Sea Surface Temperature data over Southern European Seas in the framework of MyOcean project”. In: *Remote Sensing of Environment* vol. 129, pp. 1–16.

Ni, Q. et al. (2021). “Abundant cold anticyclonic eddies and warm cyclonic eddies in the global ocean”. In: *Journal of Physical Oceanography* vol. 51, no. 9, pp. 2793–2806.

Pessini, F. et al. (2018). “Mesoscale eddies in the Algerian Basin: do they differ as a function of their formation site?” In: *Ocean Science* vol. 14, no. 4.

Pettenuzzo, D., Large, W., and Pinardi, N. (2010). “On the corrections of ERA-40 surface flux products consistent with the Mediterranean heat and water budgets and the connection between basin surface total heat flux and NAO". In: *Journal of Geophysical Research: Oceans* vol. 115, no. C6.

Stegner, A. et al. (2021). "Cyclone-Anticyclone Asymmetry of Eddy Detection on Gridded Altimetry Product in the Mediterranean Sea". In: *Journal of Geophysical Research: Oceans* vol. 126, no. 9, e2021JC017475.

Su, Z. et al. (2018). "Ocean submesoscales as a key component of the global heat budget". In: *Nature communications* vol. 9, no. 1, pp. 1–8.

Sun, W. et al. (2019). "Statistical Characteristics of Cyclonic Warm-Core Eddies and Anticyclonic Cold-Core Eddies in the North Pacific Based on Remote Sensing Data". In: *Remote Sensing* vol. 11, no. 2, p. 208.

Trott, C. B. et al. (2019). "Eddy-induced temperature and salinity variability in the Arabian Sea". In: *Geophysical Research Letters* vol. 46, no. 5, pp. 2734–2742.

Whalen, C. B., MacKinnon, J. A., and Talley, L. D. (2018). "Large-scale impacts of the mesoscale environment on mixing from wind-driven internal waves". In: *Nature Geoscience* vol. 11, no. 11, pp. 842–847.

Young, W. and Jelloul, M. B. (1997). "Propagation of near-inertial oscillations through a geostrophic flow". In: *Journal of marine research* vol. 55, no. 4, pp. 735–766.

Zhang, Z., Wang, W., and Qiu, B. (2014). "Oceanic mass transport by mesoscale eddies". In: *Science* vol. 345, no. 6194, pp. 322–324.

Paper II

DEEP-SST-EDDIES: A Deep Learning framework to detect oceanic eddies in Sea Surface Temperature Images

Evangelos Moschos, Olivier Schwander, Alexandre Stegner, Patrick Gallinari

Published in *ICASSP 2020 IEEE International Conference on Acoustics, Speech and Signal Processing*, May 2020, pp. 4307–4311. DOI: 10.1109/ICASSP40776.2020.9053909..

Abstract

Until now, mesoscale oceanic eddies have been automatically detected through physical methods on satellite altimetry. Nevertheless, they often have a visible signature on Sea Surface Temperature (SST) satellite images, which have not been yet sufficiently exploited. We introduce a novel method that employs Deep Learning to detect eddy signatures on such input. We provide the first available dataset for this task, retaining SST images through altimetric-based region proposal. We train a CNN-based classifier which succeeds in accurately detecting eddy signatures in well-defined examples. Our experiments show that the difficulty of classifying a large set of automatically retained images can be tackled by training on a smaller subset of manually labeled data. The difference in performance on the two sets is explained by the noisy automatic labeling and intrinsic complexity of the SST signal. This approach can provide to oceanographers a tool for validation of altimetric eddy detection through SST.

II.1 Introduction

Mesoscale eddies are oceanic vortices with horizontal scales on the order of few tens of kilometers and lifetime on the order of weeks or months. These large, coherent structures can trap and transport heat, salt, pollutants and various biogeochemical components from their regions of formation to remote areas (Z. Zhang et al., 2014). Their dynamics can impact significantly the biological productivity at the ocean surface (Gaube et al., 2013; McGillicuddy

Jr, 2016), modify the mixed layer (Kouketsu et al., 2011), amplify locally the vertical motions (Klein et al., 2009) and even concentrate and transport microplastics (Brach et al., 2018). Thanks to spectacular advances in satellite altimetry, automatic eddy detection and tracking algorithms have become essential analytical tools for studying the dynamics of oceanic eddies.

Plenty of these algorithms, based on multi-satellite altimetry maps, have been developed during the last ten years (Chelton et al., 2011; Le Vu et al., 2018; Nencioli et al., 2010). These algorithms use geometrical properties of the Sea Surface Height (SSH) field and/or the streamlines of the derived velocity field to detect and track in time vortex structures. However, altimetry satellite products undergo large spatio-temporal interpolation between the areas crossed by satellite tracks, producing low-resolution fields as well as uncertainty in areas which have not been adequately sampled. Recent studies show that many oceanic eddies could be missed or wrongly detected (Amores et al., 2018).

On the other hand, eddy signatures are also apparent in visible satellite imagery such as Sea Surface Temperature (SST), Ocean Color/Chlorophyll (CHL), or synthetic-aperture radar (SAR images). Even if visible imagery has much higher resolution than altimetry, it may be frequently covered by clouds and the few detection algorithms that have been developed on SST (D'Alimonte, 2009; Dong et al., 2011) hardly exploit their complex patterns. Deep Learning has been rapidly gaining in popularity and solving problems in remote sensing (L. Zhang et al., 2016), climate and the environment (Rolnick et al., 2019). Machine learning methods have also been used in previous studies to tackle altimetric eddy detection and tracking on the SSH field via pixel-wise classification (Lguensat et al., 2018) or LSTM (Franz et al., 2018), as well as the velocity field (Ashkezari et al., 2016). Albeit their important contributions, they are restricted the limitations of the altimetry field $per se$ (that is, its interpolation) on which the learning dataset is based. Deep learning has also been reportedly employed for classification of eddy signatures in SAR images (Huang et al., 2017).

In this study we seek to harness the potential of deep learning on the visible satellite imagery of Sea Surface Temperature, which contains high-resolution vortex signatures. To this purpose, we introduce a novel method to obtain a dataset of SST images based on altimetric detection. The SST dataset is available on demand through https://www1.lmd.polytechnique.fr/dyned/data-base.We train a CNN-based classifier which is able to accurately detect eddy signatures on well-defined, manually selected cases. The classifier is tested on a larger set containing noisy labels and shows potential in selecting the accurately labeled images and correcting false labels. This methodology could serve to validate altimetric eddy detection through SST.

II.2 SST Eddy Image Dataset

II.2.1 Localizing SST images through altimetric detections

The task of this study consists in classifying SST images which can contain either the signature of an Anticyclonic Eddy (AE), a Cyclonic Eddy (CE) or

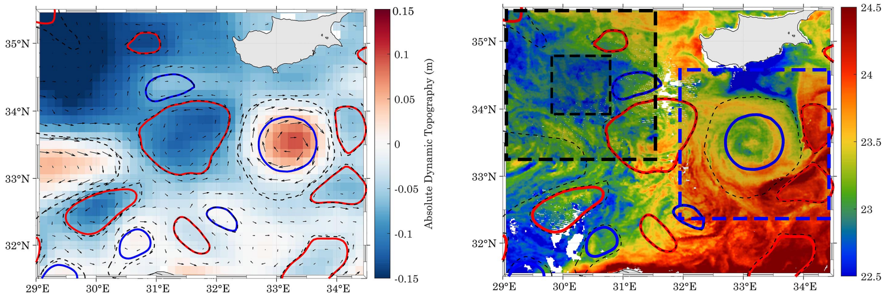

Figure II.1: Altimetric field with superimposed geostrophic velocity vectors (left) and SST field (right) in the Levantine Sea on the 08/06/2017. Maximum velocity contours detected by AMEDA on altimetry are superimposed on both figures. On the rightmost one, the blue box represents a sample AE AoI, the big black box represents a sample NE AoI, and the smaller black box inside it shows the area of no-contour constrain.

No Eddy signature (NE). Anticyclones (cyclones) rotate in the opposite (same) direction with the earth's rotation, that is clockwise (counter-clockwise) in the Northern Hemisphere.

To create a data-set of SST images, the Mediterranean Sea is chosen as the domain of study, where through the CMEMS we receive 720 daily high-resolution images for the period of 2016-2017. These images, produced as desribed in Nardelli et al., 2013, consist of of supercollated SST data with a resolution of 1/12° and are representative of night SST values.

To localize and retain Areas of Interest (AoI) containing AE and CE signatures on the SST field, we utilize the daily outputs of the Angular Momentum Eddy Detection and tracking Algorithm ($AMEDA$) (Le Vu et al., 2018), working on satellite altimetry and applied on the AVISO/DUACS field of geostrophic velocities. The AMEDA detects eddies by identifying minima and maxima on the geostrophic velocity field and selecting closed streamlines around them. The algorithm does also dynamically track eddies backward and forward in time, as well as identifies their merging and splitting events. Eddy tracks detected by AMEDA, labeled as AE or CE based on their sense of rotation, with information on the closed contour of maximum velocity and other properties, are contained in the DYNED-Atlas [1]

For each day of the two-year period of study, we co-localize the AE and CE contours received from AMEDA with the SST images both referring to the domain of the Med Sea. In this sense, physical detections on altimetry act as a region proposal for class-representative SST image extraction. Around each AMEDA contour we crop a AoI with side $k = \lambda * R_{max}$ where R_{max} is the

---

[1] The DYNED-Atlas, containing more than 11500 eddy tracks for the 2000-2017 period in the Mediterranean Sea, is publicly available through: https://www1.lmd.polytechnique.fr/dyned/data-base

radius of a circle of equivalent area with the AMEDA maximum velocity contour, and $\lambda = 5$. These AoI are interpolated to a constant size of $m = \lambda * \bar{R}_{max}(km)$ where $\bar{R}_{max} = 42.5km$ is the mean maximum velocity radius of all AMEDA contours retained, resulting in an image size of $m = 230$ pixels. In order to receive SST images labeled as NE, that is, not containing an eddy signature, an AoI of size $m = 230$ pixels is slided along the domain of the Mediterranean Sea. AoI that do not contain any AMEDA contour in their center (in a smaller box of side R_{max}) are retained as NE images. The above methodology is visualized in Figure II.1.

All the retained images are also furtherly filtered based on the altimetric satellite track coverage of the AoI and the cloud coverage of the SST image. Thus SST images corresponding to altimetric detections with the lowest uncertainty are selected. A threshold of 50% is selected as the maximum missing values due to clouds for an image to be retained.

II.2.2 Dataset features and labels

We automatically retain a dataset of SST images with 4000 images for each of the AE,CE and NE classes (total of 12000 images). These are one-channel images with values that represent the grid temperature in degrees Celsius.

Examples of images contained in the Dataset are given in Figure II.2. They are distincted based on whether they contain an eddy signature (AE, CE) or not (NE). Apart from their sense of rotation, eddy signature images can also be visually characterized by the sign of their core anomaly: both warm and cold core cases exist for the two classes AE and CE.

In order to enhance feature extraction and generalization, two methods are followed: The first consists of applying rotational augmentation during the training process. This way, rotational invariance, on images which depict physically rotating structures, can be learned. The second concerns cloud coverage: all cloud cover pixels are set to zero value. An extra channel of a semantic mask is added to each image, where all non cloud points are set to a value of one.

Noisy labels are contained in the Dataset: images selected through AMEDA contours and labeled as AE or CE might not contain eddy signature or, *mutatis mutandis*, images labeled as NE might contain the signature of an eddy missed by AMEDA. Mislabeling by AMEDA can be due to intrinsic limits of the altimetric dataset or algorithm errors. Cloud coverage and air-sea processes can also affect significantly the surface eddy signature. Through visual sampling of the automatically received, noisy labeled, Dataset, we diagnose a 20% of images being accurately labeled and a 80% containing false or uncertain labels. Because of this effect we manually separate 1,200 images (400 per class) creating a of handpicked, accurate labeled (here on $EDDIES - HL$) and class-representative examples. From the total Dataset we remove the images contained in the EDDIES-HL dataset to receive a large dataset of 10,8000 images containing noisy labels (here on $EDDIES - AUTO$).

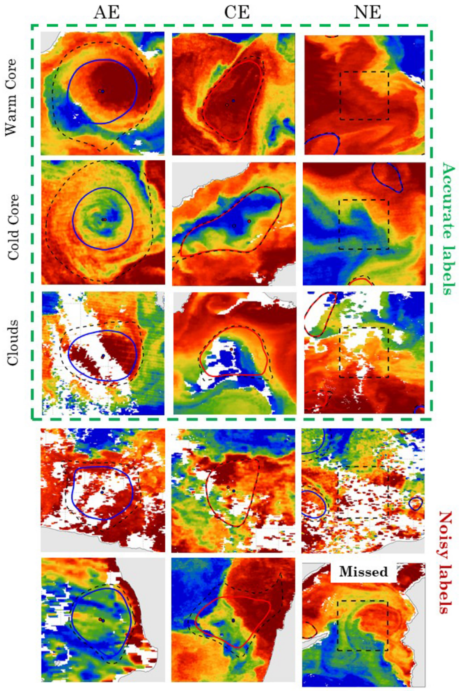

Figure II.2: Samples of SST images, plotted together with the AMEDA contours. Columns represent the three classes. Dashed line boxes on NE images represent the areas of no-contour constrain. Examples with both accurate and noisy labels are given. Colours represent one channel images in a perceptually uniform jet colormap between the 5th and the 95th percentile of the image range of temperature values. Clouds are visualized with white colour and land with a gray patch.

II.3 Training a CNN-Based Classifier

Convolutional Neural Networks have been exceptionally successful in practical applications which consist of processing complex imagery, as is the case of the satellite data used here. A CNN-based classifier is employed to treat the 3-class problem, using a Cross-Entropy Loss, Stochastic Gradient Descent with momentum and a SoftMax output. Residual Networks (He et al., 2016) use skip connections between layers in order to build efficient Deep Architectures. A pretrained ResNet18 architecture is used in this study, downloaded through the torchvision package of the Pytorch library. All 18 layers are finetuned during the training process.

Apart from the test set, a validation set (consisting of 10% of the train set) is used in our experiments. This allows early stopping based on loss function convergence to a local minimum with a certain patience, in order to avoid

Setup	Test Accuracy
EDDIES-HL	92.9 ± 1.3 %
EDDIES-HL (+Mask)	93.8 ± 1.1 %
EDDIES-HL (+Rotation)	94.7 ± 1.0
EDDIES-HL (+Mask+Rot)	95.6 ± 0.5 %

Table II.1: Test accuracy for different setups on the EDDIES-HL dataset training. Reported scores are means ± stdev, of the 5-fold cross validation.

overfitting.

II.4 Results and Discussion

A 5-fold stratified cross validation is performed through a 80/20 train/test split on the EDDIES-HL dataset. For four different setups, the mean and standard deviation of the accuracy on the test set, is shown on Table II.1. The positive effect of adding a semantic mask and a rotation is seen through the increase in mean accuracy and decrease in divergence of models trained on different folds.

For a more in depth view of model performance, the normalized confusion matrix on the EDDIES-HL set (using both the semantic mask and rotational augmentation techniques) is plotted in Figure II.3(a). An overall accuracy of 95.6% is achieved, with a good convergence between different folds ($\sigma = 0.5\%$). The high precision on the AE denotes the prevalence of clear signatures in anticyclonic images. Also the zero missprediction between AE and CE classes depicts the ability of our model to clearly separate between eddy signature classes. The model shows small error in discriminating CE images from NE. This can be explained by the fact that cyclonic signatures are in general weaker on SST than anticyclonic ones.

The performance of the models trained on the EDDIES-HL dataset is then evaluated on the EDDIES-AUTO dataset. The results of the confusion matrix in Figure II.3(b) shows the difference between the label predicted by the model and the (noisy) label of this dataset. The drop in accuracy here, is caused by the false labels as well as the larger variance of features (increased cloud coverage and unclear signatures) of the images contained in EDDIES-AUTO. Nevertheless, the model is still able to separate clearly the AE from CE signatures.

In Figure II.3(c) some characteristic examples of the above matrix are visualized, illustrating the ability of the model to predict physically accurate labels on noisy labeled images. Samples outside of the diagonal are examples of false label corrections. The confidence of the model is also evaluated by visually inspecting 400 correctly predicted images per class, above a score threshold of $t = 0.90$. Of them 90% of AE, 70% of CE and 95% of NE have a visual signal corresponding to their predicted label. The model trained on the well-defined samples shows therefore robust performance in selecting the accurately labeled AE and NE images among the noisy labeled ones, which could be used to

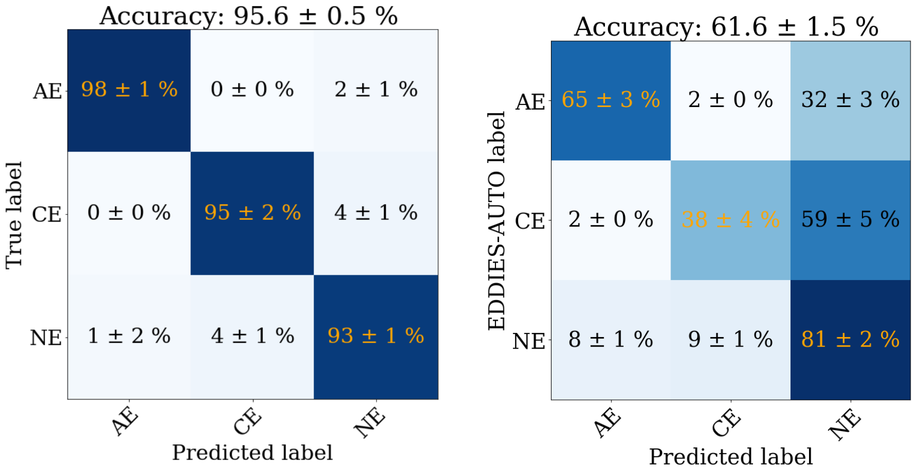

(a) Confusion: EDDIES-HL (b) Confusion EDDIES-AUTO

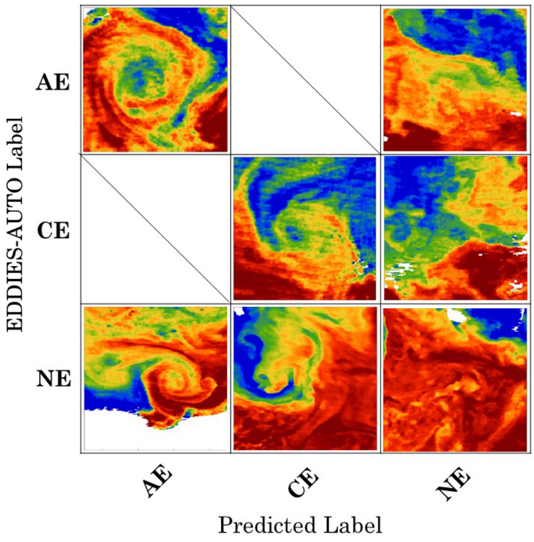

(c) Samples from EDDIES-AUTO confusion matrix

Figure II.3: (a-b): Normalized Confusion Matrices of the model trained with a 5-fold cross validation on the EDDIES-HL dataset and tested on the two different datasets. (c): Characteristic samples corresponding to cells of the matrix in (b).

further enlarge the EDDIES-HL dataset in a semi-supervised learning fashion. Performance is less reliable for the *CE* class, depicting that the signature of cyclones on *SST* is more complex and difficult to distinguish.

II.5 Conclusion and Perspectives

In this study classification of mesoscale oceanic eddy signatures in Sea Surface Temperature Images is introduced. A methodology is presented to automatically obtain a dataset of SST images, using region proposal provided by physical detections on the altimetric field. An accuracy of 95.6 ± 0.5 is performed on a manually selected dataset of 1200 images with accurate labels (EDDIES-HL), by finetuning a pretrained ResNet18. The same network is tested on a larger dataset with noisy labels (EDDIES-AUTO) in order to evaluate its ability to select among them those accurately labeled, and correct false labels. Our CNN-based classifier shows robust performance in detecting Anticyclonic Eddy signatures in images and a less reliable one in detecting Cyclonic Eddy signatures.

In future work, methods used for treating and correcting noisy labels (Mnih et al., 2012; Northcutt et al., 2019; Sukhbaatar et al., 2014) can be utilized to self-learn on a large dataset of noisy-labeled images guided through a dataset of accurate labeled ones. Ultimately, object detection and tracking methods such as the ones described in Bertinetto et al., 2016; Ren et al., 2015 could be applied on multi-modal images containing eddy signatures, harnessing the power of deep learning to surpass the limits of altimetric eddy detection.

References

Amores, A. et al. (2018). “Up to what extent can we characterize ocean eddies using present-day gridded altimetric products?” In: *Journal of Geophysical Research: Oceans* vol. 123, no. 10, pp. 7220–7236.

Ashkezari, M. D. et al. (2016). “Oceanic eddy detection and lifetime forecast using machine learning methods”. In: *Geophysical Research Letters* vol. 43, no. 23, pp. 12–234.

Bertinetto, L. et al. (2016). “Fully-convolutional siamese networks for object tracking”. In: *European conference on computer vision.* Springer, pp. 850–865.

Brach, L. et al. (2018). “Anticyclonic eddies increase accumulation of microplastic in the North Atlantic subtropical gyre”. In: *Marine pollution bulletin* vol. 126, pp. 191–196.

Chelton, D. B., Schlax, M. G., and Samelson, R. M. (2011). “Global observations of nonlinear mesoscale eddies”. In: *Progress in oceanography* vol. 91, no. 2, pp. 167–216.

D’Alimonte, D. (2009). “Detection of mesoscale eddy-related structures through iso-SST patterns”. In: *IEEE Geoscience and Remote Sensing Letters* vol. 6, no. 2, pp. 189–193.

Dong, C. et al. (2011). “An automated approach to detect oceanic eddies from satellite remotely sensed sea surface temperature data”. In: *IEEE Geoscience and Remote Sensing Letters* vol. 8, no. 6, pp. 1055–1059.

Franz, K. et al. (2018). “Ocean eddy identification and tracking using neural networks”. In: *IGARSS 2018-2018 IEEE International Geoscience and Remote Sensing Symposium.* IEEE, pp. 6887–6890.

Gaube, P. et al. (2013). “Satellite observations of chlorophyll, phytoplankton biomass, and Ekman pumping in nonlinear mesoscale eddies”. In: *Journal of Geophysical Research: Oceans* vol. 118, no. 12, pp. 6349–6370.

He, K. et al. (2016). “Deep residual learning for image recognition”. In: *Proceedings of the IEEE conference on computer vision and pattern recognition*, pp. 770–778.

Huang, D. et al. (2017). “Deepeddy: A simple deep architecture for mesoscale oceanic eddy detection in sar images”. In: *2017 IEEE 14th International Conference on Networking, Sensing and Control (ICNSC).* IEEE, pp. 673–678.

Klein, P. and Lapeyre, G. (2009). “The oceanic vertical pump induced by mesoscale and submesoscale turbulence”. In: *Annual review of marine science* vol. 1, pp. 351–375.

Kouketsu, S. et al. (2011). “The role of meso-scale eddies in mixed layer deepening and mode water formation in the western North Pacific”. In: *New Developments in Mode-Water Research.* Springer, pp. 59–73.

Le Vu, B., Stegner, A., and Arsouze, T. (2018). “Angular Momentum Eddy Detection and tracking Algorithm (AMEDA) and its application to coastal eddy formation”. In: *Journal of Atmospheric and Oceanic Technology* vol. 35, no. 4, pp. 739–762.

Lguensat, R. et al. (2018). "EddyNet: A deep neural network for pixel-wise classification of oceanic eddies". In: *IGARSS 2018-2018 IEEE International Geoscience and Remote Sensing Symposium.* IEEE, pp. 1764–1767.

McGillicuddy Jr, D. J. (2016). "Mechanisms of physical-biological-biogeochemical interaction at the oceanic mesoscale". In: *Annual Review of Marine Science* vol. 8, pp. 125–159.

Mnih, V. and Hinton, G. E. (2012). "Learning to label aerial images from noisy data". In: *Proceedings of the 29th International conference on machine learning (ICML-12)*, pp. 567–574.

Nardelli, B. B. et al. (2013). "High and Ultra-High resolution processing of satellite Sea Surface Temperature data over Southern European Seas in the framework of MyOcean project". In: *Remote Sensing of Environment* vol. 129, pp. 1–16.

Nencioli, F. et al. (2010). "A vector geometry–based eddy detection algorithm and its application to a high-resolution numerical model product and high-frequency radar surface velocities in the Southern California Bight". In: *Journal of atmospheric and oceanic technology* vol. 27, no. 3, pp. 564–579.

Northcutt, C. G., Jiang, L., and Chuang, I. L. (2019). "Confident Learning: Estimating Uncertainty in Dataset Labels". In: *arXiv preprint arXiv:1911.00068.*

Ren, S. et al. (2015). "Faster r-cnn: Towards real-time object detection with region proposal networks". In: *Advances in neural information processing systems*, pp. 91–99.

Rolnick, D. et al. (2019). "Tackling Climate Change with Machine Learning". In: *arXiv preprint arXiv:1906.05433.*

Sukhbaatar, S. et al. (2014). "Training convolutional networks with noisy labels". In: *arXiv preprint arXiv:1406.2080.*

Zhang, L., Zhang, L., and Du, B. (2016). "Deep learning for remote sensing data: A technical tutorial on the state of the art". In: *IEEE Geoscience and Remote Sensing Magazine* vol. 4, no. 2, pp. 22–40.

Zhang, Z., Wang, W., and Qiu, B. (2014). "Oceanic mass transport by mesoscale eddies". In: *Science* vol. 345, no. 6194, pp. 322–324.

Paper III

Classification of Eddy Sea Surface Temperature Signatures Under Cloud Coverage

Evangelos Moschos, Alexandre Stegner, Olivier Schwander, Patrick Gallinari

Published in *IEEE Journal of Selected Topics in Applied Earth Observations and Remote Sensing*, June 2020, vol. 13, pp. 3437-3447. DOI: 10.1109/JSTARS.2020.3001830..

Abstract

Mesoscale oceanic eddies have a visible signature on Sea Surface Temperature (SST) satellite images, portraying diverse patterns of coherent vortices, temperature gradients and swirling filaments. However, learning the regularities of such signatures defines a challenging pattern recognition task, due to their complex structure but also to the cloud coverage which can corrupt a large fraction of the image. We introduce a novel Deep Learning approach to classify sea temperature eddy signatures, even if they are corrupted by strong cloud coverage. A large dataset of SST image patches is automatically retained and used to train a CNN-based classifier. Classification is performed with very high accuracy on coherent eddy signatures and is robust to a high level of cloud coverage, surpassing human expert efficiency on this task. This methodology can serve to validate and correct detections on satellite altimetry, the standard method used until now to track mesoscale eddies.

III.1 Introduction

III.1.1 The prominence of mesoscale eddies

Mesoscale eddies are oceanic vortices with a typical radius of the order of 20-80 kilometres which is equal or larger than the local Rossby deformation radius. They can be long-lived, with lifetimes of several months or even years. Significant advances in the resolution of both satellite altimetry measurements (Chelton et al., 2011) and high resolution oceanic numerical models (Su et al., 2018) have revealed the predominance of eddies in the global oceanic circulation. These large, coherent structures can trap and transport heat, salt, pollutants and various biogeochemical components from their regions of formation to remote areas (Z. Zhang et al., 2014). Their dynamics can impact significantly the biological productivity at the ocean surface (Gaube et al., 2013; McGillicuddy Jr, 2016), influence clouds and rainfall within their vicinity (Frenger et al., 2013), modify the mixed layer (Kouketsu et al., 2011), amplify locally the vertical motions (Klein et al., 2009) and even concentrate and transport microplastics (Brach et al., 2018). Eddies have been demonstrated to play a prominent role in regional circulation in various areas such as the Southern Ocean (Mazloff et al., 2010), the Sargasso Sea (McGillicuddy et al., 1998), the Indo-Atlantic exchange (Laxenaire et al., 2019) or the Mediterranean Sea (Escudier et al., 2016; Ioannou et al., 2017; Mkhinini et al., 2014). We focus on the latter in this study.

III.1.2 Altimetric-based eddy detection and tracking algorithms

In order to detect and follow the trajectories of a very large number of mesoscale eddies on multi-satellite altimetry maps, several automatic eddy detection and tracking algorithms have been developed during the last ten years: The Okubo-Weiss parameter (Okubo, 1970; Weiss, 1991), which quantifies the relative importance of rotation with respect to deformation, is used in many studies to detect and track eddies on the geostrophic surface velocities field (Chaigneau et al., 2008; Chelton et al., 2007; Isern-Fontanet et al., 2003). Geometric properties of the streamlines have been used by other methods (Nencioli et al., 2010; Sadarjoen et al., 2000) to identify coherent vortices without considering their intensity. Finally, a physical parameter, the local normalized angular momentum, introduced by Mkhinini et al., 2014 and Le Vu et al., 2018, combines both the dynamical and the geometrical properties of the signature of mesoscale eddies on altimetric-based products. In this study, we follow this approach and use the Angular Momentum Eddy Detection and Tracking Algorithm (AMEDA) (Le Vu et al., 2018) which has shown to be very effective in locating mesoscale eddies in the Mediterranean Sea (Garreau et al., 2018; Ioannou et al., 2017, 2019).

Despite the potential of these methods, their main drawbacks stem from the spatio-temporal heterogeneity of altimetric measurements. The creation of a daily gridded product requires an optimal spatio-temporal interpolation between the satellite track measurements. This produces low-resolution fields (1/12° in the Mediterranean Sea) with a limit on the spatial scales resolved as well as uncertainty in areas which have not been sampled by satellites. We refer to these products here on as AVISO/CMEMS altimetry maps, referring to their provider for the Mediterranean Sea.

These limitations have been quantified by Amores et al., 2018. They have shown that mesoscale eddies in the North Atlantic Ocean and the Mediterranean Sea could be overestimated by a 19% and 8 % respectively. Besides, according to the same study sub-mesoscale eddies, i.e. those with sizes smaller than the mesoscale, are undersampled by 94% and 84% respectively for these two regions due to the coarse resolution of the AVISO/CMEMS altimetry products.

Real-time eddy tracking on altimetry maps is also constrained, as eddies can be "lost" by the tracking algorithms, when crossing an area at a time when it is not sampled by any satellite tracks. Similarly, they could be detected in a position prior to their real-time one, as a result of the last available measurement.

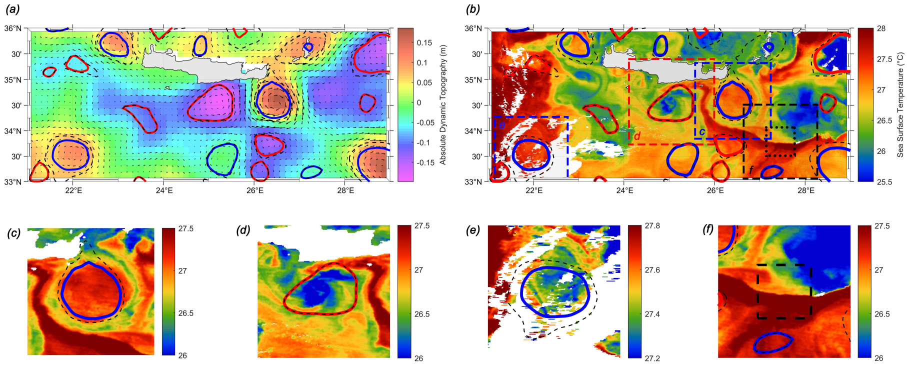

Figure III.1: (a) Absolute Dynamic Topography (altimetry) field with superimposed geostrophic velocity vectors and (b) Sea Surface Temperature field (white areas represent clouds) around Crete on the 24/08/2018. Maximum velocity contours (blue for AE and red for CE) and outermost contours (dashed lines) detected by AMEDA on the velocity field are superimposed on both figures. In (b) some characteristic SST image patch selections are represented with dashed line *RoI* boxes: (c) A warm-core anticyclone image (d) A cold-core cyclone image (e) A cold-core anticyclone image covered by clouds (f) A non-eddy image, with the area of no-contour constrain outlined with a dashed line.

III.1.3 Why Deep Learning for eddy signature classification?

Eddy signatures are nevertheless also apparent in visible satellite imagery such as Sea Surface Temperature (SST), Ocean Color/Chlorophyll (CHL), or synthetic-aperture radar (SAR) images. These images have an average resolution ten times higher than that of altimetry and are not a product of interpolation. However, they are strongly affected by cloud coverage which creates missing values in the observation. This effect is especially prominent during day-time and winter-month measurements.

Several methods of eddy detection have been developed on SST images: D'Alimonte, 2009 approach the problem through iso-SST pattern recognition to detect swirling fronts and gradients. In Dong et al., 2011 the velocity field is derived from the SST field through the assumption of the thermal wind equation. Finally Castellani, 2006 conducted an early study training an Artificial Neural Network with gradient-based methods for eddy detection on the SST field. However, as the sign of the core surface temperature anomaly (warm core or cold core), is not always correlated to the eddy sign (anticyclonic or cyclonic), a robust method for eddy detection on SST cannot be based on the thermal wind equation and the temperature gradients.

Deep Learning has been rapidly gaining in popularity and solving problems in remote sensing (L. Zhang et al., 2016), climate and the environment (Rolnick et al., 2019). Machine learning methods have also been used in previous studies to tackle altimetric eddy detection and tracking on the SSH field. In Lguensat et al., 2018 and Franz et al., 2018 a pixel-wise segmentation approach is adopted, with the original labeling of the train set stemming from geometrical eddy detection methods on the sea surface height field. Similarly in Ashkezari et al., 2016 the a geometrical eddy detection method is used to label training data derived from the velocity field. These studies while successfully exploring novel methods for eddy detection application, stumble upon the inherent limitation of the gridded altimetric products, on which the learning dataset is based. The measurement error will therefore propagate throughout the whole training process. In visible imagery, Deep Learning has been employed by Huang et al., 2017to classify eddy signatures on SAR images.

Here, following Moschos et al., 2020, we employ Convolutional Neural Networks to build a Sea Surface Temperature eddy signature classifier, a tool which can serve for validating and correcting altimetry eddy detections. This study provides contributions in automatically retaining a large dataset of SST patches with eddy signatures and constructing a CNN-based classifier of sea temperature eddy signatures. Our classifier achieves very high performance on coherent eddy signatures while being robust to high levels of cloud coverage.

The structure of this study is as follows: In Section III.2 an automatic method is presented to retain a large dataset of SST image patches containing eddy signatures based on altimetry detection region proposal. In Section III.3 the methods used to train and evaluate CNN-based classifiers are described. In Section III.4 the performance of the classifiers is evaluated on images containing coherent eddy signatures. Subsequently, in Section III.5 we assess the effect of cloud coverage on the performance of the classification. Finally, in Section III.6 main conclusions on the given task and future prospects of Deep Learning for eddy detection are discussed.

III.2 Dataset creation and features

The task of this study consists in classifying SST images which can contain either the signature of an Anticyclonic Eddy (AE), a Cyclonic Eddy (CE) or No Eddy signature (NE). Anticyclones (cyclones) rotate in the opposite (same) direction with the earth's rotation, viz. clockwise (counter-clockwise) in the Northern Hemisphere. To this end a dataset containing such SST image patches needs to be extracted from images of larger domains. In this section a regional proposal method through altimetric detection is presented, and the extracted dataset is presented.

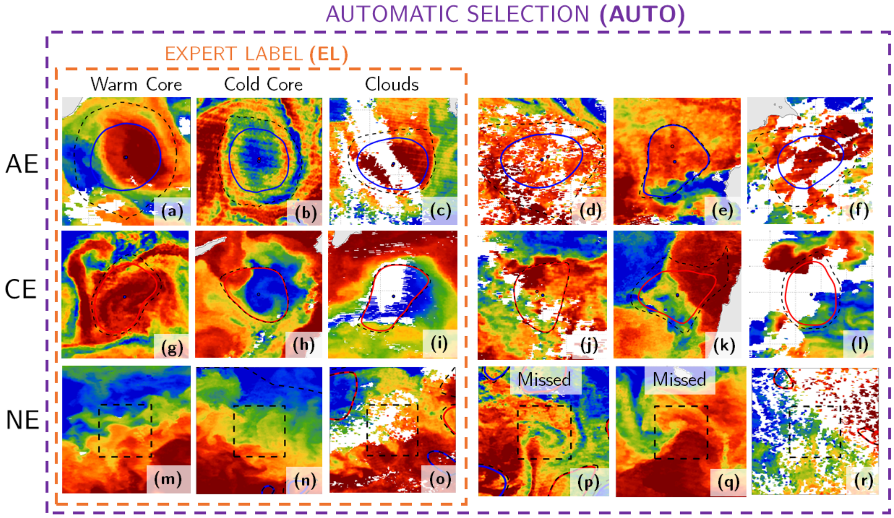

Figure III.2: Samples of images contained in the datasets. The dashed orange line box outlines coherent examples, representative of the EDDIES-EL dataset (coherent signatures), while the dashed purple line box outlines examples representative of the EDDIES-AUTO dataset (automatic selection). Row values represent the dataset labels while columns categorize coherent signature characteristics (sign of core temperature anomaly, Cloud Coverage). In the EDDIES-AUTO set, images retained through the altimetric detection regional proposal might not have a visible eddy signature on the SST, as seen in examples (d),(e) for AE, (j),(k) for CE. Similarly, images retained and labeled as NE, through the no-contour selection criterion (black dashed line box), can contain an eddy signature missed by altimetry as seen in examples (p) for an AE signature and (q) for a CE signature. Finally, examples (f),(l) and (r) represent images where validation of their label is delicate for a human expert, due to strong cloud coverage.

III.2.1 Region proposal through altimetric eddy detections

The domain of the dataset of this study is the Mediterranean Sea on a 3-year time period (2016-2018). Two data sources are considered:

- **SST images** are received on daily time intervals from the Copernicus - Marine environment monitoring service. These high-resolution (1/120°) images are a product of supercollation, as described in Nardelli et al., 2013 and stem from merged multisensor data, representative of nightime *SST* values.

- **Eddy locations and contours** are retained by applying the AMEDA on daily Adjusted Dynamic Topography and the AVISO/CMEMS surface geostrophic velocity fields with applied cyclogeostrophic corrections (Ioannou et al., 2019). The AMEDA (Le Vu et al., 2018) (Script on GitHub by B.Le Vu) detects eddies by identifying minima and maxima of the Local Normalized Angular Momentum (LNAM), computed on the surface velocity fields, and selecting closed streamlines around them. The algorithm does also dynamically track eddies backward and forward in time, as well as identifies their merging and splitting events. Eddy tracks detected by AMEDA, are labeled as AE or CE based their LNAM sign and are supplied with other metadata such as:

- The contour of the eddy where the velocity is maximum (here on *"contour"*, shown with a bold blue line for AE and a bold red line for CE in figures). Its corresponding values of the radius R_{max} of an equal-area circular contour and of the velocity V_{max} along it.
- The geometrical barycenter of the maximum velocity contour.
- The outermost contour of the eddy (shown with a dashed black line in figures).

To extract image patches containing eddy signatures from daily SST maps the detections of AMEDA on corresponding daily altimetric maps are used as a regional proposal tool. Regions of Interest (RoI) are centered on the barycenters of the altimetric contours, scaled according to the physical eddy size and then interpolated to a constant pixel size. This process is illustrated in Figure III.1.

The RoI physical size corresponds to $k = \lambda * R_{max}$, where $\lambda = 5$. RoI are cropped and interpolated to a constant size of $m = \lambda * \bar{R}_{max}(km)$, through a nearest neighbour interpolation method. $\bar{R}_{max} = 42km$ is the mean radius of the maximum velocity contour of all the contours retained in this study retained in this study, following a lognormal distribution with a standard deviation of $\sigma = 9km$. This results to retained rectangular image patches of side $m = 230$ pixels, labeled as AE or CE following the corresponding altimetric contour. Examples of AE and CE selections are shown in Figure III.1 (c) and (d).

To extract SST image patches that do not contain an eddy signature, a box of size $m = 230$ pixels is slided along the domain of the Mediterranean Sea, with a stride of $m/2$ pixels. This way RoI are retained, on the condition that they do not contain any contour inside a centered area of side R_{max}, and labeled as NE. A NE selection example can be seen in Figure III.1 (f). The no-contour centered area of side R_{max} is visualized in figures through a black dashed line box.

III.2.2 Dataset creation and labeling

Examples of images retained through the aforementioned process are given in Figure III.2. These images are used to create datasets, which are used for training and testing CNN-based classifiers. The characteristics of the datasets used in this study are outlined in Table III.1.

Table III.1: Dataset Characteristics

Dataset Name	Type	Year	Image No.	AE:CE:NE
EDDIES-EL(16/17)	Train	2016-17	3600	1:1:1
EDDIES-AUTO(16/17)	Train	2016-17	24000	1:1:2
EDDIES-EL(18)	Test	2018	1200	1:1:1
EDDIES-CLOUDY(18)	Test	2018	8x10x300	1:1:1

Table III.2: Core Temperature Anomaly Signature

Class / Core	AE	CE
Warm Core	60 ± 5%	35 ± 5%
Cold Core	40 ± 5%	65 ± 5%

As seen in Figure III.2, eddy SST signatures are differentiated both by their sense of rotation (AE/CE) as well as the sign of their core temperature anomaly (Warm/Cold). By visually inspecting a sample of the automatically retained images, we quantify that $60 \pm 5\%$ of AE images depict a Warm Core anomaly signature and $65 \pm 5\%$ of CE images depict a Cold Core one, as can be seen in Table III.2. Thus, while the temperature anomaly inferred by the thermal wind equation is dominant for each of the classes a large sample of inverse core anomaly signature images, that is Cold (Warm) Core Anticyclones (Cyclones), exist in our dataset. These inverse core anomaly signatures could be forced either by the summer thermocline or by subsurface underlying mechanisms (Assassi et al., 2016; Trott et al., 2019). This variety of visible SST patterns favors the use of deep neural networks for eddy signature classification.

Image labels received by the altimetric region proposal do not necessarily visually correspond to the SST signature depicted in them. This can be due to various reasons:

- Uncertainty of the AVISO/CMEMS altimetry maps, due to interpolation between satellite track measurements.
- Error induced by the AMEDA algorithm.
- Strong cloud coverage of the SST signature.
- Unclear SST eddy signatures due to air-sea interactions.

A large dataset named **EDDIES-AUTO**, is automatically created as described above, and contains images with labels corresponding to 3 classes $k \in AE, CE, NE$. To filter out incorrect proposals stemming from altimetric detection, only the RoI that correspond to large ($R_{max} > 26km$) and intense ($V_{max} > 6cm/s$) eddies detected by altimetry are retained.

Still, the automatically retrieved dataset contains images whose visual signature does not clearly refer to their assigned label, due to a combination of the aforementioned reasons. This set is denoted as $\tilde{D}$ and contains u examples $(x, \tilde{y})$. The labels retained by the altimetry region proposal automatic selection, are denoted as $\tilde{y}$ to refer to the presence of label noise.

The effect of label noise on the EDDIES-AUTO dataset is visualized in Figure III.2 : As an example, an Anticyclonic (AE) labeled image contained in this set can, have a visible signature that corresponds to its label (examples (a),(b),(c)) or one that does not (examples (d),(e)). Besides, delicate samples as the example (f), could lead experts having ambiguous opinions on its label. The same follows for the CE and NE labeled examples of Figure III.2.

Expert Labeling consists of a method which, albeit time-consuming can provide reliant and accurate labels. For the purposes of our study, oceanographic experts labeled a smaller dataset named **EDDIES-EL**, by selecting images with a coherent signature corresponding to their label. This set, denoted as $D \subset \tilde{D}$, contains images and accurate labels (x, y). The probability distribution $p(x, y)$ reflects the true distribution of the True Labels y between the three classes.

Representative examples of the coherent signatures images contained in EDDIES-EL can be seen outlined by a orange dashed line in Figure III.2. Their SST signature can be distincted based on the sign of the eddy core temperature anomaly, leading to warm (examples (a),(g)) and cold core (examples (b),(h)) eddies. Both AE/CE have warm and core core examples in the EDDIES-HL set, in contrast to what is usually assumed through the thermal wind balance. Furthermore, images corrupted by clouds are included on this set (examples (c),(i),(o)), only when their signature is clearly visible to a human expert.

By defining the label-noise distribution $p(\tilde{y}|y, x)$ we can specify the level of discrepancy between the expert labeling and the noisy labels obtained by the automatic altimetry region proposal. This distribution for the EDDIES-AUTO dataset can be inferred by manually labeling a random sample of v images, with $v/u \ll 1$. We receive thus the 3 by 3 sized noise matrix of probabilities:

$$N_{ij} = p(\tilde{y} = j | y = i) \tag{III.1}$$

The noise matrix of the EDDIES-AUTO dataset, sampled by different experts on 400 examples of each class is shown in Figure III.3. On average, 42 % of AE and 30 % of CE images are confirmed to have a humanly visible signature corresponding to their label. The rest of the images with these labels, but no humanly visible eddy signature, are allocated to the NE class. Likewise, out of the sampled NE-labeled images, an average 5% allocated to each of the AE and CE classes. This reflects the percentage of eddies missed by altimetric detection, corresponding to examples (p) and (q) of Figure III.2. Overall, the noise matrix evaluation shows that less than half of the eddy labeled (AE,CE) images in the

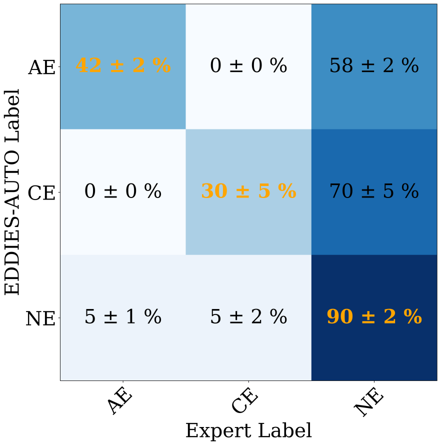

Figure III.3: Noise Matrix N_{ij} for the EDDIES-AUTO dataset, received by manually labeling 400 random samples per class, by different experts. Row values represent the labels in the EDDIES-AUTO dataset, while column values the labels assigned by experts. Cell values are normalized by the total number of sampled images per class.

EDDIES-AUTO dataset have a humanly visible signature corresponding to their labels. Additionally, a small fraction of the NE labeled images contain missed eddy signatures. This discrepancy between visible signatures and labels portrays the effect of noisy labeling on this dataset, and is tackled through a transfer learning approach in the next sections.

III.2.3 Cloud Coverage

Cloud coverage has a direct impact on SST images and on the learning process, as it creates missing values in the sampled images, and often corrupts the signature apparent in the image. Cloud coverage is also related with $p(\tilde{y}|y, x)$: the ability to infer the True Label y of a cloud-covered signature depends on both the location and the density of the cloud pattern.

To quantify the presence of clouds in the datasets used in this study, a cloud coverage percentage (CCP) is calculated for every Region of Interest as:

$$CCP = n_{NaN}/m^2 \tag{III.2}$$

where n_{NaN} is the number of missing value pixels in each image, excluding the ones that represent the coast and $m = 230$ is the RoI side in pixels.

The distribution of CCP values is quantified in Figure III.4. With a black line, the histogram of CCP values is plotted for all the available RoI to be retained through the regional proposal methodology. Out of them, only images under a threshold of 80% of Cloud Coverage are retained on the EDDIES-AUTO dataset (Figure III.4, Purple Line). Thus images with a large degree of cloud

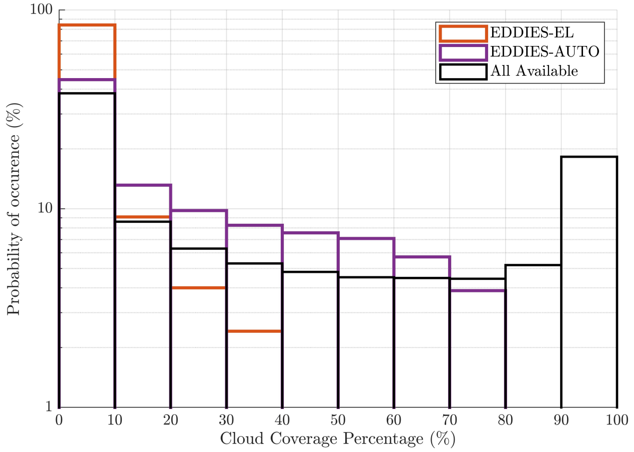

Figure III.4: Distribution of Cloud Coverage Percentages in: The EDDIES-EL dataset (Orange Line), the EDDIES-AUTO dataset (Purple Line) and all the available RoI in the sampled domain, before applying thresholds on image retainment (Black Line).

coverage (last two black line bins of Figure III.4) which completely corrupts the temperature signature are avoided. Finally, the EDDIES-EL dataset, has distribution with much lower values of CCP, due to the expert selection process: more than 80% of images in the EDDIES-HL have only $0-10\%$ of cloud-coverage (Orange Line, Figure III.4).

III.3 Deep Learning Architecture and Training

Convolutional Neural Networks (LeCun et al., 1989) have been successfully used in numerous computer vision applications, including ones of remote sensing. In this section we describe the architecture of a CNN-based classifier and the methods used in the training process. We also introduce a transfer learning scheme as well as indices of evaluation of the classification performance.

III.3.1 CNN Architecture

Due to the large size of the dataset and the complexity of the image features, a deep CNN architecture is used to build a classifier. Residual networks (He et al., 2016) utilize skip connection between layers in order to build efficient deep architectures. Here, a ResNet18 architecture, with 18 fully-connected layers and skip connections, is used through the torchvision package of the Pytorch library.

The input layer of the network is modified so that a two channel input image can be received: The first channel represents the normalized temperature values and the second channel a semantic mask representing missing data locations.

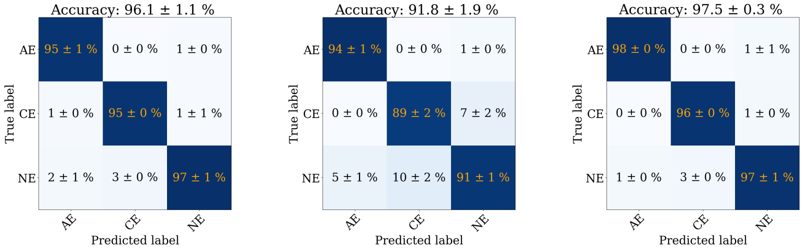

(a) Classifier-EL (b) Classifier-AUTO (c) Classifier-AUTO/EL

Figure III.5: Confusion Matrices on the EDDIES-EL(18) test set. Two models, trained on different datasets through a 5-fold cross-validation, are evaluated. Cell values represent the mean ± the standard deviation of the C_{ij}^{pre} of the classifiers trained on 5 different folds of the corresponding dataset.

The final layer of the network is also adapted to a three-class output, normalized through the softmax equation. Training and weight update is performed through a cross-entropy loss and stochastic gradient descent with momentum.

III.3.2 Training methods and transfer learning

Random orthogonal rotation is performed on input images during the training process, in order to achieve rotational invariant model training. Rotational data augmentation provides both a different geometric perspective as well as potential alternative instants of image that depict physically rotating structures.

A 5-fold cross-validation is performed in all model training runs. A different 20% of the train set, serves each time for validating the performance after every training epoch. To avoid overfitting, regularization is performed in the training process. An early stopping scheme is adopted based on the loss of the validation set. Training time of one fold is on the order of 5 minutes for the EDDIES-EL dataset and 1 hour for the EDDIES-AUTO dataset, on an NVIDIA K5000 GPU with a batch size of 4 and a learning rate of 10^{-3}.

Transfer learning aids CNN training aids by extracting features from a large dataset of images and utilizing the learned features for a more specific task. Here, this is performed by pretraining CNNs on datasets of images larger than the specific task. We then train these pretrained CNNs by unfreezing all layers, and thus using a pretrained weight initialization scheme. In our experiments, we pretrain in two different datasets:

- All the ResNets trained for the purposes of this study are already pretrained on Imagenet, a large dataset of more than 14 million images. This way, weight initialization is performed with the shallower layers being able to detect common image features such as edges or gradients.

- Pretraining is also performed on the larger EDDIES-AUTO dataset, providing weight initialization for finetuning on the EDDIES-EL dataset. The model trained this way is referenced as $AUTO/EL$.

III.3.3 Trained Classifiers and evaluation indices

We train three different classifiers, through the 5-fold cross-validation scheme:

- **Classifier-EL** is trained on the EDDIES-EL(16/17) dataset, that is on a relatively small amount of coherent signature images, with weak cloud coverage, whose labels can be directly validated by an expert.
- **Classifier-AUTO** is trained on the EDDIES-AUTO(16/17) dataset, that is on a more diverse set of images, with strong cloud coverage and presence of label noise.
- **Classifier-AUTO/EL** is first pretrained on the EDDIES-AUTO(16/17) dataset, and then finetuned on the EDDIES-EL(16/17) dataset. Finetuning is performed on all layers of the CNN. This way features from the more diverse in signatures and cloud-coverage EDDIES-AUTO dataset can be extracted, while finetuning on the EDDIES-EL dataset of coherent signatures.

Evaluation of the classifiers is performed on test sets in the form of precision normalized confusion matrices. Each cell (i, j) of the 3 by 3 sized matrix represents the precision defined as the probability of an image predicted by the classifier (y_{pred}) in class j to be labeled in the dataset (y_{true}) as class i:

$$C_{ij}^{pre} = p(y_{pred} = j | y_{true} = i) \tag{III.3}$$

Values of equation III.3, where $i = j$, i.e. at the diagonal of the confusion matrix, are referred to as the Class Precision. In order for the CNN-classifier to be confident in the eddy signature classification task, high values of class precision are required for the AE and CE classes.

The overall evaluation of a classifier can also be performed through the Classification Accuracy, a metric robust for class-balanced test sets. The classification accuracy is defined as the percentage of images predicted correctly in the test set used for evaluation:

$$A = p(y_{pred} = y_{true}) \tag{III.4}$$

By performing a 5-fold cross-validation training, precision and accuracy values are provided in a mean ± standard deviation form, between the evaluation of the different training folds.

III.4 Classification of coherent signatures

The classification performance is firstly evaluated on images containing coherent signature with a small or no amount of corruption due to cloud coverage. To this end, the EDDIES-EL(18) test set is used in order to evaluate classifier

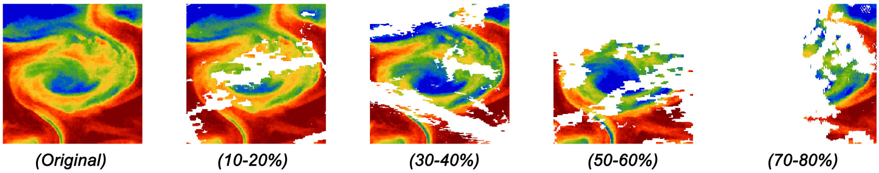

(a) Anticyclonic Eddy Example

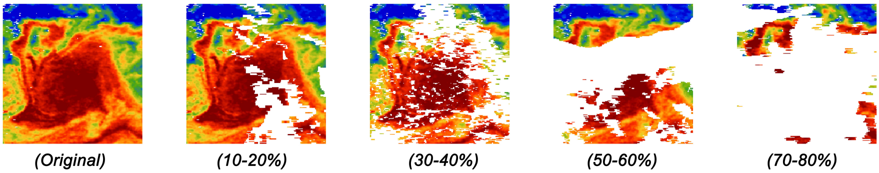

(b) Cyclonic Eddy Example

Figure III.6: Examples of Cloud Data Augmentation of an AE (top line) and a CE (bottom line) from the EDDIES-CLOUDY set. The original image from the EDDIES-HL(18) test set, along with multiple examples with different levels of cloud coverage percentages are visualized. The corruption is performed by superimposing random cloudy masks from an auxiliary EDDIES-AUTO(18) set. All of the examples in this figure were correctly predicted as AE/CE correspondigly by the Classifier AUTO/EL. Colour range is on the $5_{th} - 95_{th}$ percentiles of the non-missing pixels.

performance. The three trained classifiers (EL,AUTO,AUTO/EL) are intercompared based on the precision normalized confusion matrices. The confusion matrices of Figure III.5 show the precisions C_{ij}^{pre} for each of the given cells.

All classifiers show a robust performance on the EDDIES-EL test set, with mean classification accuracies of $91.8 \pm 1.9\%$ (Classifier-AUTO), $96.1 \pm 1.1\%$ (Classifier-EL) and $97.5 \pm 0.3\%$. (Classifier-AUTO/EL). The high classification accuracy achieved by the Classifier-EL shows that by training on a small dataset of coherent signature images, as is the EDDIES-EL(16/17) train set, a classifier with robust performance on these type of examples can be constructed.

The effect of noisy labeling of the EDDIES-AUTO(16/17) set in the training process can also be seen here: The Classifier-AUTO achieves the lowest classification accuracy between the three classifiers, when evaluating on a dataset of coherent signature images (Figure III.5b). However, by finetuning it on the EDDIES-EL dataset, the received Classifier-AUTO/EL achieves the best performance between the three by increasing the mean and reducing the standard deviation of the classification accuracy (Figure III.5c).

Nevertheless, the experiment presented here is evaluated on a dataset containing signatures which are much more clear that the ones existing in the whole domain of application. The robustness of classification on examples with strong cloud coverage corrupting the SST signature, is evaluated on the next section.

III.5 Classification of cloud-covered signatures

Cloud coverage is present in automatically sampled images from the domain of application. Strong cloud coverage can partially or completely corrupt the SST signature apparent in the sampled image, rendering the classification task delicate even when manually performed by an oceanographic expert. In this section, the robustness of a CNN-based classification on images corrupted by different degrees of cloud coverage is examined, providing an assessment on its performance on samples encountered in the real domain of application.

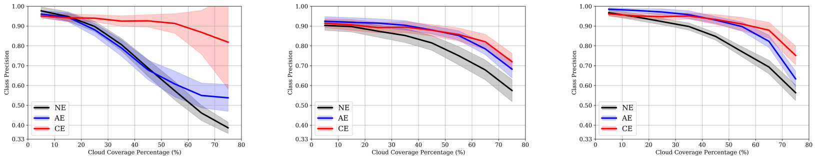

(a) Class Precision: EL (b) Class Precision: AUTO (c) Class Precision: AUTO/EL

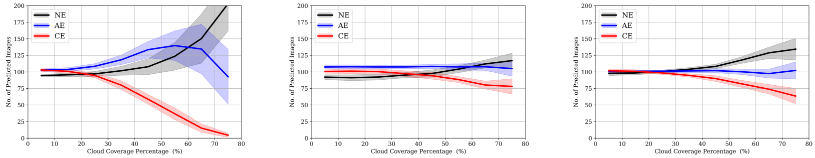

(d) Prediction Rate: EL (e) Prediction Rate: AUTO (f) Prediction Rate: AUTO/EL

Figure III.7: Classifier performance the EDDIES-CLOUDY dataset. The y-axis of figures on the top line represents the Class Precision $C^{pre}_{i=j}$ and on the bottom line the number of predicted images per class. Bold lines and envelopes represent respectively the mean and standard deviation of experiment runs (5-fold training and 10 test sets per CCP bin). Colours represent the performance over the three different classes (black for NE, blue for AE, red for CE). The x-axis represents the mean Cloud Coverage Percentage (CCP) range of the test set (0-10% to 70-80%). Figures in different columns show the performance of different classifiers.

III.5.1 Cloud Data Augmentation

The EDDIES-AUTO dataset has a distribution with higher cloud coverage values than the EDDIES-EL dataset (Figure III.4), and is therefore more depictive of the application domain, albeit being limited by the 80% threshold on CCP. Nevertheless, the noisy labeling of the EDDIES-AUTO dataset creates a discrepancy between visible signatures and image labels. Therefore, using this dataset to test the CNN-based classifier, does not allow for a confident evaluation of their robustness to cloud coverage. To tackle this issue, a test set representative of cloud values is constructed based on the coherent signature images contained in EDDIES-EL(18) test set, whose labels have been validated by experts.

The produced augmented test set, named **EDDIES-CLOUDY** here on, is created by randomly adding to the images contained in the EDDIES-EL test set, cloud masks which are retrieved from the EDDIES-AUTO dataset. This way a test set of images with expert-validated labels is produced, which is also corrupted by realistic cloud patterns, effectively simulating samples from the domain of application of the classifier. The cloud masks are extracted from images corresponding to the year 2018, so that the same cloud patterns appearing in the images used for training the classifiers, corresponding to years 2016/2017, are not repeated in the EDDIES-CLOUDY test sets.

Masks are randomly added to each of 300 images selected from the EDDIES-EL test set, in order to create corrupted images falling in 8 different bins of cloud percentages ($0 - 10\%$ to $70 - 80\%$). 10 random corruption realizations for each original uncorrupted image are performed for each of the 8 cloud range bins, creating 80 class-balanced test sets of 300, for a total of 24000 images (see Table III.1) Algorithm 1 describes the iterative process followed for the test data augmentation.

Algorithm 1: Cloud Data Augmentation

```
Input: Datasets: EL{Contains 300 uncorrupted images}, AUTO
       {Contains cloud masks}
Output: CLOUDY {80 sets of 300 images}
initialization;
for cbin = 10-20 to 70-80% {Loop over CCP bins} do
    for rep = 1 to 10 {Repeat different masks} do
        for img = 1 to 300 {Repeat for img in EL} do
            Get uncorrupted img from EL;
            Compute CCP of img;
            while CCP outside of cbin do
                Get random mask from AUTO;
                Apply random mask on uncor. img;
                Compute CCP of corrupted img;
            end
            Save corrupted img to CLOUDY;
        end
    end
end
```

An example from the EDDIES-CLOUDY dataset is given in Figure III.6.

An AE (Fig. III.6a) and a CE (Fig III.6b) example from the EDDIES-EL(18) test set are corrupted with different levels of cloud coverage, here shown for the 10-20%, 30-40%, 50-60% and 70-80% bins. All of the visualized image samples were correctly predicted by the best performing classifier. The level of corruption caused by the cloud coverage on the eddy signature, is not only affected by the percentage of the missing values but also by their positioning on the image. In all of the examples, a part of the information important for the correct classification of the image (core anomaly signature, swirling filaments) is still visible, despite the image corruption, and exploited by the CNN to achieve correct classification.

III.5.2 Experimental results

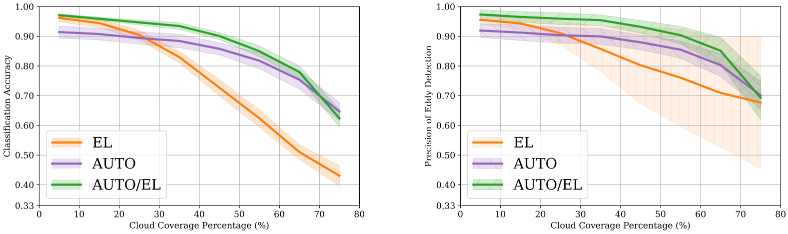

(a) Accuracy (b) Precision of Eddy Detection

Figure III.8: Intercomparison of classifier performance on the EDDIES-CLOUDY test sets: Classifier-EL (organge), Classifier-AUTO (purple), Classifier-AUTO/EL (green). The classifiers are compared based on their (a) Classification Accuracy (ratio of correctly predicted images in the EDDIES-CLOUDY test sets) and (b) Precision of Eddy Detection (mean of AE and CE precision). The best performing Classifier AUTO/EL shows very high accuracy and precision (> 0.90) for images with up to 50% of CCP while also being robust to images with even higher amounts of cloud coverage.

The CNN-based classifiers, previously evaluated on the EDDIES-EL test set, are now assesed on their ability to correctly predict the label of cloud-corrupted images contained in the EDDIES-CLOUDY test sets. This is evaluated by computing the Class Precision $C_{i=j}^{pre}$ (i.e. the values corresponding to the diagonal of the normalized confusion matrices) for each of the three classes. For each of the 8 cloud range bins, the values of $C_{i=j}^{pre}$ are calculated by running the 5-fold corss-validated models on each of the 10 test set repetitions. A mean and a standard deviation of the 50 (5x10) received class precision values is thus received, and plotted in the top-line of Figure III.7 as the thick line and the envelope respectively, for each of the three classes. A high mean precision on eddy-signature images means that a high fraction of images predicted as AE or CE will have a signature corresponding to their predicted label. A thinner envelope shows convergence between different test realizations.

On the bottom line of Figure III.7 the number of predicted images per class is plotted on the y-axis. As before, the thick line and the envelope, represents respectively the mean and standard deviation of experiment runs. As each test set of 300 images is class balanced, 100 images per class suggest a balanced prediction, although that doesn't directly imply that these images were correctly predicted. To assess the performance of each classifier the information of Precision is combined with that of the Predicted numbers.

The Classifier-EL, trained on coherent signature samples, while performing a high precision on test sets with small amounts of CCP, proves incapable of correctly predicting eddy signatures corrupted with strong levels of cloud coverage. This is depicted in Figures III.7a in which the initial high precision on AE images in the bin $0-10\%$ of cloud coverage, drops rapidly for increasing values of CCP. The high precision on CE images for high values of CCP is caused by the large drop in the amount of images predicted as CE (Fig III.7d). This is also visualized by the large spread of the envelope in the CE precision. However, the EDDIES-EL train set used here, contains images with CCP up to 40% (Figure III.4). Nevertheless, the AE class scores an above-random precision (ranging from 70% to 55%) for images with CCP of 40-80%. This demonstrates the ability of the classifier to generalize learning on treating missing values, as it has not encountered images with more than 40% of CCP during the training process.

The Classifier-AUTO, trained on a wider variety of samples with up to 80% of cloud coverage, shows a more robust performance on the EDDIES-CLOUDY test sets. Starting from the same point of high precisions for the $0-10\%$ cloud coverage bin, this classifier sustains high values of precisions for increasing values of CCP (Figure III.7b), while prediction numbers remain almost class balanced (100 images per class), up until the $40-50\%$ cloud coverage bin (Figure III.7e). For higher values of CCP, the balance of predicted CE rates drops in favour of more NE predictions.

Precision on the EDDIES-CLOUDY test sets is furtherly augmented by Classifier-AUTO/EL (Figure III.7c), which consists of the previous classifier finetuned on EDDIES-EL. When compared to the precisions of Classifier-AUTO, Classifier-AUTO/EL shows a common behaviour on the test set, with yet an increased mean precision of 0.05 on the eddy-classes (AE and CE), and a thinner envelope for the NE class, up until the $40-50\%$ cloud coverage bin. The balance of predicted image numbers (Figure III.7f) is also stable (80-120 images per class) up until the $40-50\%$ bin, above which there is likewise a drop in CE and a gain in NE predictions.

The inter-comparison of the three classifiers is more precisely depicted in Figure III.8: The precision of eddy detection, that is the mean between the precisions of the red and blue lines in the top line of Figure III.7 is shown in Figure III.8b. The higher robustness of Classifier-AUTO to Classifier-EL is depicted here. The first has a higher mean and a lower standard deviation of eddy detection precision as values of CCP increase. A further difference in precision of eddy detection of 0.05 is obtained by the Classifier-AUTO/EL up until the $40-50\%$ cloud coverage bin, after which it narrows down to zero.

An inter-model comparison of the classification accuracies (Eq. III.4) for increasing CCP ranges on Figure III.8a shows essentially the same behaviour: training on the EDDIES-AUTO dataset proves more robust to cloud coverage than training on the EDDIES-EL dataset, while pretraining on EDDIES-AUTO and finetuning on EDDIES-EL, furtherly improves classification accuracy on clear signature images.

Overall, the best performing Classifier-AUTO/EL, achieves a considerable precision of more than 90% for the AE and CE classes and more than 80% for the NE class, for images with up to 50% of cloud coverage. It still shows robust performance for images with up to 80% of cloud coverage, although with a lower precision, with a minimum of 70% mean precision of eddy detection. Robustness on classification of cloud covered eddy signature images is higher for Anticyclonic than Cyclonic signatures, shown by the stable number of AE predictions (Figure III.7f). This depicts the fact that cyclones have a more complex, and difficult to classify, signature on the SST.

The pretraining methodology followed here, allows for feature extraction from a large, automatically retained dataset with a high variety of signatures, corrupted by missing values and with presence of label noise.. By finetuning a classifier trained on such images on a smaller subset of coherent signatures with accurate labels, we show that coherent signature, uncorrupted cases can be classified with almost no error, while maintaining a robust performance on images corrupted by missing values.

The Deep Learning approach also achieves a performance which exceeds that of an oceanographic human expert in classifying eddy signatures with strong cloud coverage: the Classifier AUTO/EL proves able to correctly classify eddy signatures with up to 80% of cloud coverage with an increasing amount of error as CCP increases. However, when asked to perform the same task, human experts only selected images with up to 40% of CCP (Figure III.4) to assign them as coherent eddy signatures. Such an approach can therefore aid not only in automating a time-costly task but also in achieving a superior performance.

III.6 Conclusion

In this study a novel Deep Learning approach is presented to validate the detection of mesoscale eddies from standard altimetry products, using Sea Surface Temperature images. An SST image CNN-based classifier is trained, showing potential to detect eddy signatures, even if the images are corrupted by a high level of cloud coverage. Such a classifier can be used as a tool to validate or correct standard eddy detections based on altimetry products, which are often uncertain due the to interpolation between satellite track measurements. Our trained Neural Network can automate the human-expert detection of eddy signatures on SST image patches, and even surpass it on signatures under strong cloud coverage.

A methodology to automatically retain a large dataset of SST image samples, based on altimetric detection region proposal, is first presented. However, a dataset retrieved this way contains a large number of noisy labels, due to complex eddy signatures or to a significant amount cloud coverage. On the other hand, a smaller subset of coherent signature images is labeled by oceanographic expert, in order to extract a reference dataset with coherent eddy signature images.

The best performing SST eddy signature classifier is constructed by pretraining a ResNet18 CNN on a large dataset of automatically retained images, and then fine tuning it on a smaller subset of coherent signature, expert labeled ones. A mean classification accuracy of 97.5% is achieved on a test set containing coherent eddy signatures.

Our classifier achieves significant performance on cloud-covered eddy-signature images, with a precision larger than 90% on Anticyclonic and Cyclonic signature predictions for images having up to 50% of cloud coverage. Furthermore it shows robust performance on images with 80% of cloud coverage, reaching a minimum mean precision of 70% on eddy detection.

It is demonstrated thus that a CNN-based classifier can successfully exploit the high-resolution information available on visible imagery such as the SST, while being robust to strong cloud coverage. From an oceanographic point of view, our classifier can provide an automatic validation of altimetric eddy detections by processing the information in SST images. Moreover, the Deep Learning approach followed here, exceeds the performance of human experts on correctly classifying such images when they are corrupted by a large amount of cloud coverage. Besides, our classification tool can also be exploited to furtherly analyze and characterize the complex surface temperature signatures of oceanic eddies.

From a machine learning point of view, a task is presented where pretraining on a large set of complex and corrupted images and finetuning on a set of coherent signature ones, provides a robust training strategy. The ability of a CNN-based classifier to generalize the treatment of missing data is also assessed by corrupting coherent signature images with masks of existing missing value patterns.

Missing values in large-domain SST imagery could also be treated by data-driven methods. This way, spatio-temporaly interpolated products, without missing values could be produced, while preserving the fine-scale structures, viz. eddies, in them. Studies have shown the potential of such data-driven approaches either by means of Data Assimilation (Fablet et al., 2017) or by Generative Adversarial Networks (Ayed et al., 2019).

The advantages of utilizing high-resolution visible satellite imagery for eddy-signature classification could be extended by using a multi-modal image input. The pattern information contained in all visible satellite imagery such as SST, Ocean Colour and SAR images could be exploited in a joint fashion.

Eventually, object detection and tracking CNN-based methods such as RCNN (Ren et al., 2015) or YOLO (Redmon et al., 2016) can be employed to construct an independent Deep Learning eddy detection and tracking algorithm on satellite imagery. Besides, future advances in satellite altimetry and imagery, will provide with increasing information of mesoscale and submesoscale eddy signatures.

References

Amores, A. et al. (2018). “Up to what extent can we characterize ocean eddies using present-day gridded altimetric products?” In: *Journal of Geophysical Research: Oceans* vol. 123, no. 10, pp. 7220–7236.

Ashkezari, M. D. et al. (2016). “Oceanic eddy detection and lifetime forecast using machine learning methods”. In: *Geophysical Research Letters* vol. 43, no. 23, pp. 12–234.

Assassi, C. et al. (2016). “An index to distinguish surface-and subsurface-intensified vortices from surface observations”. In: *Journal of Physical Oceanography* vol. 46, no. 8, pp. 2529–2552.

Ayed, I. et al. (2019). “Learning Dynamical Systems from Partial Observations”. In: *arXiv preprint arXiv:1902.11136*.

Brach, L. et al. (2018). “Anticyclonic eddies increase accumulation of microplastic in the North Atlantic subtropical gyre”. In: *Marine pollution bulletin* vol. 126, pp. 191–196.

Castellani, M. (2006). “Identification of eddies from sea surface temperature maps with neural networks”. In: *International journal of remote sensing* vol. 27, no. 8, pp. 1601–1618.

Chaigneau, A., Gizolme, A., and Grados, C. (2008). “Mesoscale eddies off Peru in altimeter records: Identification algorithms and eddy spatio-temporal patterns”. In: *Progress in Oceanography* vol. 79, no. 2-4, pp. 106–119.

Chelton, D. B., Schlax, M. G., and Samelson, R. M. (2011). “Global observations of nonlinear mesoscale eddies”. In: *Progress in oceanography* vol. 91, no. 2, pp. 167–216.

Chelton, D. B. et al. (2007). “Global observations of large oceanic eddies”. In: *Geophysical Research Letters* vol. 34, no. 15.

D’Alimonte, D. (2009). “Detection of mesoscale eddy-related structures through iso-SST patterns”. In: *IEEE Geoscience and Remote Sensing Letters* vol. 6, no. 2, pp. 189–193.

Dong, C. et al. (2011). “An automated approach to detect oceanic eddies from satellite remotely sensed sea surface temperature data”. In: *IEEE Geoscience and Remote Sensing Letters* vol. 8, no. 6, pp. 1055–1059.

Escudier, R. et al. (2016). “Eddy properties in the Western Mediterranean Sea from satellite altimetry and a numerical simulation”. In: *Journal of Geophysical Research: Oceans* vol. 121, no. 6, pp. 3990–4006.

Fablet, R., Viet, P. H., and Lguensat, R. (2017). “Data-driven Models for the Spatio-Temporal Interpolation of satellite-derived SST Fields”. In: *IEEE Transactions on Computational Imaging* vol. 3, no. 4, pp. 647–657.

Franz, K. et al. (2018). “Ocean eddy identification and tracking using neural networks”. In: *IGARSS 2018-2018 IEEE International Geoscience and Remote Sensing Symposium.* IEEE, pp. 6887–6890.

Frenger, I. et al. (2013). “Imprint of Southern Ocean eddies on winds, clouds and rainfall”. In: *Nature geoscience* vol. 6, no. 8, pp. 608–612.

Garreau, P. et al. (2018). “High-Resolution Observations and Tracking of a Dual-Core Anticyclonic Eddy in the Algerian Basin”. In: *Journal of Geophysical Research: Oceans*.

Gaube, P. et al. (2013). “Satellite observations of chlorophyll, phytoplankton biomass, and Ekman pumping in nonlinear mesoscale eddies”. In: *Journal of Geophysical Research: Oceans* vol. 118, no. 12, pp. 6349–6370.

He, K. et al. (2016). “Deep residual learning for image recognition”. In: *Proceedings of the IEEE conference on computer vision and pattern recognition*, pp. 770–778.

Huang, D. et al. (2017). “Deepeddy: A simple deep architecture for mesoscale oceanic eddy detection in sar images”. In: *2017 IEEE 14th International Conference on Networking, Sensing and Control (ICNSC)*. IEEE, pp. 673–678.

Ioannou, A. et al. (2017). “Dynamical evolution of intense Ierapetra eddies on a 22 year long period”. In: *Journal of Geophysical Research: Oceans* vol. 122, no. 11, pp. 9276–9298.

Ioannou, A. et al. (2019). “Cyclostrophic corrections of AVISO/DUACS surface velocities and its application to mesoscale eddies in the Mediterranean Sea”. In: *Journal of Geophysical Research: Oceans* vol. 124, no. 12, pp. 8913–8932.

Isern-Fontanet, J., Garcıa-Ladona, E., and Font, J. (2003). “Identification of marine eddies from altimetric maps”. In: *Journal of Atmospheric and Oceanic Technology* vol. 20, no. 5, pp. 772–778.

Klein, P. and Lapeyre, G. (2009). “The oceanic vertical pump induced by mesoscale and submesoscale turbulence”. In: *Annual review of marine science* vol. 1, pp. 351–375.

Kouketsu, S. et al. (2011). “The role of meso-scale eddies in mixed layer deepening and mode water formation in the western North Pacific”. In: *New Developments in Mode-Water Research*. Springer, pp. 59–73.

Laxenaire, R., Speich, S., and Stegner, A. (2019). “Evolution of the thermohaline structure of one Agulhas ring reconstructed from satellite altimetry and Argo floats”. In: *Journal of Geophysical Research: Oceans* vol. 124, no. 12, pp. 8969–9003.

Le Vu, B., Stegner, A., and Arsouze, T. (2018). “Angular Momentum Eddy Detection and tracking Algorithm (AMEDA) and its application to coastal eddy formation”. In: *Journal of Atmospheric and Oceanic Technology* vol. 35, no. 4, pp. 739–762.

LeCun, Y. et al. (1989). “Generalization and network design strategies”. In: *Connectionism in perspective*. Vol. 19. Citeseer.

Lguensat, R. et al. (2018). “EddyNet: A deep neural network for pixel-wise classification of oceanic eddies”. In: *IGARSS 2018-2018 IEEE International Geoscience and Remote Sensing Symposium*. IEEE, pp. 1764–1767.

Mazloff, M. R., Heimbach, P., and Wunsch, C. (2010). “An eddy-permitting Southern Ocean state estimate”. In: *Journal of Physical Oceanography* vol. 40, no. 5, pp. 880–899.

McGillicuddy, D. et al. (1998). “Influence of mesoscale eddies on new production in the Sargasso Sea”. In: *Nature* vol. 394, no. 6690, pp. 263–266.

McGillicuddy Jr, D. J. (2016). “Mechanisms of physical-biological-biogeochemical interaction at the oceanic mesoscale”. In: *Annual Review of Marine Science* vol. 8, pp. 125–159.

Mkhinini, N. et al. (2014). “Long-lived mesoscale eddies in the eastern Mediterranean Sea: Analysis of 20 years of AVISO geostrophic velocities”. In: *Journal of Geophysical Research: Oceans* vol. 119, no. 12, pp. 8603–8626.

Moschos, E. et al. (2020). “DEEP-SST-EDDIES: A Deep Learning framework to detect oceanic eddies in Sea Surface Temperature images”. In: *ICASSP 2020-2020 IEEE International Conference on Acoustics, Speech and Signal Processing (ICASSP).* IEEE, pp. 4307–4311.

Nardelli, B. B. et al. (2013). “High and Ultra-High resolution processing of satellite Sea Surface Temperature data over Southern European Seas in the framework of MyOcean project”. In: *Remote Sensing of Environment* vol. 129, pp. 1–16.

Nencioli, F. et al. (2010). “A vector geometry–based eddy detection algorithm and its application to a high-resolution numerical model product and high-frequency radar surface velocities in the Southern California Bight”. In: *Journal of atmospheric and oceanic technology* vol. 27, no. 3, pp. 564–579.

Okubo, A. (1970). “Horizontal dispersion of floatable particles in the vicinity of velocity singularities such as convergences”. In: *Deep sea research and oceanographic abstracts.* Vol. 17. 3. Elsevier, pp. 445–454.

Redmon, J. et al. (2016). “You only look once: Unified, real-time object detection”. In: *Proceedings of the IEEE conference on computer vision and pattern recognition*, pp. 779–788.

Ren, S. et al. (2015). “Faster r-cnn: Towards real-time object detection with region proposal networks”. In: *Advances in neural information processing systems*, pp. 91–99.

Rolnick, D. et al. (2019). “Tackling Climate Change with Machine Learning”. In: *arXiv preprint arXiv:1906.05433.*

Sadarjoen, I. A. and Post, F. H. (2000). “Detection, quantification, and tracking of vortices using streamline geometry”. In: *Computers & Graphics* vol. 24, no. 3, pp. 333–341.

Su, Z. et al. (2018). “Ocean submesoscales as a key component of the global heat budget”. In: *Nature communications* vol. 9, no. 1, pp. 1–8.

Trott, C. B. et al. (2019). “Eddy-induced temperature and salinity variability in the Arabian Sea”. In: *Geophysical Research Letters* vol. 46, no. 5, pp. 2734–2742.

Weiss, J. (1991). “The dynamics of enstrophy transfer in two-dimensional hydrodynamics”. In: *Physica D: Nonlinear Phenomena* vol. 48, no. 2-3, pp. 273–294.

Zhang, L., Zhang, L., and Du, B. (2016). “Deep learning for remote sensing data: A technical tutorial on the state of the art”. In: *IEEE Geoscience and Remote Sensing Magazine* vol. 4, no. 2, pp. 22–40.

Zhang, Z., Wang, W., and Qiu, B. (2014). “Oceanic mass transport by mesoscale eddies”. In: *Science* vol. 345, no. 6194, pp. 322–324.

Paper IV

Computer Vision for Ocean Eddy Detection in Infrared Imagery

Evangelos Moschos, Alisa Kugusheva, Paul Coste, Alexandre Stegner

Accepted for publication in *Winter Conference on Applications of Computer Vision 2023*

Abstract

Reliable and precise detection of ocean eddies can significantly improve the monitoring of the ocean surface and subsurface dynamics, besides the characterization of local hydrographical and biological properties, or the concentration pelagic species. Today, most of the eddy detection algorithms operate on satellite altimetry gridded observations, which provide daily maps of sea surface height and surface geostrophic velocity. However, the reliability and the spatial resolution of altimetry products is limited by the strong spatio-temporal averaging of the mapping procedure. Yet, the availability of high-resolution satellite imagery makes real-time object detection possible at a much finer scale, via advanced computer vision methods. We propose a novel eddy detection method via a transfer learning schema, using the ground truth of high-resolution ocean numerical models to link the characteristic streamlines of eddies with their signature (gradients, swirls, and filaments) on Sea Surface Temperature (SST). A trained, multi-task convolutional neural network is then employed to segment infrared satellite imagery of SST in order to retain the accurate position, size, and form of each detected eddy. The EddyScan-SST is an operational oceanographic module that provides, in real-time, key information on the ocean dynamics to maritime stakeholders.

IV.1 Introduction

Eddies, dynamical structures are to the oceans what weather systems are to the atmosphere. By transporting heat, momentum and mass from their regions of formation to distant areas, they affect they biological productivity (Chelton et al., 2011b), water transport (Zhang et al., 2014), local hydrographic properties (Dong et al., 2014) and the movement of pelagic species (Lobel et al., 1986). Mesoscale eddies, with radii of tens of kilometers and timescales on the order of

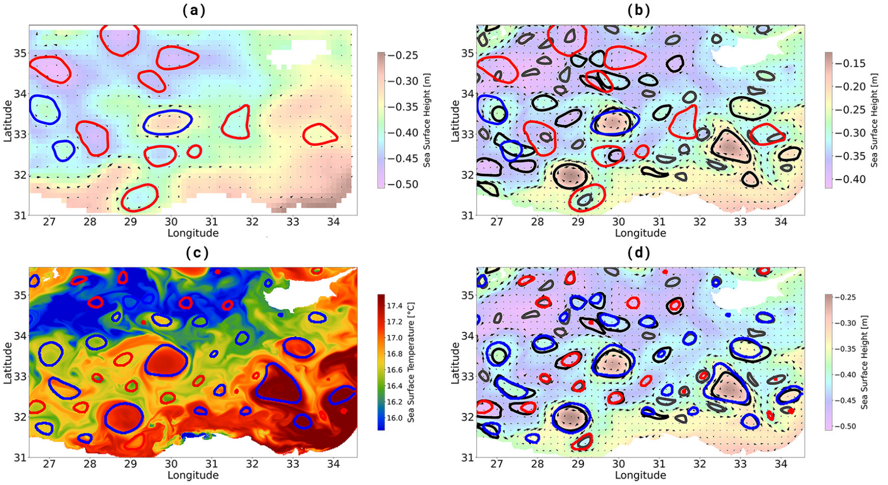

Figure IV.1: Examples of eddy detections on different satellite data. Blue (red) contours depict predicted anticyclones (cyclones). Black (grey) contours depict the mesoscale (submesoscale) reference geostrophic velocity eddies. (a) Standard eddy detection on simulated altimetric geostrophic velocity field (OSSE). (b) Reference contours and geostrophic velocity field with superimposed standard altimetric detections. (c) EddyScan CNN detections on SST data. (d) Reference contours and geostrophic velocity field with superimposed EddyScan detections.

months, amount for an oceanic energy partition on the order of the large ocean circulation (Gill et al., 1974; Zhang et al., 2014). This makes their detection and characterization crucial, both for the study of the climate evolution as well as day-to-day, operational oceanography.

The advances in Satellite Altimetry, measuring the Sea Surface Height (SSH) has led to 40 years of development of altimetric eddy detection (Holloway, 1986), revealing the prevalent role of eddies on ocean dynamics (Chelton et al., 2011a). As a result, many altimetric eddy detection and tracking algorithms (Isern-Fontanet et al., 2003; Le Vu et al., 2018; Mason et al., 2014; Nencioli et al., 2010; Pegliasco et al., 2022) have been recently developed. These algorithms, employ an objective function to detect eddies either on the SSH field or the derived geostrophic velocity field, which also stems from altimetry. Albeit the importance of standard altimetric eddy detection, strong limitations have been evoked: by simulating satellite altimetry products, Amores et al., 2018 showed that altimetric detection only captures 6 to 16 % of eddies in the North Atlantic Ocean and Mediterranean Sea respectively. In addition, they have calculated a constant bias of artificially larger detected eddies compared to their real size. In a study of the Mediterranean Sea, Stegner et al., 2021 showed that altimetric detection has a Missed (False Negative) rate of 34% and a Ghost

(False Positive) rate of 10% for large ($R > 20km$) eddies. These limitations of standard detection stem mainly from the altimetric observation, due to the strong spatio-temporal interpolation of SSH maps ($15km$ resolution), creating strong uncertainties in areas not covered by satellite tracks. Thus, the error of the altimetric data is of a larger order of magnitude than the error of the standard detection algorithms *per se*. On Figure V.1 (a) we plot the contours detected on a simulated altimetric geostrophic velocity field and compare them to those of the reference geostrophic velocity field at panel (b). Standard detection struggles to capture small and submesoscale eddies, because of the low resolution of the altimetry fields, while also miss-detects many larger eddies in areas not covered by tracks. To surpass these limitations, other sources of satellite data should be considered: the Sea Surface Temperature (SST) are high-resolution ($1km$) observations on the infrared spectrum where the signature of eddies is portrayed through gradients, swirls, and filaments.

Convolutional Neural Networks (CNNs) have been successfully employed to detect eddies on satellite data. Most of the work using CNNs is applied to altimetric data to perform semantic segmentation of maps of eddies (Duo et al., 2019; Franz et al., 2018; Lguensat et al., 2018). Yet, these successful implementations of Machine Learning stumble upon the inherent uncertainties of the altimetric observation data and the best of CNNs will only manage to replicate the best of standard eddy detection models. Two more studies (Lambhate et al., 2021; Liu et al., 2021) have employed CNNs that fuse SSH and SST data to improve semantic segmentation characterizing eddies as warm or cold core. They showed that adding SST as an independent source of data can lead to an improvement of eddy detection. However, the SST training data used need to be hand labeled or inferred by altimetric detections resulting in sparse/noisy labeling. Finally, classification of eddy signatures has been performed successfully by independently treating SST (Moschos et al., 2020b) and Synthetic Aperture Radar (SAR) data (Du et al., 2019). On Figure V.1 (c) we show the detections on the SST field of the CNN proposed in this paper, EddyScan-SST on SST, and compare them with the reference velocity field. Due to the high-resolution and accurate signatures of eddies on the SST, we manage to capture correctly most of the mesoscale eddies and an important part of the submesoscale (black and grey contours respectively; Figure V.1 (d)).

To perform an efficient operational eddy detection with CNNs two learning problems need to be treated successfully: the uncertainty of altimetric (SSH) eddy detections as ground truth, and the sparsity of ground truth in SST data. In this work we present EddyScan-SST, a pixel-wise segmentation CNN applied on SST data to detect with high precision the position, size, and form of eddies, without the need of an altimetry input. Our work provides several novelties in the task of eddy detection:

- Using CNNs, we infer from SST data the dynamical contours of eddies, which are local topological proxies of the field of velocities.
- As infrared satellite images are not linked with an accurate dynamical ground truth, we use a transfer learning schema, using ground truth

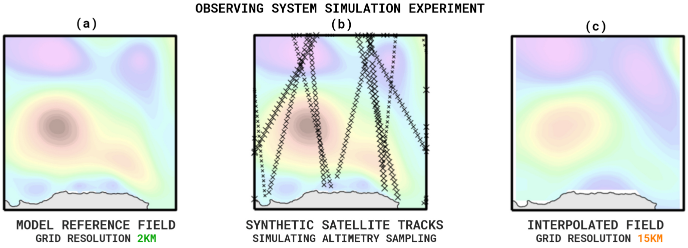

Figure IV.2: An OSSE consists of (a) Retaining a high-resolution numerical model field of SSH (b) Sampling the field via synthetic satellite tracks which simulate observation by altimeters (c) Inhomogenous spatio-temporal interpolation between the sampled points to receive the OSSE field. In our experiment grid resolution is degraded from 2km to 15km.

from ocean numerical model simulations, to learn representations of eddy dynamical contours on SST data.

- We use a multi-task learning schema to perform contour detection with correct position, size and form on both numerical model data and satellite infrared images.
- By testing on numerical model data and satellite images, we find that the CNN applied on SST greatly outperforms standard altimetric eddy detection when infrared observations are available.
- We provide a hand-labeled dataset of satellite infrared images containing eddy signatures and their corresponding dynamical contours for use by the oceanographic and vision communities.

IV.2 Data: Simulation and Observation

IV.2.1 The CROCO Numerical Model

The CROCO Numerical Model of the Ocean is a realistic numerical simulation of the ocean circulation, carried here on the domain of the Mediterranean Sea. CROCO is able to resolve very fine scales of ocean dynamics and their interactions with larger scales. The model solves the primitive equations on an grid, with a horizontal resolution of 2km in both longitudinal and latitudinal direction. We use in this study the SSH output of the numerical model as a reference (SSH REF) on which the Geostrophic Velocities are computed. We also use the output SST maps that correspond to the simulated dynamical field. These Numerical Model outputs serve as a reference ground truth for our experiments. Examples of the SSH and SST outputs of the CROCO Numerical Model are seen in panels (c) and (d) of Figure V.1.

IV.2.2 Observing System Simulation Experiment

The reference ground truth provided by the CROCO model simulations, as seen in Figure IV.2 (a), needs to be downsampled in an inhomogeneous manner, in order to reproduce the exact observation error found in the satellite altimetry. To do so, we perform an Observing System Simulation Experiment (OSSE) in a four-satellite configuration, composed of the reference mission Jason-3 and three other missions Sentinel3-A, Sentinel3-B, and Cryosat-2. Synthetic satellite tracks are reproduced through the SWOT simulator software (Gaultier et al., 2016), providing realistic measurement errors and noise. Example synthetic satellite tracks covering the CROCO model numerical field are depicted in Figure IV.2 (b). The resulting synthetically observed field is then processed to compute gridded fields with the same interpolation schema that is utilized for the production of gridded SSH satellite data (Taburet et al., 2019). It consists of an inhomogeneous spatiotemporal interpolation between the sampled points by the synthetic tracks, shown in Figure IV.2 (c). The resolution is thus downgraded from 2km of the initial numerical model field to 15km of the OSSE field. A preprocessing is also carried out on the CROCO simulation data to filter large scale, high-frequency signals derived from atmospheric forcing fields (Carrère et al., 2003).

IV.2.3 Satellite Data

By collating measurements made by multiple infrared sensors, high-resolution (1km) super-collated SST maps of the Mediterranean Sea are received from the Copernicus - Marine Environment Monitoring Service (CMEMS), Ultra High Resolution L3S SST Dataset, produced by the CNR - Italy and distributed by CMEMS. The process of supercollation uses SST measurements derived from the LSTR and AVHRR instruments on board Sentinel-3A/-3B and NOAA, VIIRS, MetOp-B, MODIS AQUA and TERRA, and SEVIRI on board the MSG satellite and are representative of nighttime SST values (Nardelli et al., 2013).

IV.3 Methods and Learning

IV.3.1 Standard Eddy Detection

The geostrophic velocity fields are derrived from the SSH fields of the Reference Model simulation and the OSSE altimetric simulation, velocities being proportional to the gradient of the SSH. To represent dynamics on other non-dynamical variables such as SST (and therefore in imagery), we employ a topological proxy of the velocity field, the maximum velocity eddy contour. This contour is defined as the closed isoline around an eddy where its velocity is maximum (Vmax). The plotted contours in this work correspond to the maximum velocity contour. To receive eddy contours and dynamical properties we use in this study the Angular Momentum Eddy Detection and Tracking Algorithm (Le Vu et al., 2018), which is employed on the calculated geostrophic velocity fields.

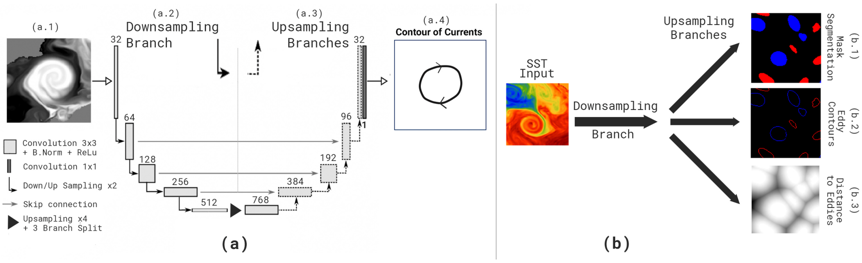

Figure IV.3: Schematic of the Neural Network used for Deep Eddy Scan. (a) The UNet-type architecture learns the mapping of an SST Input (a.1) via a downsampling branch (a.2) and three upsampling branches (a.3) to a dynamical contour (a.4). Skip connections are employed between the downsampling branch and each of the upsampliing branches. (b) The SST Input follows a donwsampling branch then leads to three upsampling branches predicting the (b.1) Mask Segmentation (b.2) Eddy Contours and (b.3) Distance to Eddies.

The identification of potential eddy centers by AMEDA is performed by computing the Local Normalised Angular Momentum (LNAM) (Mkhinini et al., 2014) of the velocity field. Only eddy centers with at least one closed contour of the stream function of the velocity field are retained. A radial profile of the velocity for each detected eddy center is calculated by computing the average velocity and radius at each closed streamline around it:

$$\langle V \rangle = \frac{1}{L_p} \oint \vec{V}\, d\vec{l} \tag{IV.1}$$

where $\vec{V}$ is the local geostrophic velocity field and L_p is the streamline perimeter. The radius R of the characteristic contour is obtained by considering a circular contour of an equivalent area A:

$$\langle R \rangle = \sqrt{\frac{A}{\pi}} \tag{IV.2}$$

The radii considered for sizing the eddies in this study correspond to the radius of the maximum velocity contour. Eddy centers and radius are are important parameters used to retrieve SST patches for training and testing the Neural Network.

IV.3.2 Convolutional Neural Network

We employ a CNN to learn the relation between the SST signature of an eddy (monochromatic image) with a corresponding maximum velocity dynamical contour. We treat this contour detection task, through a semantic segmentation of an image into regions of Anticyclones, Cyclones and No Eddies. Detected contours are subsequently extracted from the labeled regions.
UNET encoder-decoder architectures (Ronneberger et al., 2015) have been

successful in mapping low and high-resolution features of an input image into a ground truth, due to skip connections between the downsampling and upsampling branches. Precisely, they have been successfully employed for the task of eddy detection (Lambhate et al., 2021; Lguensat et al., 2018). Multi-task learning approaches have proven robust on contour detection tasks (Chen et al., 2016; Murugesan et al., 2019; Tan et al., 2018). By using additional output channels and corresponding loss function terms the CNN converges both faster and better to the task of contour detection. We employ an encoder-decoder CNN with one downsampling and three upsampling branches, following Murugesan et al., 2019, each corresponding to a learning task. The encoder-decoder architecture is depicted in Figure IV.3 (a). The first and main learning task consists of learning the filled mask of each eddy, depicted in Figure IV.3 (b.1). The second task consists of learning a contour mask, which consists of the outline of each filled mask with a width of 2 pixels, depicted in Figure IV.3 (b.2). Learning contour masks has been reported to boost the detection of multiple contours in a single window (Chen et al., 2016). A softmax activation is applied on the predictions before the calculation of the loss. For the first and the second task (*T1,T2*) we employ pixel-wise classification loss, for each pixel $\mathbf{x}$ of a matrix:

$$L_{T1,T2} = \sum_{i,j} logp\left(\mathbf{x}_{i,j}; \omega_c c\left(\mathbf{x}_{i,j}\right)\right) \tag{IV.3}$$

where $p\left(\mathbf{x}; l\left(\mathbf{x}\right)\right)$ denotes the probability of predicting a class c between No Eddy, Anticyclone and Cyclone. A class weight ω_c is tuned so that Cyclones weight three times more than Anticyclones and No Eddy classes, as their representations are more complex to learn (see Figure IV.4).

Finally, the third task consists of calculating a distance map, where filled masks containing eddies are labeled as zero and for the non-eddy pixels we calculate the euclidean distance from the closest eddy contour, depicted in Figure IV.3 (b.3). Including a distance map in the multi-task learning has reportedly improved the smoothness of the retained contours, an important factor for realistic eddy detection (Tan et al., 2018). A softmax activation function is performed to clamp the final values between zero and one before the calculation of the loss. For this third task ($T3$) we calculate a pixel-wise MSE loss:

$$L_{T3} = \sum_{i,j} \left(D'\left(\mathbf{x}_{i,j}\right) - D\left(\mathbf{x}_{i,j}\right)\right)^2 \tag{IV.4}$$

where D(x) is the distance map of the ground truth and D'(x) the predicted distance map. The three losses for L_{T1}, L_{T2} and L_{T3} are summed up and weighted with weights $\lambda_{T3} = 3 * \lambda_{T1,2}$, in order to clamp values on the same order of magnitude.

IV.3.3 Patch Creation on the fly

As the sampled domain of the Mediterranean Sea is large relative to the size of the eddies, we retain small windows, cropped randomly during the training process. To increase in the variance of the training samples while gaining in computational efficiency and memory load, we retain patches on the fly, during

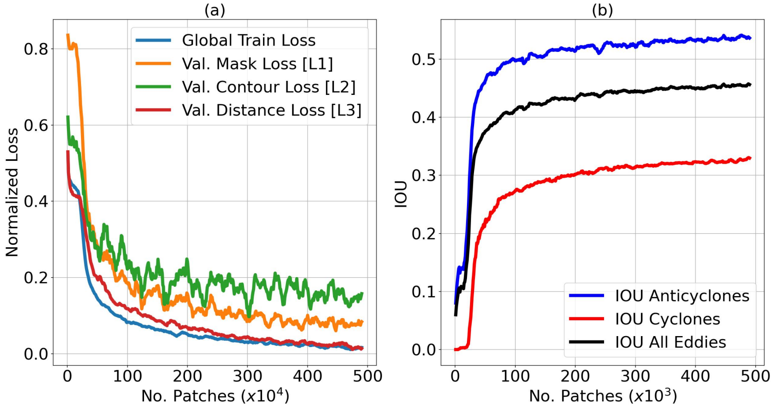

Figure IV.4: (a) Global train and validation losses for the Mask (L_{T1}), Contour (L_{T2}) and Distance (L_{T3}). Loss values are standardized between zero and one. (b) Evolution of the global IOU metric on the validation set. On both x-axes is the number of patches iterated at training.

the training pipeline: First, patches of a size $(\pm 1.5) * 128px$ are cropped in a random location and day, having more than 80% of ocean pixel values. Then, these patches are interpolated to a constant size of 128px. Because of the multi-modality of the distribution of SST pixel values, patches are normalized and a mask containing the location of land values is added as a second input channel. We use one year of numerical model simulation of the Mediterranean sea as train data for the neural network and a second year as test data. This serves to avoid overlap between representations of the same eddy between the train and test datasets, as well as to guarantee a balance between representation of seasonal effects, which can affect significantly the signature of eddies on SST images (Moschos et al., 2022).

IV.3.4 Training and Validation

We use the above framework to generate patches on-the fly as the network is trained. We define an epoch as an iteration of 1,000 training patches generated on the computer memory, passed to the GPU memory via batches of 16. After the end of each epoch, the CNN is validated on a constant set of 1,000 batches, retained by the train test with an equal distribution between seasons. The evolution of the global train loss and the validation losses for the three tasks (equations IV.3 and IV.4) are shown in Figure IV.4 (a).

We define a global validation metric through the Intersection over Union (IoU), else called the Jaccard Index, which evaluates the global accuracy on the form of detected eddies. The IOU is calculated on each pixel-wise segmentation mask

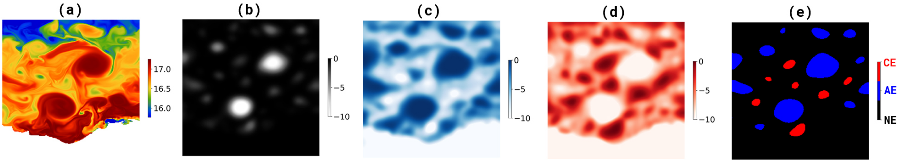

Figure IV.5: (a) An sample SST patch of the test set (size: 256^2 pixels) where the EddyScan CNN is applied. Negative likelihood heatmaps for the (b) No Eddy (c) Anticyclone and (d) Cyclone class. (d) Predicted pixel-wise segmentation mask (Task 1)

(T1) as:

$$IoU\left(R,P\right)=\frac{|R\cap P|}{|R\cup P|} \tag{IV.5}$$

where R is the reference and P is the predicted mask.
Training with 500k patches takes 4 hours on 8GBs of GPU. However, we retained the trained model at 250k patches for regularization as the validation IOU has stopped progressing significantly, reaching also a threshold of $IOU_{AE} > 0.5$ and $IOU_{CE} > 0.3$, as seen in Figure IV.4 (b). The asymmetry between anticyclones and cyclones in the CNN validation can be explained by the more intrinsically complex signatures of cyclones on the SST images as well as their globally smaller size. These effects are linked with the different dynamical structure between anticyclones and cyclones as explained in Stegner et al., 2021.

IV.4 Results and Evaluation

IV.4.1 Performance on Model Data

We first explore the network's performance on the test dataset of the numerical model. An ensemble of 10,000 patches, of a size of 256^2 pixels each, is generated via the random window method from the numerical model simulation on the test year. By applying the EddyScan CNN on each SST patch - Figure IV.5 (a), we retain the heatmaps of the output for task one (see Figure IV.3 (b.1)), for each of the three classes, as seen in Figure IV.5 (b)-(d). Segmentation is performed by retaining the largest value, pixel-wise between the three heatmaps, as depicted in Figure IV.5 (e). On the pixel-wise classified image, we apply a contour detection algorithm to retain the boundaries of every eddy.
Additionally, a simple colocalization schema between predicted and reference eddies is performed on every patch. For each predicted eddy, we search for a barycenter of a reference eddy contour inside the predicted contour. If at least a reference eddy is found, we considered the predicted eddy as correctly detected. In this case, we calculate the position and size errors (see below) between the predicted eddies and all colocalized references and we match it with the one that is closest in position and size. If a predicted eddy has no colocalized reference

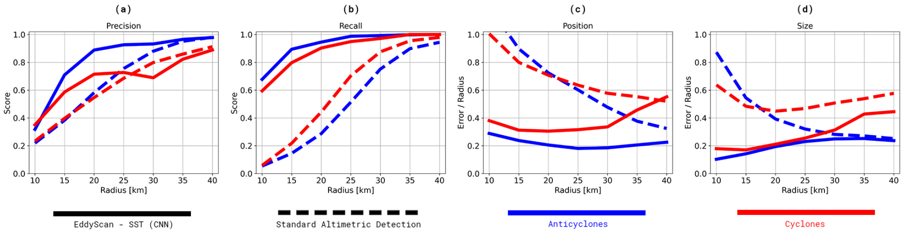

Figure IV.6: Performance indicators: (a) Precision (1-Ghost Rate) and (b) Recall (1 - Missed Rate). (c) Position (barycenter) and (d) Size (radius) mean errors normalized by the reference radius. Straight (dashed) lines correspond to the performance of the EddyScan-SST CNN (Standard Altimetric Detection). Blue (red) lines correspond to performance for anticyclones (cyclones).

eddy it is considered a *Ghost*. Finally, the eddy contours of the references which correspond to no predictions are named *Missed*.
As the eddy detection task is an object detection with underlying physical properties, we define relevant metrics to evaluate the performance of the CNN:

- An overall Precision and Recall metric.
- A metric on the error on the position of each eddy detection.
- A metric on the error of the size of each eddy detection.

The precision and recall scores are defined as:

$$\begin{aligned} Precision(c) &= \frac{|R_{i,c} \cap P_{i,c}|}{|P_{i,c}|} \\ Recall(c) &= \frac{|R_{i,c} \cap P_{i,c}|}{|P_{i,c}|} \end{aligned} \tag{IV.6}$$

The scores are calculated for each eddy object i and for each eddy class c, i.e. Anticyclones or Cyclones. $R_{i,c}$ and $P_{i,c}$ denote, respectively, reference and predicted eddies of each class. Through these metrics, we define the Ghost eddy rate, i.e. false positive detections $Ghost(c) = 1 - Precision(c)$ and the Missed Eddy rate i.e. false negative detections as $Missed(c) = 1 - Recall(c)$.
The precision and recall scores are shown in Figure IV.6 (a) and (b) respectively. We compare the scores of the Eddy Scan CNN, applied on SST images, with those of the Standard Eddy Detection applied on simulated altimetry fields. The latter, are received through an OSSE (see Figure IV.2) and our standard eddy detection experiment corresponds to those described by Amores et al., 2018 and Stegner et al., 2021. The EddyScan CNN generally outperforms the standard eddy detection, as the eddy signatures on the SST are much closer to the reference dynamical field than those found in altimetric observations (Figure V.1). The precision for Anticyclones is constantly higher for all eddy sizes, while

cyclones have a lower ghost rate for radii up to 25km. On the recall metric, the CNN greatly outperforms standard eddy detection both on the mesoscale and submesoscale detections. For instance, the CNN missed rate 30% (40%) for small submesoscale Anticyclones (Cyclones) compared with 90% of missed small eddies by standard detection, due to the low resolution of the altimetry fields (Amores et al., 2018). For large, mesoscale eddies with radii bigger than 25km, the CNN has a miss rate lower than 5% (10%) for Anticyclones (Cyclones). It is noted that the missed rate shown for the Standard Eddy Detection for large cyclones is overestimated: due to the colocalization schema followed, large cyclones of the altimetry corresponding to multiple smaller reference detections, are falsely labelled as correctly detected. This is portrayed in the increased error in size estimation for large cyclones in Figure IV.6 (d).

We additionally quantify the error in the position and size of the correctly detected eddies. For the position error we consider the distance between the barycenters of two colocalized eddy contours, normalized by the radius of the reference eddy contour:

$$E_{pos} = \frac{\sqrt{(x^{bar}_{pred} - x^{bar}_{ref})^2 + (y^{bar}_{pred} - y^{bar}_{ref})^2}}{r_{ref}} \tag{IV.7}$$

For the size error we consider the difference between the radii of the two colocalized eddy contours, normalized by the radius of the reference eddy contour:

$$E_{size} = \frac{|r_{pred} - r_{ref}|}{r_{ref}} \tag{IV.8}$$

The mean errors, over all correctly detected eddies, on the position and the size are plotted in Figure IV.6 for both the EddyScan CNN and the Standard Altimetric Detection. On average, the EddyScan has an error of 20% of the radius when determining the center of an anticyclone, with an error of $30 - 50\%$ for cyclones. Due to the degradation of the altimetry fields, the positioning of small eddies by standard methods reaches up to one radius of error. Size error for anticyclones does not exceed 20% for all sizes while the size of big cyclones tends to be underestimated by the CNN. In both cases, the EddyScan-SST outperforms the altimetric methods. Here again, cyclones prove more difficult to detect than their anticyclonic counterparts, due to their complex signatures, as discussed before.

IV.4.2 Performance on Satellite Data

The EddyScan-SST serves as an operational oceanographic module, thus needing to be applied and evaluated on satellite observations of the ocean. In particular, infrared imagery is a proxy to obtain observations of the SST, which contains representations common to those learned by the CNN. However, the satellite data possesses some key differences from the numerical model data:

- The impact of noisy labels: As the altimetric observations of eddies are often of low reliability, it is impossible to establish with certainty the link between a dynamic contour (altimetry) and the satellite observation of

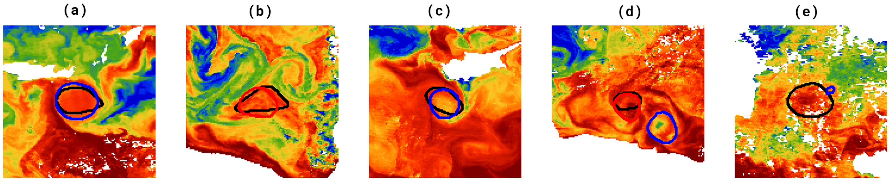

Figure IV.7: Samples from the Eddy Infrared Satellite Observations dataset released with this paper. Handlabeled contours are plotted with black. Predictions of the EddyScan CNN are plotted with blue for anticyclones and red for cyclones. Cases (a)-(c) portay coherent well-detected eddies. Case (d) portrays a typical structure of a Cyclone-Anticyclone dipole. Case (e) shows the impact of cloud coverage that can hinder prediction.

the surface temperature. Therefore there is a need for a transfer learning schema, using representations from models to train a CNN which will be applied to satellite data.

- The impact of cloud coverage: Infrared radiation cannot penetrate clouds, leading to a constant corruption of the observation either by scattered missing values or even completely covered chunks of the ocean. Furthermore, cloud presence corrupts the observed values of nearby pixels, creating noise in the data. Even though cloud coverage is out of the scope of this study, it has been demonstrated in Moschos et al., 2020a that CNNs can classify eddy signatures on the SST even when impacted by strong local cloud coverage of up to 80% .

- The need for hand labeling: stemming from the noisy label problem. As such we have retained 500 patches, each one containing the ground truth of the dynamical contour of an Anticyclone (428 patches) or a Cyclone (72 patches). These patches are provided to the community with this paper and are used to evaluate the performance of the EddyScan on infrared observations.

In Figure IV.7 we depict several examples of eddy signatures found on infrared images: anticyclones and cyclones can have a coherent warm or cold anomaly in their cores depending on the season, as seen in panels (a)-(c). A typical case that arises is a dipole structure, featuring an anticyclone rotating near a cyclone and constituting a dynamic ensemble. These pairs are often hard to detect on altimetry, as they are often formed by relatively small eddies, and have many times intense signatures on the SST such as the one seen in panel (d). Finally, as discussed, cloud coverage can hinder EddyScan prediction as seen in panel (e), which is why we have limited the maximum cloud coverage per patch at 10% for this dataset.

	ALL	AE	CE
IOU (eq. IV.5)	0.46	0.48	0.28
Miss Rate (eq. IV.6)	0.21	0.19	0.35
Position Error (eq. IV.7)	0.33	0.30	0.54
Size Error (eq. IV.8)	0.23	0.22	0.35

Table IV.1: EddyScan-SST performance on the hand labeled set of 500 satellite infrared images.

Applying the EddyScan on the 500 patches retained, we receive the metric scores presented in Table IV.1. The overall IOU is calculated between the reference eddy and the corresponding predicted contour. All secondary contours are filtered out. The miss rate expresses how many of the patches had no CNN detection over the reference contour. The position error (equation IV.7), and the size error (equation IV.8) are expressed as a percentage of the radius of the reference contour. As with the numerical model data, performance on Anticyclones is significantly better than that on Cyclones. Cyclones tend to be much smaller, and with more complex signatures, pinpointing the need for an additional finetuning of the CNN using infrared images of cyclones.

IV.5 Conclusion

In this work, we employ computer vision to perform eddy detection on infrared satellite imagery, surpassing the limitations of standard eddy detection methods on altimetry. Our CNN trained on patches of SST from a simulation of a high-resolution ocean numerical models, achieves important performance scores on the task of eddy detection with a global IOU of 0.45 and a Miss Rate from $0 - 20\%$ for mesoscale eddies and 15%-40% for small and submesoscale eddies ($< 15km$). To compare the performance of the CNN with standard detection methods we perform a simulation of the satellite altimetry observation on numerical model fields. Standard detection methods have a miss rate of $10 - 80\%$ for mesoscale eddies, while missing completely the small and submesoscale due to the uncertainty and low resolution of altimetry data. Albeit being powerful tools, Neural Networks will only perform as good as the underlying data allows, making a training on altimetric data bound by its noisy labels.

High-resolution satellite imagery, such as infrared measurements, remains largely unused for ocean structure detection, despite the rich amount of information contained in patterns of gradients, swirls and filaments. These measurements, although affected by cloud coverage have a very high global repeat period due to the many infrared sensors launched on satellites. To extract the dynamical information from these complex representations in infrared imagery we utilize the topological information of eddy contours as a proxy of the surface dynamics of the ocean. Our method does not replace, but rather compliments standard eddy detection on altimetry, especially on periods and regions not covered by altimeter satellites, while also providing a reliability index.

We employ a transfer learning schema, using ground truth from a high-resolution numerical model simulation of the ocean, with an almost perfect link between dynamics and temperature signature, applying afterwards the trained network on satellite observations. This way we avoid the noisy labeling of satellite data and the tedious hand labeling process. We treat the contour detection task as a multi-task learning aids in order to retain better information on the contours size, position and form. Finally, the CNN is invariant of the input size, meaning that it can be applied in any region of the world, given enough computational resources.

The trained eddy-detecting neural network proves functional on infrared satellite imagery with a 20% miss rate of eddies and a mean error of 23% on their size and 33% on their position. We release a hand-labeled dataset containing eddy signatures on infrared observations along with their dynamical contours, for use by the oceanographic and vision communities.

Including multi-modal satellite data such as satellite observations on the visible spectrum and synthetic aperture radar (Du et al., 2019; Lambhate et al., 2021) as well as finetuning the neural network for cloud coverage (Moschos et al., 2020a) can boost the operational performance of the EddyScan module. Employing semi-supervised learning (Sohn et al., 2020) can allow for the extraction of accurate information on eddies in noisy-labeled satellite data. Furthermore, super-resolution neural networks, resampling the velocity fields in high resolution by fusing satellite altimetry and infrared imagery (Buongiorno Nardelli et al., 2022) could work in conjunction with the eddy detection neural networks.

Precise and reliable eddy detection allows us to estimate, in real-time, the local hydrographic properties and the surface circulation in a given region, providing key information for many applications of maritime stakeholders.

References

Amores, A. et al. (2018). “Up to what extent can we characterize ocean eddies using present-day gridded altimetric products?” In: *Journal of Geophysical Research: Oceans* vol. 123, no. 10, pp. 7220–7236.

Buongiorno Nardelli, B. et al. (2022). “Super-Resolving Ocean Dynamics from Space with Computer Vision Algorithms”. In: *Remote Sensing* vol. 14, no. 5, p. 1159.

Carrère, L. and Lyard, F. (2003). “Modeling the barotropic response of the global ocean to atmospheric wind and pressure forcing-comparisons with observations (DOI 10.1029/2002GL016473)”. In: *Geophysical Research Letters* vol. 30, no. 6, pp. 8–8.

Chelton, D. B., Schlax, M. G., and Samelson, R. M. (2011a). “Global observations of nonlinear mesoscale eddies”. In: *Progress in oceanography* vol. 91, no. 2, pp. 167–216.

Chelton, D. B. et al. (2011b). “The influence of nonlinear mesoscale eddies on near-surface oceanic chlorophyll”. In: *Science* vol. 334, no. 6054, pp. 328–332.

Chen, H. et al. (2016). “DCAN: deep contour-aware networks for accurate gland segmentation”. In: *Proceedings of the IEEE conference on Computer Vision and Pattern Recognition*, pp. 2487–2496.

Dong, C. et al. (2014). “Global heat and salt transports by eddy movement”. In: *Nature communications* vol. 5, no. 1, pp. 1–6.

Du, Y. et al. (2019). “Deep learning with multi-scale feature fusion in remote sensing for automatic oceanic eddy detection”. In: *Information Fusion* vol. 49, pp. 89–99.

Duo, Z., Wang, W., and Wang, H. (2019). “Oceanic mesoscale eddy detection method based on deep learning”. In: *Remote Sensing* vol. 11, no. 16, p. 1921.

Franz, K. et al. (2018). “Ocean eddy identification and tracking using neural networks”. In: *IGARSS 2018-2018 IEEE International Geoscience and Remote Sensing Symposium*. IEEE, pp. 6887–6890.

Gaultier, L., Ubelmann, C., and Fu, L.-L. (2016). “The challenge of using future SWOT data for oceanic field reconstruction”. In: *Journal of Atmospheric and Oceanic Technology* vol. 33, no. 1, pp. 119–126.

Gill, A., Green, J., and Simmons, A. (1974). “Energy partition in the large-scale ocean circulation and the production of mid-ocean eddies”. In: *Deep sea research and oceanographic abstracts*. Vol. 21. 7. Elsevier, pp. 499–528.

Holloway, G. (1986). “Estimation of oceanic eddy transports from satellite altimetry”. In: *Nature* vol. 323, no. 6085, pp. 243–244.

Isern-Fontanet, J., Garcıa-Ladona, E., and Font, J. (2003). “Identification of marine eddies from altimetric maps”. In: *Journal of Atmospheric and Oceanic Technology* vol. 20, no. 5, pp. 772–778.

Lambhate, D. et al. (2021). “W-Net: A Deep Network for Simultaneous Identification of Gulf Stream and Rings From Concurrent Satellite Images of Sea Surface Temperature and Height”. In: *IEEE Transactions on Geoscience and Remote Sensing* vol. 60, pp. 1–13.

Le Vu, B., Stegner, A., and Arsouze, T. (2018). “Angular Momentum Eddy Detection and tracking Algorithm (AMEDA) and its application to coastal eddy formation”. In: *Journal of Atmospheric and Oceanic Technology* vol. 35, no. 4, pp. 739–762.

Lguensat, R. et al. (2018). “EddyNet: A deep neural network for pixel-wise classification of oceanic eddies”. In: *IGARSS 2018-2018 IEEE International Geoscience and Remote Sensing Symposium*. IEEE, pp. 1764–1767.

Liu, Y., Zheng, Q., and Li, X. (2021). “Characteristics of Global Ocean Abnormal Mesoscale Eddies Derived From the Fusion of Sea Surface Height and Temperature Data by Deep Learning”. In: *Geophysical Research Letters* vol. 48, no. 17, e2021GL094772.

Lobel, P. and Robinson, A. (1986). “Transport and entrapment of fish larvae by ocean mesoscale eddies and currents in Hawaiian waters”. In: *Deep Sea Research Part A. Oceanographic Research Papers* vol. 33, no. 4, pp. 483–500.

Mason, E., Pascual, A., and McWilliams, J. C. (2014). “A new sea surface height–based code for oceanic mesoscale eddy tracking”. In: *Journal of Atmospheric and Oceanic Technology* vol. 31, no. 5, pp. 1181–1188.

Mkhinini, N. et al. (2014). “Long-lived mesoscale eddies in the eastern Mediterranean Sea: Analysis of 20 years of AVISO geostrophic velocities”. In: *Journal of Geophysical Research: Oceans* vol. 119, no. 12, pp. 8603–8626.

Moschos, E., Barboni, A., and Stegner, A. (2022). “Why do inverse eddy surface temperature anomalies emerge? The case of the Mediterranean Sea”. In: *Remote Sensing* vol. 14, no. 15, p. 3807.

Moschos, E. et al. (2020a). “Classification of eddy sea surface temperature signatures under cloud coverage”. In: *IEEE Journal of Selected Topics in Applied Earth Observations and Remote Sensing* vol. 13, pp. 3437–3447.

Moschos, E. et al. (2020b). “DEEP-SST-EDDIES: A Deep Learning framework to detect oceanic eddies in Sea Surface Temperature images”. In: *ICASSP 2020-2020 IEEE International Conference on Acoustics, Speech and Signal Processing (ICASSP)*. IEEE, pp. 4307–4311.

Murugesan, B. et al. (2019). “Psi-Net: Shape and boundary aware joint multi-task deep network for medical image segmentation”. In: *2019 41st Annual International Conference of the IEEE Engineering in Medicine and Biology Society (EMBC)*. IEEE, pp. 7223–7226.

Nardelli, B. B. et al. (2013). “High and Ultra-High resolution processing of satellite Sea Surface Temperature data over Southern European Seas in the framework of MyOcean project”. In: *Remote Sensing of Environment* vol. 129, pp. 1–16.

Nencioli, F. et al. (2010). “A vector geometry–based eddy detection algorithm and its application to a high-resolution numerical model product and high-frequency radar surface velocities in the Southern California Bight”. In: *Journal of atmospheric and oceanic technology* vol. 27, no. 3, pp. 564–579.

Pegliasco, C. et al. (2022). “META3. 1exp: a new global mesoscale eddy trajectory atlas derived from altimetry”. In: *Earth System Science Data* vol. 14, no. 3, pp. 1087–1107.

Ronneberger, O., Fischer, P., and Brox, T. (2015). “U-net: Convolutional networks for biomedical image segmentation”. In: *International Conference on Medical image computing and computer-assisted intervention*. Springer, pp. 234–241.

Sohn, K. et al. (2020). “A simple semi-supervised learning framework for object detection”. In: *arXiv preprint arXiv:2005.04757*.

Stegner, A. et al. (2021). “Cyclone-Anticyclone Asymmetry of Eddy Detection on Gridded Altimetry Product in the Mediterranean Sea”. In: *Journal of Geophysical Research: Oceans* vol. 126, no. 9, e2021JC017475.

Taburet, G. et al. (2019). “DUACS DT2018: 25 years of reprocessed sea level altimetry products”. In: *Ocean Science* vol. 15, no. 5, pp. 1207–1224.

Tan, C. et al. (2018). “Deep multi-task and task-specific feature learning network for robust shape preserved organ segmentation”. In: *2018 IEEE 15th International Symposium on Biomedical Imaging (ISBI 2018)*. IEEE, pp. 1221–1224.

Zhang, Z., Wang, W., and Qiu, B. (2014). “Oceanic mass transport by mesoscale eddies”. In: *Science* vol. 345, no. 6194, pp. 322–324.

Paper V

Real-time Validation of Operational Ocean Models via eddy-detecting deep neural networks

Evangelos Moschos, Alexandre Stegner, Briac Le Vu, Olivier Schwander

Published in *International Geoscience and Remote Sensing Symposium (IGARSS 2022)*, July 2022 pp. 8008-8011. DOI: 10.1109/IGARSS46834.2022.9883253..

Abstract

Surface currents provided, in real time, by operational ocean models often differ from each other but also from satellite altimetry observations, especially in terms of mesoscale dynamics. Eddies, which play a dominant role on circulation at the regional scale, have a signature on both altimetry maps and satellite imagery, such as sea surface temperature. Combining these independent signatures allows for a highly reliable detection of reference eddies. To this end, we build a convolutional neural network capable of detecting the contours of mesoscale eddies on SST maps in real time. Combined with a standard eddy detection algorithm applied to altimetry maps, we were able to locate and identify with high accuracy more than 900 eddies, in the Mediterranean Sea, over a period of 6 months, and use them as a reference for numerical model validation. We compare as a case study the performance of two operational models: MERCATOR and MFS.

V.1 Introduction

Operational ocean numerical models simulate, in real-time, the physical state and the dynamical properties of oceans, forecasting also their future state. Validation of ocean models consists of a quality assessment of their operational output. The quantification of model error is performed by comparing model outputs with observations, from satellite or in-situ source.

Assimilation of numerical models, seeks to integrate these observations to produce an optimal estimate of the evolving state of the system. The mesoscale dynamics, partially observed through different measured variables, can be thus assimilated

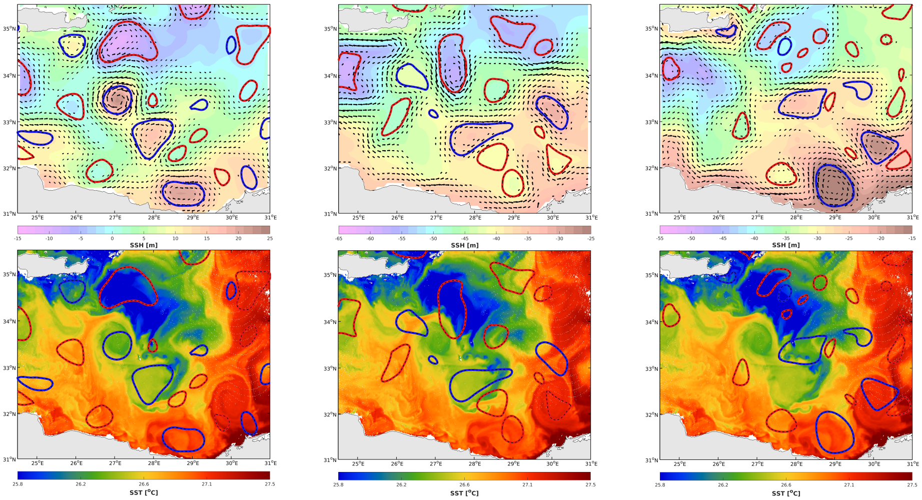

(a) AVISO (Satellite) (b) MERCATOR (Model) (c) MFS (Model)

Figure V.1: Comparison of satellite altimetry (a) and two numerical models (b,c) on the eastern Mediterranean sea on the 22/08/2021. Sea Surface Height (SSH) obtained by the models and observed by satellite correspondingly is shown on the topmost panels along with the derrived geostrophic velocity vectors. The eddy contours (blue=anticyclonic, red=cyclonic) detected by AMEDA on each field are superimposed on the SSH panels. The bottom panels all show the Sea Surface Temperature (SST) measured by satellite on the same day, on which the aforementioned eddy contours corresponding to each SSH output are superimposed.

by the numerical model. Albeit the important improvements brought by data assimilation methods, the results of different operational models in the same period and region can vary significantly on the level of mesoscale dynamics.

Eddies are coherent structures, that can survive several weeks or months, with a prevalent role at mesoscale or submesoscale ocean circulation. These structures can have a signature on satellite observations such as altimetry, but also on visible imagery or synthetic aperture radar. Many algorithms use geometrical properties of the Sea Surface Height (SSH) field and/or the streamlines of the derived velocity field to detect and track in time vortex structures. However, standard altimetry (AVISO/DUACS) products contain large uncertainties due to the spatio-temporal interpolation between satellite tracks, limiting the reliability of these algorithms (Stegner et al., 2021).

Satellite imagery provides independent observations of mesoscale structures. In spite its high resolution, their patterns are too complex for standard geometric methods to process. Besides, Convolutional Neural Networks (CNNs) with deep architectures have proven very efficient in detecting eddy signatures on visible imagery such as Sea Surface Temperature (Moschos et al., 2020a), marking the

potential of Deep Learning methods for this task.
We present a novel methodology which employs an Eddy-Detecting Convolutional Neural Network on SST maps, combined with an Altimetric Eddy Tracking Algorithm to provide a set of highly reliable eddy detections. These reference detections are used to validate the operational output of different numerical models and serve as a basis for an operator to pick-and-choose between different models on a certain region.

V.2 Satellite and Model Data

Working on the Mediterranean Sea as a case study, we use near real-time altimetry and SST satellite data to validate the real-time output of two operational numerical ocean models: MERCATOR and MFS.
Daily, 1/120°resolution, multi-sensor SST maps of the Mediterranean Sea are received from the CMEMS Ultra High Resolution L3S SST Dataset and are representative of night time SST. We also utilize daily SSH and derived geostrophic velocity fields from AVISO/DUACS altimetry products at 1/8°resolution from the CMEMS L4 Sea Level dataset.
To retrieve the eddy centers, their corresponding contours and dynamical properties we use the AMEDA algorithm (Le Vu et al., 2018) applied on the geostrophic velocity field. Daily eddy contours derived from the geometrical and dynamical properties of the velocity field are then integrated into eddy tracks which follow the lifetime of an eddy. The contours shown in this work correspond to the closed streamline of maximum velocity of the eddy.
Two operational models are considered in this study. The Operational Mercator global ocean analysis and forecast system (MERCATOR) is routinely operated in real time since early 2001 and updated daily (Lellouche et al., 2018). The Mediterranean Forecasting System (MFS) is a second operational model providing nowcasting and forecasting specific to the Mediterranean Sea dynamics (Med-Currents) (Coppini et al., 2021). Both models run on a rectangular grid with unevenly spaced vertical levels and use data assimilation schemes: reduced-order Kalman filter for the MERCATOR and 3DVAR for MFS. Table V.1 summarizes the differences in the parameters of the two operational models. The nowcast output of these models was downloaded in real-time from the CMEMS database.

Model	Resolution		Assimilation		
	Horiz.	Vert.Lev.	In-Situ	SSH	SST
MERCATOR	1/12°	50	✓	✓	✓
MFS	1/24°	141	✓	✓	

Table V.1: Main properties of the two operational models

In Figure V.1 the real-time data available from the MERCATOR Model, the MFS Model and Satellite Altimetry are compared on a certain day (22/08/2021) in the Eastern Mediterranean Sea region. The difference between the eddy contours obtained through the geostrophic velocity field of the two models and the observations are evident. Through SST images, an independent validation of the eddy position can be performed (Figure V.1 bottom panels). Both models seem to miss many eddies with a signature on SST, while even the eddy contours from the best performing AVISO fields on Figure V.1 (a) are not aligned with the SST gradients.

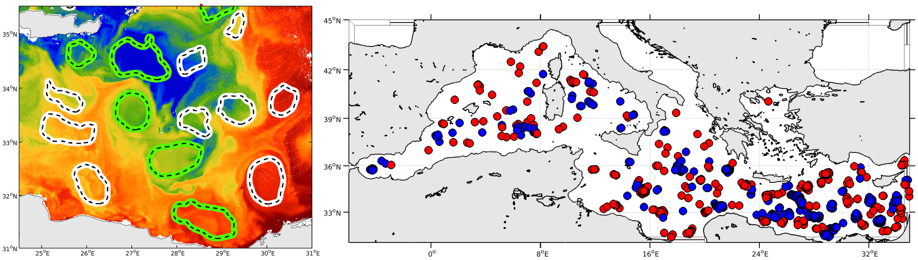

(a) Example on 22/08/2021

(b) Reference eddies (900) in Feb-Aug 2021

Figure V.2: CNN Reference Eddies: (a) An example of CNN eddy detection on the SST on the 22/08/2021. White contours are CNN detections on the SST with no corresponding SSH AMEDA detection. Green contours are CNN detections with an overlapping SSH detection (criterion V.1), and retained as reference eddies (b) Positions of 600 anticyclonic (blue dots) and 300 cyclonic (red dots) reference eddies retained on February-August 2021.

V.3 Eddy-Detecting CNN on SST Images

Convolutional Neural Networks (CNNs) have been successfully put to test on the task of eddy detection which consists of a semantic segmantation task (Lguensat et al., 2018). However, most of the methods in the bibliography train and evaluate the performance of these CNNs on satellite altimetry data (SSH) which contain inherent uncertainty biases. Thus, the best of CNNs trained this way will only manage to replicate the best of the standard eddy detection models.

In this work, we introduce a CNN able to detect the position, size and form of eddies via a contour, on Sea Surface Temperature (SST) images. To perform this semantic segmentation task, we construct a U-Net type architecture with an upsampling and a downsampling branch composed by convolution and pooling operations. A dataset of more than 100,000 distinct eddy signatures on SST images are used to train the network by minimizing cross entropy loss on masks stemming from the contours of maximal velocity (obtained by AMEDA). The training is performed on an GPU card with 24 GB of memory, with a batch size of 32 images.

To evaluate the performance of the trained CNN we use a sample of 30,000 SST patches retained on distinct years from the ones used for training. Our test is performed on mesoscale eddies with radii larger than 20km and with a cloud coverage in the patch of less than 10 %. A comparison between the performance of the eddy-detecting CNN applied on SST images and that of standard detection methods applied on the geostrophic field derived by the SSH (as described in Stegner et al., 2021) is given in Table V.2. The Neural Network on SST overperforms standard detection on SSH both by a much lower Missed Eddies and Ghost (False Positive) Rate but also through the precision on the position and the size of detect eddies. This difference is even more pronounced for cyclonic eddies, for which altimetry detection does not prove robust (Stegner et al., 2021).

Method / Data	Miss	Ghost	Position	Size
Standard / SSH	34 %	10 %	7-20 km	15-50 %
CNN / SST	3 %	<1 %	7km	20%

Table V.2: Error comparison on SSH and SST detection

V.4 Reference Eddies

Detections on SSH derived products (velocity) by the AMEDA are combined with the detections on the SST images by the Convolutional Neural Network (CNN). We define the agreement of the two detections on independent satellite observations with a simple Intersection over Union (IoU) threshold:

$$\frac{SSH \cap SST}{SSH \cup SST} > 0.5 \tag{V.1}$$

The outputs of the eddy detecting CNN on the SST are shown on Figure V.2 (a). SST detections with no corresponding AMEDA detection on the SSH are shown with a white contour. SST detections with an overlapping SSH detection above the IoU threshold of criterion V.1 are shown with a green contour and are retained as reference eddies. A total of 900 reference eddies shown in Figure V.2 (b), of which 600 anticyclones and 300 cyclones, were retained in real-time on the February-August 2021 by applying the CNN and AMEDA detection tools, spanning all the Mediterranean sea.

V.5 Model Validation

The reference eddies, cross-detected in real-time on both SSH and SST observations, serve to validate the accurate reproduction of mesoscale dynamics of operational models in real-time. To retrieve the numerical model eddy contours we apply the AMEDA algorithm to the geostrophic velocity derived from the operational model in real time. As seen in Figure V.1 (b) and (c), the MERCATOR and MFS model show diverging results on the mesoscale field.
To apply our validation scheme we search for a corresponding numerical model contour for each reference eddy contour. To perform a colocalization the distance of the barycenters of the two contours should not be bigger than the sum of their

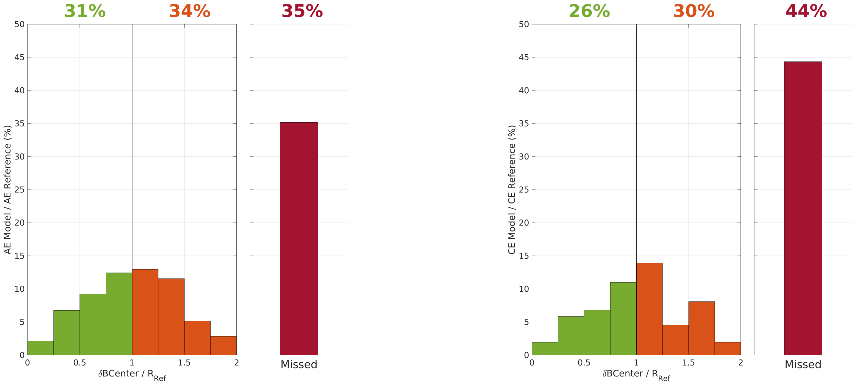

(a) MERCATOR (AE) (b) MERCATOR (CE)

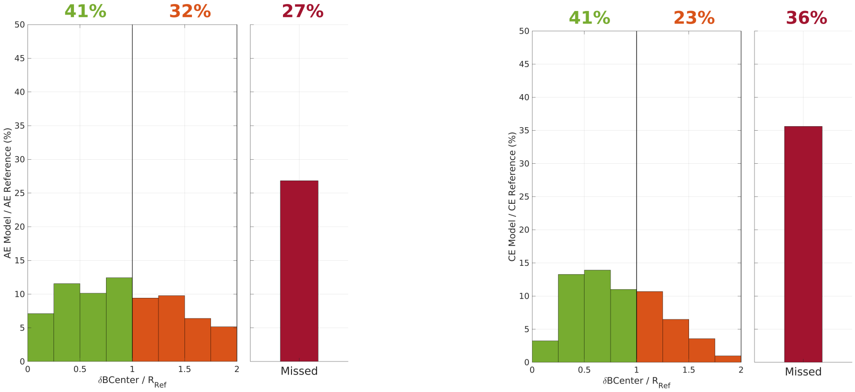

(c) MFS (AE) (d) MFS (CE)

Figure V.3: Validation of two numerical models on the accuracy of reproduction of anticyclonic (AE) and cyclonic (CE) eddies. Green bins show accurately detected eddies, orange bins show erroneously detected eddies and red bins show missed eddies.

radii, i.e. the equivalent surface circles of their contours should not intersect:

$$d_{bar}^{(Ref,Mod)} < R_{Ref} + R_{Mod} \tag{V.2}$$

If a contour is colocalized, the distance $d_{bar}^{(Ref,Mod)}$ normalized by the reference eddy radius R_{Ref} represents its positioning error, plotted on the x axes of Figure V.3. When this error is smaller than one reference radius (R_{Ref}) then the eddy is considered as accurately detected (green bins). When the error is between the reference radius (R_{Ref}) and the diameter ($2R_{Ref}$) the eddy is considered as erroneously detected (orange bins). If no model contour in the vicinity of the

reference contour surpasses the criterion V.2, then the eddy is characterized as "missed" by the model.
As seen in Figure V.2, the MFS model outperforms the Mercator model with a 41% of accurate detections both for AE and CE. However both models have a high miss rate of about a third or more of the eddies, higher for CE than AE and another third which is erroneously detected.

V.6 Conclusion

Operational oceanic model nowcast errors on mesoscale dynamics can be important, despite the assimilation of observations. Here, we propose a novel scheme to validate operational models in real-time. The eddy detections of a Convolutional Neural Network on SST satellite maps are coupled with those of standard methods on SSH maps to provide a sub set of highly reliable reference eddies. The later are then used to quantify, in real time, the accuracy of different operational models in the Mediterranean Sea.
Our CNN detecting eddies on SST images has a very low false negative (3%) and false positive ($< 1\%$) rate compared that of standard detection methods. CNNs have proven robust in processing cloud coverage (Moschos et al., 2020b), and can be thus trained to provide with reference eddy detections when the local region is covered with less than $< 50\%$ of clouds. Besides, the inclusion of other visible (CHL) or radar (SAR) observations could significantly increase the number of reference eddies. Harnessing data fusion and deep neural networks to validate operational ocean models can provide maritime stakeholders with reliable and accurate nowcast and forecast data.

References

Coppini, G. et al. (2021). “The Copernicus Marine Service ocean forecasting system for the Mediterranean Sea”. In: *9th EuroGOOS International conference.*

Le Vu, B., Stegner, A., and Arsouze, T. (2018). “Angular Momentum Eddy Detection and tracking Algorithm (AMEDA) and its application to coastal eddy formation”. In: *Journal of Atmospheric and Oceanic Technology* vol. 35, no. 4, pp. 739–762.

Lellouche, J.-M. et al. (2018). “Mercator Ocean Global High-Resolution Monitoring and Forecasting System”. In: *New Frontiers in Operational Oceanography*, pp. 563–592.

Lguensat, R. et al. (2018). “EddyNet: A deep neural network for pixel-wise classification of oceanic eddies”. In: *IGARSS 2018-2018 IEEE International Geoscience and Remote Sensing Symposium.* IEEE, pp. 1764–1767.

Moschos, E. et al. (2020a). “Deep-SST-Eddies: A Deep Learning Framework to Detect Oceanic Eddies in Sea Surface Temperature Images”. In: *IEEE ICASSP*, pp. 4307–4311.

Moschos, E. et al. (2020b). “Classification of eddy sea surface temperature signatures under cloud coverage”. In: *IEEE Journal of Selected Topics in Applied Earth Observations and Remote Sensing* vol. 13, pp. 3437–3447.

Stegner, A. et al. (2021). “Cyclone-Anticyclone Asymmetry of Eddy Detection on Gridded Altimetry Product in the Mediterranean Sea”. In: *Journal of Geophysical Research: Oceans* vol. 126, no. 9, e2021JC017475.

Conclusion

Concluding Remarks

On the presented papers

We have presented a body of work centered around the signatures of mesoscale eddies on infrared (SST) images, composed of five publications. Our main objective, that of eddy detection on infrared imagery, was presented at different steps of its maturation through Paper II, Paper III and Paper IV. We have also expanded our work in complementary directions, providing a physical study of the anomalies of mesoscale eddies on Sea Surface Temperature in Paper I as well as an application of the eddy detection algorithm we built, in order to validate operational ocean numerical models in Paper V.

Considering the eddy detection on infrared imagery, we are the first to propose a method performing independently on SST data, able to provide a proxy of the dynamical contour in real-time. Our method significantly outperforms standard altimetric eddy detection with up to 30% improvement in missed rates and up to 60% improvement in ghost eddy rates, depending on the type and size of eddies (see Paper IV, Figure 6), while additionally improving in the errors in the position and sizes of the detected eddies. Operationally wise, a pipeline of real-time application of the trained Neural Network on infrared satellite observations has been set up, visualizing the results through the SeaScope open-source software developped by OceanData lab. The real-time application of our module has very low computational costs, as our method requires very short processing times on the orders of seconds per daily satellite image. We also have demonstrated that cloud coverage on infrared imagery can be robustly treated up to levels of 50% (see

As developed in the introduction, many works have been published recently, employing Machine Learning and CNNs for the task of eddy detection. The vast majority of these publications build and apply their networks on altimetric data, which contain large amounts of uncertainty due to their spatio-temporal interpolation scheme. Thus, the best Machine Learning approaches on altimetry will only emulate the best of the standard altimetric eddy detection methods, on which they are trained. This is why, in our work, we develop Machine Learning methods working independently on satellite imagery, which contains high-resolution signatures of eddies and virtually no uncertainty when free of cloud coverage. Our CNN, detecting eddies on infrared imagery, is not antagonistic with altimetric eddy detection but rather, the two methods can act in synergy.

We showcase the synergy between standard altimetric eddy detection methods and our CNN-based method on infrared imagery via an application of operational oceanographic model validation presented in Paper V. To build a dataset of reference eddy detections, we characterize the reliability of detections as *strong* when an equivalent detection is performed on both altimetry and infrared imagery, *good* when it is performed only on infrared imagery, and *standard* when it is performed only on altimetry. In this fashion, we utilize the agreement between independent sensors to create a reliability metric of eddy detections. Through these reference dynamical contours, which act as a proxy of the velocity field, we then intercompare the outputs of different operational oceanographic models, on their ability to correctly reproduce eddies, and thus the mesoscale dynamics of the ocean. In a case study in the Mediterranean Sea, we intercompare in Paper V the outputs of the MERCATOR and MFS operational assimilated models, in a common time period, finding that the latter outperforms the former. The proposed method provides a large number of reference objects that can be used to validate, but also intercompare operational models, with a great addition of references to the currently available, costly in-situ measurements. Our application is also generalizable in any time period or region of the globe.

Finally, in Paper I we add a physical comprehension element to our body of work, by performing a characterization of the anomalies of mesoscale eddies, found in the infrared imagery datasets originally extracted for the purposes of Machine Learning. We specifically explore the emergence of inverse eddy anomalies on the Sea Surface Temperature, that is Cold-Core Anticyclones and Warm-Core Cyclones. We find that a peak of 70% of inverse anomalies is reached in May and June for both Anticyclones and Cyclones. We subsequently show through observations that the inversion of eddy surface temperature anomalies is seasonal and that their cycle corresponds with the evolution of the Mixed Layer Depth during the winter mixing and spring-summer restratification periods. Additionally, we show that this inversion between Warm and Cold Core regimes can happen several times during the lifetime of an individual long-lived mesoscale eddy. However, using vertical profiles obtained through argo floats we find that the inversion of the temperature anomalies, only occurs on the first 50 meters of the ocean layer. Finally, we propose a simple mechanism that explains the emergence of these inverse anomalies, using a 1-D column simulation that only reproduces the inversion once a vertical mixing component has been added.

On applications of our work

Advances in eddy detection have a direct application in operational oceanography as well vis-a-vis marine stakeholders:

Reliable eddy detection, proposed here through satellite imagery allows for the real-time correct positioning of structures, which can then be used to extrapolate elements of underwater hydrography and biology, based on actual or past vertical profile measuring as well as the signature of the eddy on infrared and visible images. This can have a direct effect in environmental applications of monitoring pelagic species concentration and fishing (Durán Gómez et al., 2020), the monitoring of the concentration of microplastics (Brach et al., 2018) or the diffusion of oil spill events {walker2011impacts.

Additionally, as described previously, reliable detection of eddies (along with fronts) can act as reference objects, proxies of the dynamical field, used to validate operational oceanographic models. This could further enhance the actual validation means which are currently based on costly in-situ measurements that are very sparse compared with the abundance of reliable eddies that can be detected by satellite.
Finally, applications for the optimal routing of ships to reduce fuel consumption and CO2 emissions can also be proposed. A real-time accurate evaluation of the surface currents through the correct positioning of eddy structures allows for the accurate designation of an optimal ship route using currents in its favour.

Perspectives

Treating Cloud Coverage

Cloud Coverage importantly affects infrared (as well as visible) satellite sensors, and should therefore be treated successfully for an optimal eddy detection method on satellite imagery. We have evoked the question of treatment of cloud coverage as missing data in an image in several of the presented papers. Notably Paper III is dedicated to this question, providing a method of cloud data augmentation in order to artificially generate realistic missing data patterns on a dataset, without corrupting the underlying ground truth. This method is shown to be robust to the classification task with 90 % of accuracy for images with up to 50 % of cloud coverage. This method has also been put to test on the eddy semantic segmentation task, proposed on Paper IV. Preliminary results show that performance stays on the same level when using cloud data augmentation for training, when testing on images with up to 40% cloud coverage. It is one of the immediate perspectives to refine these experiments and perform an ablation study on the robustness to cloud coverage of the semantic segmentation method.
Finally, partial convolutions (Liu et al., 2018) have been employed successfully for image inpainting, by convolving with the omission of missing data. This convolution schema could also be employed to treat in a most effective way the cloud coverage of satellite imagery.

Multi-modal Data Fusion

We choose infrared imagery for eddy detection as the main subject of this work for two main reasons:

- Numerical models directly reproduce SST outputs that can be used to learn similar representations with accurate underlying ground truths. This creates a robust learning schema to then finetune a CNN for application on infrared imagery.

- Compared to visible image products, infrared image products are widely more available in their processed (L3+) versions.

However, the information contained both in visible images as well as in Synthetic Aperture Radar (SAR) observations needs to be harnessed to expand eddy detection capabilities.

To harness visible imagery, we suggest two possible methods :

- Utilizing the Ocean Colour Reflectance (OCR) observations. The main advantage of this method is that OCR is distributed on a linear scale and does not require complex transformations, giving directly the signature of pigment concentration, and thus eddy filament location. The main disadvantage is that there exists no numerical model that reproduces this observed variable, so the collection of data with accurate underlying ground truths (dynamical contours) is a challenge. This could be tackled by retreiving a hand-labeled dataset, or following a semi-supervised method with a teacher-student network. In any case, a network trained to recognize eddy representations on SST, distributed in a linear scale, could be finetuned to be applied to OCR observations.

- Utilizing the Chlorophyll Concentration (CHL) products. These by-products of OCR have as their main disadvantage the fact that they are distributed on a logarithmic scale, and are the product of several calibrations via biological criteria, so important data pre-processing might need to take place. On the contrary, their main advantage is that several numerical models with adapted ocean biology schemas reproduce CHL output which could be used as training data in a transfer learning schema similar to that used for SST.

SAR observations are notably important for their ability to bypass clouds. In operational terms for eddy detection, their main disadvantages are the high revisit time for a certain region as well as the obstruction of eddy signatures by many other effects, particularly wind and waves. Although challenging, the addition of this observation in a detection pipeline could aid the identification of the position of known intense eddies in periods and regions of very strong cloud coverage.

Tracking and Forecasting Methods

Neural Networks such as Long-Short Term Memory Recurrent Networks (Hochreiter et al., 1997), allow for the processing of sequential information, such as speech or video, through feedback connections in their architecture. Taking into account the fact that satellite images provide a sequential information on the dynamics or variables of the ocean through successive maps, these type of networks could be adapted into learning the time component that encompasses the ocean dynamics. Additionally, recurrent-type networks could be used to perform a tracking of eddies in satellite imagery, as is done by standard eddy detection and tracking algorithms on satellite altimetry. Furthermore, these networks can also be employed to forecast the position of these structures in a weekly window, as the movement of mesoscale eddies is generally both slow and follows patterns of direction based on different factors.

Super Resolution

Super Resolution (SR) has been a rapidly advancing field of application of CNNs (Dong et al., 2015), where a Low Resolution (LR) image is upsampled into a High Resolution (HR) version. The LR-HR pairs constitute of training data for the CNNs, which with various architecture and loss function implementation are successfull in augmenting the resolution of images or signals. Recent applications of SR on oceanographic data (Archambault et al., 2022; Buongiorno Nardelli et al., 2022) has shown their potential in upsampling LR fields such as altimetric observation to HR versions by incorporating other HR priors such as SST observations. Additionally, reconstruction methods such as 4D-Var (Fablet et al., 2021) utilizing variational formulations for the space-time reconstruction of ocean dynamics through Deep Neural Networks with convolutional operators and LSTM blocks, consist of a state-of-the-art for the incorporation of both the spatial as well the time aspects of satellite observations formulating the reconstruction of the HR fields as an inverse problem. By using the Numerical Model transfer learning schema, as well as the OSSE principle, to synthetically simulate altimetric observations, as was done for this study, SR can be successfully applied to improve altimetric observations maps, using the information of satellite imagery, therefore also improving the capabilities of standard eddy detection.